# Fiber Based Infrared Lasers and Their Applications in Medicine, Spectroscopy and Metrology

by

Vinay Varkey Alexander

A dissertation submitted in partial fulfillment
of the requirements for the degree of
Doctor of Philosophy
(Electrical Engineering)
in the University of Michigan
2013

Doctoral Committee:

Professor Mohammed N. Islam, Chair
Associate Professor Hitinder S. Gurm
Professor Fred L. Terry Jr.
Professor Michael J. Welsh

To my Appa and Amma – Thank you$^{\infty}$

## ACKNOWLEDGEMENTS

First and foremost, I would like to sincerely thank my advisor, Professor Mohammed N. Islam for giving me the opportunity to pursue my doctoral study under his mentorship. Thank you for teaching me the importance of thinking outside the box and for so much more, than just doing good science. I truly believe that the skills I learned in this group under Prof. Islam's guidance will help me throughout my life, and for that I will always be grateful.

I would also like to thank my committee members, Prof. Fred Terry, Prof. Michael Welsh and Prof. Hitinder Gurm for their valuable help and support on various topics in this thesis. Despite their busy schedules, they always made time to guide and discuss various aspects of my doctoral work.

A large part of my graduate life was spent in lab with some of the most amazing colleagues and now good friends: Malay Kumar, Ojas Kulkarni, Chenan Xia, Ramon Martinez and Zhennan Shi. It was a privilege to have worked with all of you and I will always cherish our time together in this lab.

Special mention is needed for the Omni Sciences team, particularly Dr. Michael Freeman for immensely fruitful discussions on various topics covered in this thesis. His expertise on the optics and electronics design was invaluable in successfully carrying out various experiments in my doctoral work. I would also like to thank Dr. Kevin Ke at Omni Sciences for his help on several projects.

Most of the works presented in this thesis required the help of people with expertise in various fields. I could not have done good work without their help and support and I would like to express my sincere gratitude to the following people. David Carter, Jim Tice and Michael Folts at the Physics Instrument shop, Judy Poore and Jeff Harrison at the Microscopy and Image Analysis Laboratory, Gail Rising, Amber Yanovich, Kim Walacavage and Dr. Ingrid Bergin at the Unit for Laboratory Animal Medicine, and Roy Wentz at the Chemistry Glass shop.

Over the years, during my stay in Ann Arbor, I have also made some good friends who provided great company over the years: Xu Zhao, Nidhi Talwar, James Easter, Priyank Kumar, Nick Lalic, Nupur Srivastava and Scott Rudolph. I would like to take this opportunity to wish them all the very best for their future endeavors.

I would also like to thank the funding agencies, NGA, AFRL, SAIC, OmniSciences, Inc, Coherix Inc, UM Cardiovascular Center and the University of Michigan, for financially supporting me and my work during the course of my doctoral studies.

Finally, I would like to thank my parents, Dr. Varkey Alexander and Annie Alexander and my Brother, Vijay Alexander for their unwavering support and confidence in my abilities. They have whole heartedly supported me in all of my pursuits, both academic and personal. I am forever indebted to their kindness and generosity. Thank you for teaching me the value of hard work and the importance of being a good and humble human being. I would not be where I am today without their unconditional love and support.

## TABLE OF CONTENTS

DEDICATION....ii

ACKNOWLEDGEMENTS....iii

LIST OF FIGURES....vii

LIST OF TABLES....xiii

ABSTRACT....xiv

**Chapter**

I .Introduction ....1

1 Fiber Based Infrared Lasers for Acne Treatment .... 4
2. Fiber Based Infrared Lasers for Renal Denervation.... 5
3. All-Fiber SWIR SC Lasers for Long Distance Spectroscopy .... 9
4. All- Fiber SC laser for Surface Roughness Measurement .... 12

II. Photothermolysis of Sebaceous Glands in Human Skin Ex Vivo with a 1708 nm Raman Fiber Laser and Contact Cooling: A potential Treatment for Acne ....17

1. Introduction .... 17
2. Materials and Methods .... 19
3. Experimental Results.... 28
4. Discussion and Conclusions.... 36

III.Renal Denervation Using Focused Infrared Fiber Lasers: A potential Treatment for Hypertension....42

1. Introduction .... 42
2. Materials and Methods .... 46
3. Experimental Results.... 59
4. Discussion .... 73
5. Summary .... 77

IV.Active Remote Sensing Using A Near Diffraction Limited High Power Short Wave Infrared Supercontinuum Laser ....83

1. Introduction .... 83
2. Field Trial Setup.... 86
3. SWIR SC Laser .... 90
4. Experimental Results.... 92
5. Discussion .... 100
6. Summary .... 103

V. Power Scalable > 25 W Supercontinuum Laser from 2 -2.5 μm with Near Diffraction Limited Beam and Low Output Variability ..... 106
1. Introduction ..... 106
2. Experimental Setup ..... 107
3. Experimental Results ..... 110
4. Discussion ..... 115
5. Summary ..... 118
VI. Surface Roughness Measurement of Flat and Curved Machined Metal Parts Using a Near Infrared Super-Continuum Laser ..... 121
1. Introduction ..... 121
2. Experimental Setup and Method ..... 125
3. Theory and Data Analysis ..... 127
4. Results ..... 129
5. Discussion ..... 139
6. Summary ..... 142
VII. Summary and Future Work ..... 146
1 Laser Treatments for Acne ..... 146
2 Laser Treatments for Hypertension ..... 148
3 Supercontinuum Laser for Remote Sensing ..... 152
4 Supercontinuum Laser for Metrology ..... 155

## LIST OF FIGURES

**Figure**

Fig 1.1. (a) Absorption spectra of water, haemoglobin, melanin and proteins together with scattering in tissue [4]. Absorption spectrum for water[5], adipose[6], and collagen[7]. .. 2

Fig. 1.2. Illustration of the relation between renal sympathetic nerves and hypertension. RF renal denervation is shown on the right[26]..... 7

Fig. 1.3. Architecture for MI initiated SC generation process: amplified pump pulses followed by pulse breakup in single-mode fiber followed y spectral broadening in SC fiber[13]. ..... 10

Fig. 1.4. Atmospheric transmission window from the visible to the mid-IR wavelength range (Source: Santa Barbara Research Center)..... 11

Fig. 2.1. Infrared spectra showing the coefficients for water ($\mu_a$) and human fat absorption, effective scattering in the dermis ($\mu_s'$)and combination of water absorption with the effective scattering in the dermis ($\mu_t'$); also noted are common wavelengths of IR lasers used in acne treatments. ..... 20

Fig. 2.2. 1708 nm Raman fiber laser setup showing the two main stages; amplified 1542 nm source (left) and the cascaded Raman oscillator (right). ..... 22

Fig. 2.3. Scanning laser treatment setup without surface cooling. The sample is placed on a holder and scanned across the laser beam using a computer controlled stepper motor stage. ..... 24

Fig. 2.4. Ex vivo skin laser treatment setup with surface cooling to protect the epidermis. Block B2 is always kept at ~37°C and block B1 is initially kept at ~37°C and then cooled to ~2°C starting 5 seconds prior to laser exposure. ..... 25

Fig. 2.5. Histology of ex vivo porcine heart tissue cross section treated with the 1708 nm laser (2mm spot, 2mm/s scanning exposure) at 750 mW showing damage to pericardial fat with very little damage to the myocardium. Both the pericardial fat and myocardium were exposed to the same laser parameters. ..... 29

Fig. 2.6. Histology of ex vivo porcine intestinal visceral fat cross section treated with the 1708 nm laser (2mm spot, 2mm/s scanning exposure) at 600mW showing damage to the fat with no damage to the embedded blood vessels. The fat and the blood vessels were all exposed to the same laser parameters. ..... 30

Fig. 2.7. Histology of ex vivo porcine skin tissue cross section treated with the 1708 nm laser (2mm spot, 2mm/s scanning exposure) at 800mW showing damage to the subcutaneous fat with no damage to the epidermis or the dermis. The epidermis, dermis and the subcutaneous fat were all exposed to the same laser parameters. ..... 31

Fig. 2.8. Histology of ex vivo human skin treated with 1708 nm laser (2mm diameter spot and 5 mm/min scanning exposure) at (a) 375mW and (b) 275mW showing thermal damage to the epidermis and dermis, extending to ~ 1mm into the dermis from the skin surface; insets show damaged and undamaged sebaceous glands. ..... 33

Fig. 2.9. MTT histochemistry of ex vivo human skin treated with 1708 nm laser and cold window (5 seconds pre-cool; 2mm diameter spot exposure for 3 seconds) at 725 mW (A, B) corresponding to ~70 J/cm$^2$ average fluence and 830 mW (C, D) corresponding to ~80 J/cm$^2$ average fluence. ..... 34

Fig. 2.10. Maximum depth of thermally induced damage in the dermis as measured from MTT histochemistry results at different 1708 nm average fluences..... 35

Fig. 3.1. Infrared spectra showing the coefficients for water ($\mu_a$) and human fat absorption, effective scattering in the dermis ($\mu_s'$)..... 48

Fig. 3.2. The laser sources used in the renal denervation study, 980 nm laser diode, 1210 nm laser diode, 1700 nm laser diode and our developed fiber laser source. ..... 51

Fig. 3.3. Experimental setups used for the in vitro experimental studies. (a) Collimated laser beam setup and (b) Focused laser beam setup. ..... 51

Fig. 3.4. Extraction of the renal artery and sample preparation for the in vitro experiments. The renal artery is first identified and extracted. The artery is then sectioned (along dashed lines) and prepared for laser treatments..... 52

Fig. 3.5. Distal end design for the catheter used to deliver the in vivo treatments. ..... 53

Fig. 3.6. ZEMAX Simulation results of the distal end performance in tissue (a) Outer tube – focus vs. the air gap length. (b) Estimate of the beam diameters at the distal end output and at the focus. ..... 54

Fig. 3.7. Tygon tube model used to test that the final catheter is able to make the bend and get to the renal artery. The aorta and renal artery diameters are assumed to be 1 cm and 0.5 mm respectively. ..... 55

Fig. 3.8. In vitro wavelength comparison study at (a) 980 nm( 23W) (b) 1210 nm (10 W) and (c) 1700 nm(6 W). The samples are all scanned across a 3mm diameter beam at 1 mm/s. Extreme tissue damage was observed in (c) using the 1700 nm laser. ..... 60

Fig. 3.9. Measured depth of damage in chicken breast tissue treated with 980 nm, 1210 nm and 1700nm .The depths are measured from the histochemistry results ..... 60

Fig. 3.10. In vitro laser renal denervation in bovine renal artery (a) Untreated control section (b) Artery cross section treated with collimated 1700 nm laser (1.5W, 2mm beam,0.4mm/s scan) showing damaged nerves and artery tissue. ..... 62

Fig. 3.11. In vitro porcine renal denervation results using the focused laser setup at 980 nm(a,b,c), 1210 nm(d,e,f) and 1700nm (g,h,i), scanned at 0.4mm/s. Three cases are shown for each wavelength The first column shows inadequate damage. The middle column shows the optimum treatment condition achieved for each wavelength with thermal damage to the nerves and little to no damage to the endothelium. The third column shows treatment power levels high enough to cause transmural damage extending across the entire section. ..... 66

Fig. 3.13. In vitro renal denervation in sheep using the 980nm laser scanned at 0.4mm/s (a) Histochemistry of treatment with 2 W showing damaged nerve with no apparent injury to the endothelium (b) Histochemistry of treatment with 3 W showing transmural damage to the nerve and arterial tissue across the entire depth. ..... 67

Fig. 3.14. Fluoroscope image of laser catheters in sheep in vivo (a) Left kidney (b) Right kidney. ..... 68

Fig. 3.15. MTT histochemistry of sections from in vivo trials showing complete renal denervation with 980 nm laser at the treatment site using catheters FL1 (a and b) and FL2 ( c and d). ..... 69

Fig. 3.16. Histochemistry sequence of sections surrounding the sections from Fig. 3.15, which show renal nerve damage after treated with . (a) catheter FL1 and (b) catheter FL2. ..... 70

Fig. 3.17. Catheter FL1 and FL2 intensity difference factor between the endothelium and the focus for various focus positions within the tissue. Both absorption and the focusing effect are taken into account. ..... 72

Fig. 3.18. MTT histochemistry examples showing damage to the media/adventitia with little to no injury to the endothelium and artery wall. (A) catheter FL1 3.5-4W,5 seconds (B) catheter FL1, 2-2.5W, 5 seconds. ..... 73

Fig. 3.19. Catheter distal end design with a focal length of ~ 2mm. The intensity difference factor is calculated to be > 5x for focus positions at depths > 1 mm and suggests that it should be possible to damage nerves without injuring the endothelium as long as the distal end is within ~ 1mm from the artery wall. ..... 75

Fig.4.1.Atmospheric transmission window from the visible to the mid-IR wavelength range (Source: Santa Barbara Research Center). ..... 84

Fig. 4.2. (a) Map view of 1.6 km tower to ground path at Wright Patterson Air force base (b) Diagram of tower-target test layout ..... 86

Fig. 4.3. (a) SC laser optical layout in the tower at the WPAFB. (b) ) SC laser in the tower at WPAFB. ..... 87

Fig. 4.4. (a) Overhead view of the SWIR camera setup used for the beam quality measurements and (b) an image of the SWIR camera ..... 88

Fig. 4.5 (a)Overhead view of the spectroscopy setup showing locations from target to SR1. (b) Image of SR1 used for the diffuse reflectance measurements. ..... 88

Fig. 4.6 (a)Overhead view of the spectral stability measurement setup showing locations from target to SR2. (b) Image of SR2 used for the apectral stability measurements. ..... 89

Fig.4. 7. (a)Optical layout of the all-fiber integrated 5W SWIR SC laser. (b) Packaged 5W SC laser prototype. (c) Collimation setup for the SC final output. ..... 90

Fig.. 4.8. (a) SC output spectrum spanning from ~1.55 to 2.35 μm with an average power of ~5W across the continuum. (b) SC output power scaling with 940 nm pump power.. 91

Fig.4. 9. Preliminary beam divergence measurements (a) Map view of airfield ~720 m used for measurements. (b) Infrared thermal viewer image of the beam at ~720 m

corresponding to a full angle divergence of ~0.6 mrad, well within our specification of < 1 mrad. ..... 92

Fig. 4.10. SC laser(EYFA system) beam profile measurements at ~1.6 km; 1000 frame average (a) Camera image of the beam (b) 3 D image of the beam (c) Gaussian fit and beam width measurement. ..... 94

Fig. 4.11. Spectral reflectance measurements at ~1.6 km using the SC laser(solid lines) and their comparison to in-lab measurements performed using a quartz-halogen lamp (dashed lines) . (a) Retrieved reflectance of white cloth, tyvek, and wallboard (b) Retrieved reflectance of plywood, gray painted plywood and blue tarp (c) Retrieved reflectance of gray and black silt cloth. ..... 96

Fig 4.12. Reflectance spectra for blue tarp, plywood and gray silt cloth corrected with constant offset factors in each of the SWIR wavelength bands. The SC measurements overlap fairly well with the reference measurements after the applications of a the constant offset factors in each on the SWIR wavelength bands. ..... 97

Fig. 4.13. (a) Sample measurement sequence of radiance spectra at 1.6km range. (b) Relative scan-to-scan variability for 8 field measurements ..... 99

Fig. 4.14. (a) Single frame image of the SC laser beam at ~1.6 km. showing effects of atmospheric turbulence. (b) 1000 frame average of the same beam with background subtraction showing a much smoother beam profile. ..... 101

Fig. 4.15. Long term power stability measurements of the 5 W SC prototype (Left) Zoomed in view (Right) ..... 102

Fig.5. 1.Block diagram and table top layout of the 25.7W SC laser system ..... 108

Fig. 5.2. Measured output power from ~1.5m of combiner fiber versus 793nm pump power for various lengths of the 25/250 μm TDFA. ..... 109

Fig. 5.3. (a) 25.7W SC output spectrum (b) SC output power scaling with 793 nm pump power..... 110

Fig. 5.4. (a) Linear scaling of the SC average power with repetition rate. (b) Nearly constant SC output Spectra with average power scaling from ~5 -25.7 W. ..... 111

Fig. 5.5. SWIR camera image of the beam at 25.7 W SC (Left). Corresponding Gaussian fit of the beam cross section at 25.7W (Right). ..... 112

Fig.5. 6. SC beam quality measurements using a SWIR camrera. (a) Measured FWHM beam width with power scaling . (b) Calculated $M^2$ measurements with power scaling. ..... 113

Fig. 5.7. SC Output stability measurements. (a) Sixty scan sequence of the 25.7W SC spectra. (b) SC output relative variability with power scaling..... 114

Fig.5 8. Diffuse spectral reflectance measurements of various samples using the SC laser (solid) and reference measurements performed using a lamp. ..... 115

Fig. 5.9. Fiber thermal damage (a) Fiber jacket/recoat is clearly burnt due to lack of good thermal management. (b) Thermal study of the fiber used in our system show a slight browning at ~150 deg C and clear damage at ~200 deg C. ..... 116

Fig.5.10. Spectral data showing that the spectral flatness can be improved by increasing the output peak power. ..... 117

Fig. 6.1. Optical layout of the surface roughness measurement setup for crankshaft journal measurements. ..... 126

Fig. 6.2. Comparison of normalized reflectance curves using smooth steel and gold references for both Flat A and B. Extracted roughness values for Flat A are 0.152±0.010 µm (w/gold reference) and 0.151±0.010 µm (w/steel reference). Extracted roughness values for Flat B are 0.313±0.005 µm (w/gold reference) and 0.312±0.009 µm (w/steel reference). Larger slope values correspond to higher surface roughness values. ..... 131

Fig. 6.3. Normalized reflectance spectrum of Flat B at 45° where $2 \le g \le 5.6$. The slope of the normalized reflectance is not a straight line and begins to curve at lower wavelengths where the diffuse scattering component begins to dominate in the specular direction. This will result in an erroneous roughness value..... 133

Fig. 6.4. Normalized reflectance spectrum of Flat B at 73° where $0.35 \le g \le 0.96$. The reflectance curve is once again a straight line as expected from the BK model and the correct roughness value can be extracted from the slope of this line. The extracted roughness value is seen to be in good agreement with the value measured using a stylus profilometer..... 133

Fig. 6.5. Example of a crankshaft journal ..... 135

Fig. 6.6. Measured signal for the reference (gold mirror) and sample (crank B) as measured by the two detectors DET 1and DET 2 respectively ..... 136

Fig. 6.7. Normalized reflectance spectrum and the extracted roughness values for cylindrical crank journals Crank B and Crank C respectively. Dotted lines represent the 95% confidence interval for the fitted y-axis values. ..... 136

Fig.6.8. Super-continuum vs. stylus measured roughness values. The SC roughness values are seen to be in good agreement with the values measured using a stylus profilometer..... 138

Fig. 6.9. RMS roughness distributions for Crank A and Crank B. Crank A has a higher roughness distribution towards lower roughness values while Crank B has a higher distribution towards larger surface roughness values. Crank A is specified as a journal with acceptable roughness by the vendor. This data indicates that Crank B has a higher surface roughness value than Crank A and is therefore not polished to specification. .. 139

Fig 7.1. Catheters used in current renal denervation procedures. (a) SYMPLICITY catheter design used for RF renal denervation (http://www.medtronicrdn.com/intl/news-events/media-resources/index.htm )(b) PARADISE catheter design used for ultrasound renal denervation[5]. ..... 150

Fig. 7.2 ZEMAX simulations for GRIN lens (a) Outer-tube to focus distance versus air gap distance. (b) Beam diameter at outer tube and focal spot and the corresponding NA calculations ..... 151

Fig. 7.3 ASTM standard terrestrial solar spectrum for AM1.5, Direct spectrum from standard ASTM E891 and global spectrum from ASTM E892..... 154

Fig. 7.4. A potential design for in-line surface roughness measurement using the SC laser ..... 157

## LIST OF TABLES

**Table**

Table 3.1. Penetration depth calculations in tissue for 980 nm, 1210 nm and 1700 nm. ..49

Table 3 2. Penetration depth calculations in blood (5% hematocrit concentration) for 980 nm, 1210 nm and 1700 nm .....49

Table 3.3. Laser Sources used for the in vitro renal denervation study.....50

Table 3.4. Comparison of trends between the penetration depth calculations and the measured depth of damage from the histochemistry results.....61

Table 4.1. 5 W SWIR amplitude fluctuations at different wavelengths measured in lab*99

Table 6.1. Comparison of flat sample RMS roughness values.....134

Table 6 2. Comparison of crank journal RMS roughness values .....137

Table 7.1. Approximate values for the SC power required to match the solar irradiance at ~1.6 km and ~3 km. .....154

## ABSTRACT

In my thesis, I have demonstrated the development of fiber based infrared lasers and devices for applications in medicine, spectroscopy and metrology. One of the key accomplishments presented in this thesis for medical applications is the demonstration of a focused infrared laser to perform renal denervation both *in vivo* and *in vitro*. Hypertension is a significant health hazard in the US and throughout the world, and the laser based renal denervation procedure may be a potential treatment for resistant hypertension. Compared to current treatment modalities, lasers may be able to perform treatments with lesser collateral tissue damage and quicker treatment times helping to reduce patient discomfort and pain. An additional medical application demonstrated in this thesis is the use of infrared fiber lasers to damage sebaceous glands in human skin as a potential treatment for acne.

Another significant work presented in this thesis is a field trial performed at the Wright Patterson Air Force Base using a Short Wave Infrared (SWIR) Supercontinuum (SC) laser as an active illumination source for long distance reflectance measurements. In this case, an SC laser developed as part of this thesis is kept on a 12 story tower and propagated through the atmosphere to a target kept 1.6 km away and used to perform spectroscopy measurements. In the future this technology may permit 24/7 surveillance based on looking for the spectral signatures of materials. Beyond applications in defense, this technology may have far reaching commercial applications as well, including areas such as oil and natural resources exploration. Beyond these major contributions to the state-of-the-art, this thesis also describes other significant studies such as power scalability of SWIR SC sources and non-invasive measurement of surface roughness.

# Chapter I

# Introduction

Fiber lasers were invented by Elias Snitzer in 1963[1, 2] and the first rare earth doped fibers produced powers of only a few milliwatts[3]. About two decades of development later, the first commercial devices appeared in the market in the late 1980s , used single mode diode pumping and emitted a few tens of milliwatts. Nevertheless, it attracted many users because of their large gains and the feasibility of single mode continuous wave lasing for transitions of rear-earth ions not achievable in the common crystal laser versions [2] . Even to this day, the most well known application of fiber laser technology is its use in fiber amplifiers, most of which happen to have emission bands in the infrared (IR) wavelengths, such as Ytterbium Doped Fiber Amplifiers (YDFA) used for amplification at ~1060nm, Erbium Doped Fiber Amplifiers (EDFA) and Erbium, Ytterbium doped Fiber Amplifiers (EYFA) for ~1550 nm and more recently the Thulium Doped Fiber Amplifiers (TDFA) for ~2000 nm. These fiber amplifiers then laid the groundwork for true high power fiber lasers. Fiber lasers have a number of advantages compared to competing laser sources, such as high efficiencies of (> 30 % pump to signal), high brightness, excellent beam quality, high output powers and easy coupling into other fibers or systems[4]. Although fairly new and still developing, high power fiber lasers have many potential applications in various fields such as micromachining, medicine, remote sensing and metrology.

Most of these fiber amplifiers also have absorption bands in other IR wavelengths. For example, EDFA and EYFA fiber amplifiers have an absorption band at ~980 nm, which can then serve as a pump for the fiber amplifiers. Similarly, TDFA amplifiers are often pumped using ~790 nm pumps diodes. In a lot of ways, the growth of infrared fiber lasers and their power requirements have fueled the development of high power fiber coupled diode lasers as pumps for these systems, and vice versa. Fiber

coupled 980 nm laser diode systems are now available with average powers of > 100 W. Commercial fiber coupled diode lasers at other infrared wavelengths, such as the 1210 nm and 1700 nm laser are also being developed as their use in medical applications are being demonstrated. Thus, the infrared wavelengths are an attractive spectral region to work in due to the abundance of high power fiber based laser sources. In most cases, it is convenient and sometimes required to have an optical fiber output, in order to deliver the light to where it is needed. This is an obvious requirement for certain applications like catheter based medical treatments, where the fiber itself is an integral part of the energy delivery to the treatment site.

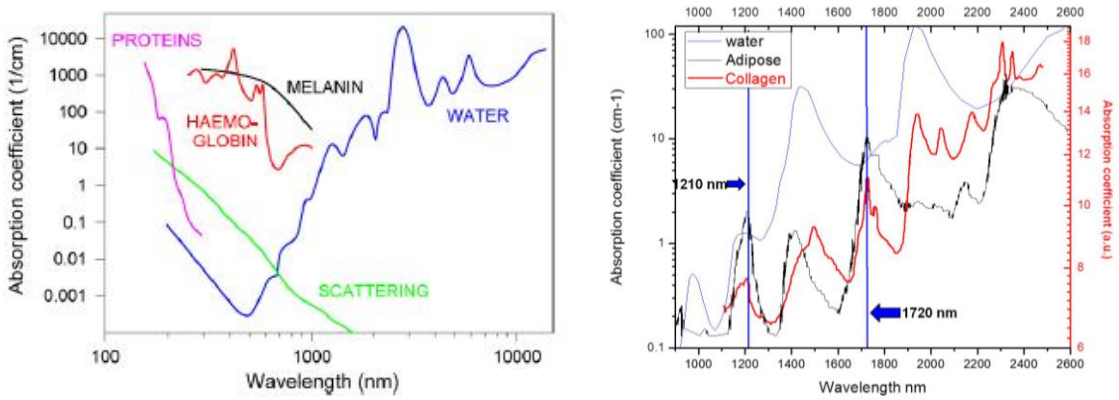


(a) (b)

*Fig 1.1. (a) Absorption spectra of water, haemoglobin, melanin and proteins together with scattering in tissue [5]. Absorption spectrum for water[6], adipose[7], and collagen[8].*

In addition to the availability of convenient high power fiber based lasers, infrared wavelengths have other advantages as well. For example, in medical applications, published reports have demonstrated that the wavelengths ~800-1100 nm offer relatively deep penetration depths in water and efficient volumetric heating, which permit the delivery of necrotic temperatures deep into the tissues [9]. As Fig. 1.1a shows, this is enabled by the low absorption coefficient for blood and water at these wavelengths. There are also several tissue components like adipose and collagen, that have absorption peaks in this wavelength region (Fig. 1.1b), which allows for selective targeting of these components. For example, reports have been published demonstrating the ability of a ~1720nm laser to selectively target lipid rich sebaceous glands in human skin tissue [10]. The availability of fiber based laser devices and the variety of achievable penetration depths in the infrared wavelengths has led to the development of various *in*

*vivo* catheter based procedures as well. Clinical trials involving fiber based catheter procedures have been reported in treatments for atrial fibrillation[11], endovenous laser ablation [12] and interstitial laser therapy[9].

Unlike medical applications that usually rely on single wavelengths to achieve a therapeutic effect like ablation depth or selective targeting, there are a number of applications such as spectroscopy, remote sensing, hyperspectral imaging, etc, that require broadband illumination sources in the infrared wavelengths. Broadband sources in the infrared wavelength s are attractive for such long distance applications due to the presence of so-called atmospheric transmission windows, where losses due to propagation are minimal [13]. Previous works have demonstrated the use of a fiber as an ideal choice for broadband light generation known as supercontinuum [14]. Supercontinuum generation describes the process by which narrow band optical pulses undergo substantial spectral broadening through the interplay of a number of non-linear optical interactions in the medium, to yield a broadband spectrally continuous output. Broadband SC generation in optical fibers has been of particular interest due to the unique advantages offered by their long optical interaction lengths and high non linearity. In addition fiber based SC lasers are potentially compact, reliable and robust, which make them attractive candidates over conventional bulk lasers sources for practical applications. With the development of mature fiber amplifiers like EYFA and TDFA, high power fiber coupled pump diodes, optical fibers of various materials, geometries and dispersion profiles; it is now possible to construct a broadband SC fiber laser platform for almost any wavelength of interest from the UV to the mid-IR [14].

In my thesis, I demonstrate the development of fiber based infrared lasers and devices for applications in medicine, spectroscopy and metrology. One of the key accomplishments presented in this thesis for medical applications is the demonstration of a focused infrared laser to perform renal denervation both *in vivo* and *in vitro*. Hypertension is a significant health hazard in the US and throughout the world, and the laser based renal denervation procedure may be a potential treatment for resistant hypertension. An additional medical application demonstrated in this thesis is the use of infrared fiber lasers to damage sebaceous glands in human skin as a potential treatment for acne. Another significant accomplishment is this thesis is a field trial performed at the

Wright Patterson Air Force Base using a Short Wave Infrared (SWIR) Supercontinuum laser as an active illumination source for long distance reflectance measurements. In the future this technology may permit 24/7 surveillance based on looking for the spectral signatures of materials. Beyond applications in defense, this technology may have far reaching commercial applications as well, including areas such as oil and natural resources exploration. Beyond these major contributions to the state-of-the-art, this thesis also describes other significant studies such as power scalability of SWIR SC sources and non-invasive measurement of surface roughness.

# 1 Fiber Based Infrared Lasers for Acne Treatment

Lasers were introduced in the specialty of dermatology in the mid -1960s. Since the skin is easily accessible to examination and study by lasers, dermatologists usually play an important role in defining the early clinical usefulness and limitations of laser systems. They have also contributed much to the knowledge base of laser-tissue interactions that helped to further improve the usefulness of lasers in various medical applications. There are a large number of lasers in the visible to the infrared wavelengths used for various types of dermatological indications. The major effect of lasers on skin is photothermolysis[5] .

Acne vulgaris is one of the most common diseases of the skin and, in cases of extreme disfigurement , can severely impair the personality development and carries the significant potential for psychosocial morbidity[15, 16] . Several studies using visible lasers, infrared lasers, broadband light sources and photodynamic therapy have all been reported in literature. While some of these works reported some potential efficacy , other work demonstrated no clear benefits and as such, lasers were not considered the main therapeutic choice for acne [17]. It is well known that excess sebum production is one of the main factors responsible for acne [17], which typically affects the areas of the skin with the densest population of sebaceous follicles, such as the face, upper part of the chest and back. Clinical drugs like Accutane (isotretinoin) have had much success in controlling acne. However, given the risk associated with the use of isotretinoin, there is great interest in developing an alternate treatment. Skin samples obtianed from patients treated with isotretinoin showed sebaceous gland atrophy and destruction[18, 19]. Thus,

treatments that specifically target sebaceous glands are considered an attactive strategy for acne treatments.

A number of infrared lasers at 1450 nm, 1540 nm and 1320 nm have been reported in literature for acne treatments[20-22]. However, these wavelengths target the tissue water content to cause injury to the sebaceous glands and results using these lasers were seen to be quite transient[21, 23]. Perhaps, a wavelength that targets lipids directly instead of the water content could prove to be more effective in destroying sebaceous glands and improving conditions like acne. The absorption spectrum for fat in Fig. 1.1b show a clear lipid absorption peak at ~1720 nm, which appeared to be the ideal wavelength to use for this treatment. However, at the time of our experiments, there were no commercially available laser sources at ~1720 nm.

In chapter 2, I present the development of a fiber infrared laser at 1708 nm, close to the absorption peak at ~1720 nm. I demonstrate with histological evidence that the 1708 nm laser is capable of selectively targeting the fat in several tissue samples. I also show examples of human skin samples, both with and without any surface cooling, treated with the 1708 nm. Experiments without cooling showed entire tissue damage including the epidermis, dermis and the sebaceous glands. Treatments with surface cooling showed damage to the sebaceous glands at depths of ~ 1.6mm, but the epidermis and a portion of the dermis were seen to be saved. While further research and clinical studies are required to determine the optimum treatment parameters, the selective damage of sebaceous glands using ~1720 nm laser has since been reported in literature by other groups.

## 2. Fiber Based Infrared Lasers for Renal Denervation

Hypertension is a significant health hazard and the search for a cure goes back several centuries. The first anatomically correct depiction of the sympathetic nerves was described in 1664[24] , followed by the discovery of vasoconstriction by electric nerve stimulation in 1840[25], which eventually lead to the understanding of renal nerve role in the maintenance of hypertension [26]. More than half a century ago, a surgical procedure, thoracolumbular sympathectomy, which involved the removal of nerve trunks and splanchnic nerves was sometimes performed to control blood pressure in patients with

malignant hypertension. While this was effective , it also had debilitating side effects such as postural hypotension, erectile dysfunction, and syncope [27]. The morbidity from these procedures remained high and the search for a better cure continued on [26, 27].

It is fairly well established that renal sympathetic nerves play a pivotal role in hypertension [27, 28]. The kidneys are supplied with postganglionic sympathetic nerve fibers that end in efferent and afferent renal arterioles and studies in humans and animals have shown that an increase in the efferent signals (i.e. from the brain to the kidney) leads to renal vasoconstriction and decreased renal blood flow, increased renin release and sodium retention. Afferent signals ( from the kidney to the central nervous system) are increased in states of renal ischemia, renal parenchymal injury and hypoxia and disinhibit the vasomotor center in the central nervous system, leading to increased efferent signals to the kidneys, heart and peripheral blood vessels. This process is illustrated in Fig.1.2 [27].

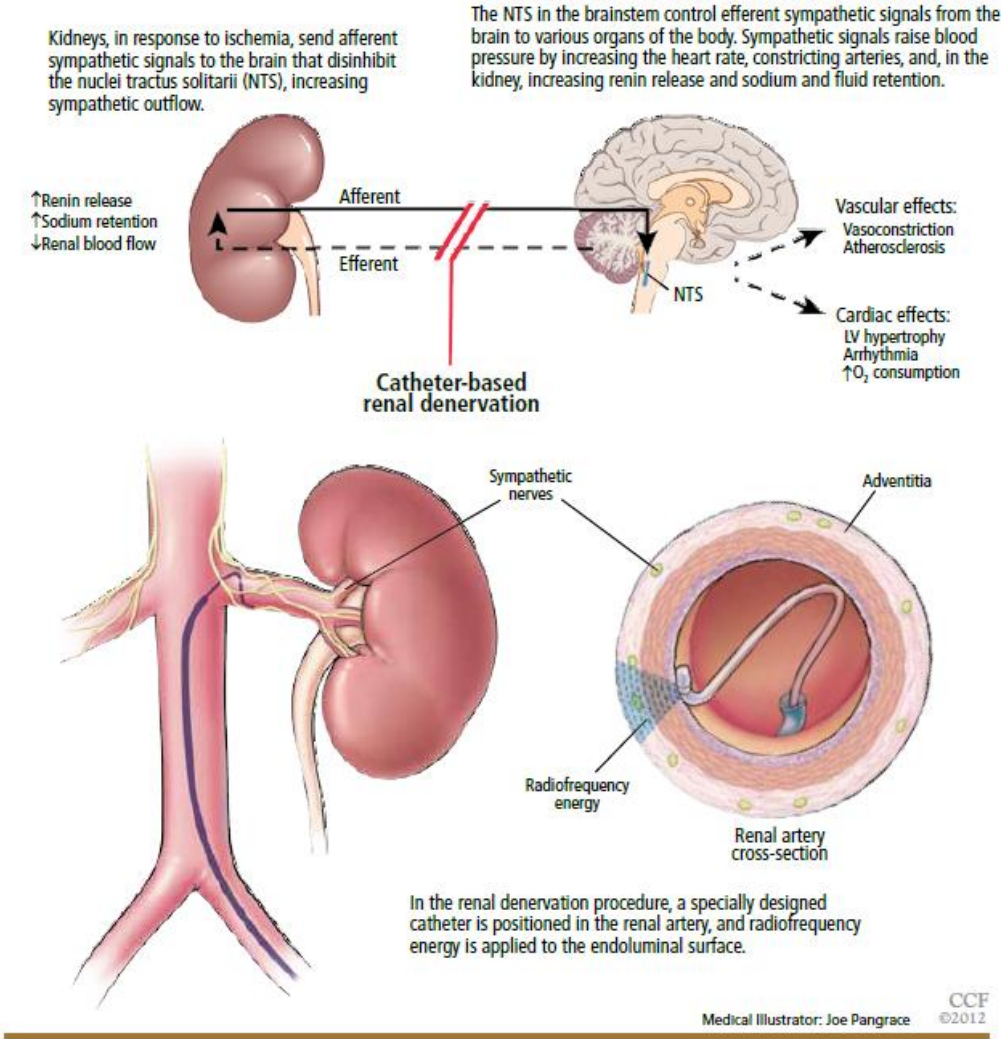


*Fig. 1.2. Illustration of the relation between renal sympathetic nerves and hypertension. RF renal denervation is shown on the right[27].*

Recently, a number of percutaneous catheter based approaches have been developed to target the renal sympathetic nerves in an effort to treat hypertension. A Few clinical studies have also been performed with promising results. The existing techniques for renal denervation use either radiofrequency (RF) [29] or ultrasound therapy [30] to achieve renal denervation. RF is currently the most widely used treatment modality for catheter based renal denervation. The ablation catheter is inserted into the renal artery with the electrode tip in contact with the vessel wall prior to delivering RF energy into the artery ablating the surrounding sympathetic nerves and interrupting autonomic nerve traffic to and from the kidneys [28, 31]. Since, the electrode tip is in contact with the vessel wall, a large amount to energy is delivered to the wall. Morphological assessment

of porcine renal arteries after RF denervation, show acute transmural tissue coagulation and loss of endothelium resulting in local thrombus formation [32]. Another concern for RF denervation is the large penetration depth and lack of directionality. Ablation extent is largely determined by the catheter characteristics, such as electrode size and energy parameters [33]. All these variables must be optimized so that the renal ablation lesions are deep and wide enough to affect the nerves but not so much as to risk perforation, stenosis and thrombosis of the artery [28]. In addition, it is not possible to easily collimate/focus RF energy, which could result in the damage of non-target arterial tissue during denervation. Other procedural limitations include the catheter instability, triggering frequent treatment interruptions and the overall duration of the procedure, which consists of a minimum of eight two minute ablations, the time required to reposition the device continuously and the associated patient discomfort or pain [30]. Therefore, a treatment modality that minimizes the treatment duration, acute endothelial damage and/or damage to the non-target arterial tissue would be attractive for renal denervation.

In chapter 3, I present the use of fiber based focused infrared lasers as an alternative energy source for catheter based renal denervation and address some of the advantages of focused laser denervation over the RF technique . Infrared (900 nm -2000 nm) fiber lasers have various features that make them attractive for renal denervation. First the wavelengths of light can be chosen to achieve the required tissue penetration depths. Unlike RF, the penetration depth in tissue can be easily adjusted by using the right wavelength. For eg: at 980 nm, the maximum tissue depth of damage that we observed in tissue is ~ 5 mm compared to only ~ 3mm at 1700 nm. Limiting the depth of damage can help in avoiding issues like vessel perforations. Second, lasers have high directionality, i.e. they can be easily collimated or focused. Focusing the laser creates an intensity difference, which translates to a temperature difference in tissue along the focus. In chapter 3, I show that is possible to achieve *in vitro* renal denervation without damaging the endothelium by focusing the laser near the nerves and without any external cooling. Third, laser energy is absorbed by the tissue faster than RF ( lower penetration depth usually indicates higher absorption. This would then suggest that laser denervation treatments should be much shorter than RF treatments. In chapter 3, I will also show,

using a designed catheter prototype, that it is possible to achieve renal denervation *in vivo* with depths of damage extending > 1.5 mm, and a laser treatment duration of only 5 seconds. With an estimated 4-6 spots/artery, the total energy delivery time is expected to be less than two minutes. While further research and clinical studies using laser renal denervation are warranted to determine the optimal treatment parameters and to evaluate the efficacy of lasers denervation as a potential treatment for hypertension, the *in vitro* and *in vivo* results presented in chapter 3 show histological evidence that it is possible to achieve renal denervation using lasers.

## 3. All-Fiber SWIR SC Lasers for Long Distance Spectroscopy

A part of the research performed in our group is focused on supercontinuum generation in optical fibers. SC generation is the result of propagation of high intensity pulses in a suitable dispersive medium, resulting from the interplay of numerous nonlinear processes such as self-phase modulation, modulation instability, stimulated Raman scattering, etc that gives rise to a broadband continuum at the wavelength output [14]. Typically, SC lasers use mode-locked laser sources to obtain the high peak power ultra short pulses coupled into a fiber suited for the non linear processes required for SC generation. However, our group uses an alternate technique called modulation instability (MI) that uses the physics of the fiber itself, to initiate high peak power pulses starting from nanosecond pulses of moderate intensity. The use of picosecond and nanosecond pump pulse regimes with MI initiated SC generation has enabled the development of high average power, broad band SC sources. In addition, this pump regime provides easier access to a range of attractive SC properties such as a high degree of spectral flatness and relative simplicity in implementation compared to many SC systems that use mode-locked lasers[14].

Figure 1.3 illustrates our architecture for MI initiated SC generation and provides the platform for generating SC in multiple wavelength regions. This framework has been utilized by our group to demonstrate SC systems in the mid-IR, SWIR, near-IR and the visible wavelengths by selecting the appropriate gain fiber and SC generation fiber . In addition to the simplicity of implementation, this architecture for SC generation also

allows for the scalability of the SC time averaged power by simply increasing the repetition rates and the pump power in the amplifier stages.

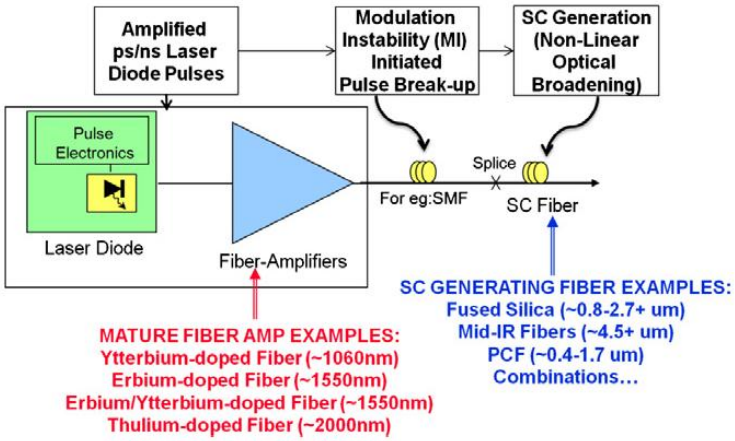


*Fig. 1.3. Architecture for MI initiated SC generation process: amplified pump pulses followed by pulse breakup in single-mode fiber followed y spectral broadening in SC fiber[14].*

All the SC systems demonstrated in our group so far, begin with ~1.5 microns picosecond/nanosecond laser diode pulses that are amplified through a series of cascaded fiber amplifier stages. These amplified pulses are then launched into a length of SMF fiber, where interaction between the nonlinearity and anomalous dispersion breaks up the quasi-CW input pulses into a train of solitons through MI and significantly increases the peak power. Thus, while many SC lasers use mode-locked femtosecond lasers to achieve high peak powers, MI enables the use of long pulses from compact laser diode sources. The generated solitons will undergo further spectral broadening in the SC fiber, due to a variety of nonlinear effects such as self phase modulation, soliton self frequency shift, Raman scattering and parametric four wave mixing. The SC fiber can then be chosen depending on the SC wavelength requirements: photonic crystal fiber (PCF) following a frequency doubler for visible wavelengths, fused silica for near-IR and SWIR wavelengths and ZBLAN for mid-IR wavelengths[14].

Due to their ability to generate light in the so -called atmospheric transmission windows[34], where losses during propagation are minimal, SC lasers are particularly attractive for applications like remote sensing and hyperspectral imaging that require long propagation distances . Figure 1.4 below shows the atmospheric transmission windows in the visible to the Mid-IR wavelength ranges. In my thesis, I focus on SC sources in the 1.5-1.8 μm and the 2-2.5 μm atmospheric windows. For long distance applications, The

beam quality/divergence, output stability and the average power of the illumination source are three important factors to consider. Infrared SC lasers have previously been studied as potential sources for hyperspectral applications [35-37], but these experiments were performed at relatively short distances of < 100m using low power SC sources. Hyperspectral imaging devices generally require the illumination of large areas and hence, high optical powers [38]. Several steps can be taken to reduce the required power of illumination, but at the cost of lower operating SNR, reduced field of view of the sensor, moving the sensor closer to the target, or a combination of both [39]. Therefore, high average power SC laser sources with near diffraction limited beams and good output stability may be key enablers for a variety of practical long distance measurements, including air borne measurements.

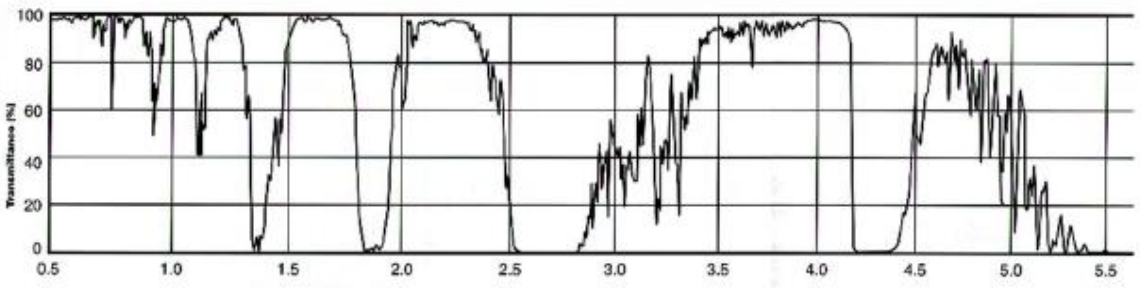


*Fig. 1.4. Atmospheric transmission window from the visible to the mid-IR wavelength range (Source: Santa Barbara Research Center)*

In Chapters 4 and 5, I will present the development of SWIR supercontinuum lasers covering the 1.5-2.5 μm wavelength regions. In chapter 4, I present the development of a 5 W SWIR SC laser prototype used to perform field trials at the Wright Patterson Air Force Base. My focus in this chapter is on long distance SC laser characterization, in terms of spectral output, beam quality ($M^2$ measurements) and output stability. I will present the results of this field trial, where the SC laser is propagated through ~1.6 km in the atmosphere and show that SC laser is nearly diffraction limited with an $M^2$ < 1.3 and the output stability to be 4-8% depending on the atmospheric turbulence effects. Finally, in order to show that there is sufficient SC signal at ~1.6 km and a potential application, diffuse spectral reflectance measurements of various samples are measured using the SC laser as the illumination source, and show good agreement with in-lab measurements performed using a conventional lamp.

In chapter 5, I shift my focus to scalability of the SC source and demonstrate an SC laser covering the 2-2.5 μm wavelength region with an average power of > 25 W in the spectrum. The results in chapter 4 indicated that the 5W SC laser is capable of maintaining a good beam quality and stability at ~1.6 km. While the laser to target distance was ~1.6 km for these measurements, the target to detector distance was ~ 2-5m. A higher average power SC could allow the detector to be placed further away from the target and possibly allow a transceiver design consisting of both the source and the detector in a single unit. In this chapter, I define three metrics for a truly scalable SC laser source as the ability to maintain a) near constant spectral output with power scaling, b) a near constant and acceptable beam quality ($M^2$ measurements) with power scaling and c) a near constant low output stability with power scaling. I show that the developed 25.7 W SC lasers satisfies all three metrics for a truly scalable system and maintains a near constant spectral output, has a near-diffraction limited beam with an $M^2$<1.2 and a radiometric variability of <0.8% across the entire spectrum, as the power is scaled from 5 to 25.7 W of SC output.

## 4. All- Fiber SC laser for Surface Roughness Measurement

Surface roughness measurements are important for a variety of applications in various industries [40-43]. Current technologies can be broadly classified as contact-based or non contact-based techniques. Stylus profilometer is the most common contact-based technique used in the industry. But, this method is limited by several factors including the stylus tip radius, lay of the surface/sample, sample curvature etc. White light interferometry is a common non-contact based technique, which is limited by the sample curvature and working distance. Thus, most of these common methods currently used are either limited by the working distance and/or the sample curvature and are not ideal for in-line measurements. On the other hand, a technique that uses reflected laser light from a sample to measure roughness has advantages of being a non contact based technique and potential for high measurement speed for in-line applications. In addition, the fiber light output can be easily collimated or focused for curved sample measurements and the high average power allows for long working distances as well [44].

In chapter 6, I demonstrate a surface roughness measurement system using a 1.2-2 μm wavelength SWIR SC laser capable of measuring roughness values in the range of ~0.05-0.35 μm, relevant for parts that are finished using lapping or polishing. The technique utilizes the wavelength dependence of reflected light on the roughness properties of the surface from which it is reflected. The system setup is explained and roughness measurements of various flat and curved samples are carried out using the SC laser. The SC measurements are also seen to be in good agreement with measurements performed using a white light interferometer and a contact based stylus profilometer, both of which are currently used in the industry. Finally, a particular application of interest to the automotive industry, in surface polish detection on crankshaft journals are carried out and the results and analysis are presented.

## References


1. C. J. Koester and E. Snitzer, "Amplification in a Fiber Laser," Appl Opt **3**, 1182 (1963).
2. V. Gapontsev and W. Krupke, "Fiber lasers grow in power," in *Laser Focus World,* (2002).
3. J. Limpert, T. Schreiber, and A. Tünnermann, "Fiber-Based High Power Laser Systems", retrieved http://www.rp-photonics.com/highpowerfiberlasers.html.
4. J. Ready and F. Zhou, "Fiber Laser Applications," in *OPTECS AND PHOTONICS SERIES,* (OP-TEC: The National Center of Optics and Photonics Education, 2011).
5. Q. Peng, A. Juzeniene, J. Chen, L. O. Svaasand, TrondWarloe, K.-E. Giercksky, and J. Moan, "Lasers in medicine," Rep. Prog. Phys. **71**, 056701 (2008).
6. K. F. Palmer and D. Williams, "Optical properties of water in the near infrared," JOURNAL OF THE OPTICAL SOCIETY OF AMERICA **64**, 1107-1110 (1974).
7. R. R. Anderson, W. Farinelli, H. Laubach, D. Manstein, A. N. Yaroslavsky, J. Gubeli, K. Jordan, G. R. Neil, M. Shinn, W. Chandler, G. P. Williams, S. V. Benson, D. R. Douglas, and H. F. Dylla, "Selective photothermolysis of lipid-rich tissues: A free electron laser study," Lasers in Surgery and Medicine **38**, 913-919 (2006).
8. A. A. Urbas and R. A. Lodder, "Near-Infrared Spectrometry in Cardiovascular Disease," in *Handbook of Near-Infrared Analysis*, D. A. Burns and E. W. Ciurzak, eds. (2008).
9. R. Muschter, "Interstitial Laser Therapy," in *Smith's Textbook of Endourology,* 3 ed., A. D. Smith, G. H. Badlani, G. M. Preminger, and L. R. Kavoussi, eds. (Blackwell Publishing Ltd, 2012).
10. F. H. Sakamoto, A. G. Doukas, W. A. Farinelli, Z. Tannous, M. Shinn, S. Benson, G. P. Williams, J. F. Gubeli, H. F. Dylla, and M. R. Rox Anderson, "Selective Photothermolysis to Target Sebaceous Glands:Theoretical Estimation of Parameters and Preliminary Results Using a Free Electron Laser," Las Surg Med **44**, 175-183 (2012).
11. S. R. Dukkipati, P. Neuzil, J. Skoda, J. Petru, A. d'Avila, S. K. Doshi, and V. Y. Reddy, "Visual Balloon-Guided Point-by-Point Ablation Reliable, Reproducible, and Persistent Pulmonary Vein Isolation," Circ Arrhythm Electrophysiol **3**, 266-273 (2010).
12. L. H. Rasmussen, M. Lawaetz, L. Bjoern, B. Vennits, A. Blemings, and B. Eklof, "Randomized clinical trial comparing endovenous laser ablation,radiofrequency ablation, foam sclerotherapy and surgical stripping for great saphenous varicose veins," British Journal of Surgery **98**, 1079-1087 (2011).
13. O. P. Kulkarni, "Single mode optical fiber based devices and systems for mid-infrared light generation, communication and metrology," (University of Michigan, PhDThesis, Ann Arbor, 2011).
14. V. V. Alexander, O. P. Kulkarni, M. Kumar, C. Xia, M. N. Islam, F. L. T. Jr., M. J. Welsh, K. Ke, M. J. Freeman, M. Neelakandan, and A. Chan, "Modulation instability initiated high power all-fiber supercontinuum lasers and their applications," Opt Fiber Tech **18**, 349-374 (2012).
15. J. S. Orringer, S. Kang, T. Hamilton, W. Schumacher, S. Cho, C. Hammerberg, G. J. Fisher, D. J. Karimipour, T. M. Johnson, and J. J. Voorhees, "Treatment of Acne Vulgaris With a Pulsed Dye Laser," JAMA **29**, 2834-2839 (2004).
16. J. I. Na and Dae Hun Suh, "Red Light Phototherapy Alone Is Effective for Acne Vulgaris: Randomized, Single-Blinded Clinical Trial," Dermatol Surg **33**, 1228-1233 (2007).
17. V. V. Alexander, P. Kevin Ke, Z. Xu, M. N. Islam, M. J. Freeman, B. Pitt, M. J. Welsh, and J. S. Orringer, "Photothermolysis of Sebaceous Glands in Human Skin Ex Vivo with a 1,708 nm Raman Fiber Laser and Contact Cooling," Las Surg Med **43**, 470-480 (2011).

18. A. S. Zelickson, J. S. Strauss, and J. Mottaz, "Ultrastructural Changes in Sebaceous Glands Following Treatment of Cystic Acne with Isotretinoin," The American Journal of Dermatology **8**, 139-143 (1986).
19. J. Goldstein, H. Comite, H. Mescon, and P. Pochi, "Isotretinoin in the treatment of acne," Arch Dematol **118**, 555-558 (1982).
20. J. S. Orringer, S. Kang, L. Maier, T. Johnson, D. Sachs, D. Karimipour, Y. Helfrich, T. Hamilton, and J. Voorhees, "A randomized, controlled, split-face clinical trial of 1320-nm Nd:YAG laser therapy in the treatment of acne vulgaris," Journal of the American Academy of Dermatology **56**, 432-438 (2007).
21. D. Y. Paithankar, E. V. Ross, B. A. Saleh, M. A. Blair, and B. S. Graham, "Acne treatment with a 1,450 nm wavelength laser and cryogen spray cooling," Lasers in Surgery and Medicine **31**, 106-114 (2002).
22. M. A. Bogle, J. S. Dover, K. A. Arndt, and S. Mordon, "Evaluation of the 1,540-nm Erbium:Glass Laser in the Treatment of Inflammatory Facial Acne," Dermatologic Surgery **33**, 810-817 (2007).
23. K. Mariwalla and T. E. Rohrer, "Use of lasers and light-based therapies for treatment of acne vulgaris," Lasers in Surgery and Medicine **37**, 333-342 (2005).
24. K. Zimmer, *Soul Made Flesh.* (Random House (Arrow Books), London, 2004).
25. W. Hamilton and D. Richards, "Output of the heart," in *Circulation of the Blood. Men and Ideas,,* A. Fishman and D. Richards, eds. (Am. Physiol. Soc, Bethesda, MD, 1982), pp. 87-90.
26. Y. Sinelnikov, S. McClain, Y. Zou, D. Smith, and R. Warnking, "Renal denervation by intravascular ultrasound: Preliminary in vivo study," AIP. Conf. Proc **1481**, 337-344 (2012).
27. G. Thomas, M. H. Shishehbor, E. L. Bravo, and J. V. Nally, "Renal denervation to treat resistant hypertension: Guarded optimism," Cleve Clin J Med **79**, 501-510 (2012).
28. D. S. Atherton, N. L. Deep, and F. O. Mendelsohn, "Micro-Anatomy of the Renal Sympathetic Nervous System: A Human Postmortem Histologic Study," Clin. Anat. **25**, 628-633 (2012).
29. H. Krum, "Catheter-based renal sympathetic denervation for resistant hypertension: durability of blood pressure reduction out to 24 months. ," Hypertension **57**, 911-917 (2011).
30. T. Mabin, M. Sapoval, V. Cabane, J. Stemmett, and M. Iyer, "First experience with endovascular ultrasound renal denervation for the treatment of resistant hypertension," Eurointervention **8**, 57-61 (2012).
31. M. Schlaich, P. Sobotka, H. Krum, E. Lambert, and M. Esler, "Renal sympathetic-nerve ablation for uncontrolled hypertension," N Engl J Med **361**, 932-934 (2009).
32. K. Steigerwald, A. Titova, C. Malle, E. Kennerknecht, C. Jilek, J. r. Hausleiter, J. r. M. N. hrig, K.-L. Laugwitz, and M. JONER, "Morphological assessment of renal arteries after radiofrequency catheter-based sympathetic denervation in a porcinemodel," J. Hypertens **30**, 2230-2239 (2012).
33. B. Avitall and H. R., "Determinants of Radiofrequency-Induced Lesion Size.," in *Radiofrequency Catheter Ablation of Cardiac Arrhythmias: Basic Concepts and Clinical Applications* 2nd ed., S. Huang and D. Wilber, eds. (Futura Publishing Company, NY, 2000), pp. 47-80.
34. C. M. Payne, "Principles of Naval Weapons systems," 2nd ed. (Naval Institute Press, Annapolis, MD, 2010).

35. T. Hakala, J. Suomalainen, S. Kaasalainen, and Y. Chen, "Full waveform hyperspectral LiDAR for terrestrial laser scanning," Opt. Express **20**, 7119-7127 (2012).
36. Y. Chen, E. Räikkönen, S. Kaasalainen, J. Suomalainen, T. Hakala, J. Hyyppä, and R. Chen, "Two-channel Hyperspectral LiDAR with a Supercontinuum Laser Source," Sensors **10**, 7057-7066 (2010).
37. R. Ceolato, N. Riviere, and L. Hespel, "Reflectances from a supercontinuum laser-based instrument: hyperspectral, polarimetric and angular measurements," Opt. Express **20**, 29413-29425 (2012).
38. C. R. Howle, D. J. M. Stothard, C. F. Rae, M. Ross, B. S. Truscott, C. D. Dyer, and M. H. Dunn, "Active hyperspectral imaging system for the detection of liquids," in *Proc. SPIE 6954,* (2008), p. 69540L
39. G. A. Shaw and H.-h. K. Burke, "Spectral Imaging for Remote Sensing," Lincoln Laboratory Journal **14**, 3-28 (2003).
40. R. M. Anderson and G. W. Neudeck, "Flatness and surface roughness of some common thin film substrate materials," J. Vac. Sci. Technol **8**, 454-457 (1971).
41. J. M. Bennett, "Measurement of the RMS roughness, autocovariance function and other statistical properties of the optical surfaces using a FECO scanning interferometer," Appl Opt **15**, 2705-2721 (1976).
42. S. Adachi, K. Horio, Y. Nakamura, K. Nakano, and A. Tanke, "Development of Toyota 1ZZ-FE engine," SAE Technical Paper series 981087 (1998).
43. S. Tung and M. L. McMillan, "Automotive tribology overview of current advances and challenges for the future," Tribol. Int. **37**, 517-536 (2004).
44. V. V. Alexander, H. Deng, M. N. Islam, J. Fred L. Terry, R. B. Pittman, and T. Valen, "Surface roughness measurement of flat and curved machined metal parts using a near infrared super-continuum laser," Opt. Eng. **50**, 113602 (2011).

# Chapter II

# Photothermolysis of Sebaceous Glands in Human Skin Ex Vivo with a 1708 nm Raman Fiber Laser and Contact Cooling: A potential Treatment for Acne

## 1. Introduction

Acne vulgaris is one of the most common dermatologic conditions, affecting the majority of people at some time in their life. It often results in significant sequelae including negative psychosocial effects. In addition, if not treated properly, acne can result in permanent scarring of the affected skin [1]. The pathogenesis of acne vulgaris has been attributed to several key factors including: a) excess sebum production, b) follicular epithelial hyperproliferation and resultant follicular plugging, c) presence of Propionibacterium acnes and production of prefatty acids and d) follicular and prefollicular inflammation [2]. Multiple treatment options have been reported to address one or more of these pathogenic elements.

Traditional medical therapy for acne remains the mainstay of therapy. Commonly employed treatments include topical retinoids, topical and oral antibiotics, benzoyl peroxide, and salicylic acid-containing agents. Severe nodulocystic acne is generally treated with oral isotretinoin, but the use of this medication is often limited by the potential for significant side effects. More recently, there has been an interest in exploring laser and light-based therapies for acne. Studies examining the use of visible light lasers and light sources, infrared lasers, broad band light sources, and photodynamic

therapy have all appeared in the recent literature [3-14]. While some research has indicated potential efficacy of these treatments, other work has demonstrated no clear benefit, and at this time, laser therapy for acne is not considered a first line treatment for most patients [15].

Given the risk profile associated with the use of isotretinoin, there is great interest in developing alternative treatments that may provide long-term improvements for even those patients with severe acne vulgaris. An ideal treatment might produce "isotretinoin-like" effects without subjecting patients to the side effects of the oral retinoid. When histology of skin samples obtained from patients on isotretinoin is examined, one major finding is the sebaceous gland atrophy and destruction that results from the use of this drug [16, 17]. Therefore, in order to produce similar clinical results to the use of isotretinoin, developing treatments that specifically target sebaceous glands is an attractive strategy.

Recently, there has been an emerging interest in lasers emitting at or near 1720 nm because of the higher absorption coefficient of lipids compared to that of water at these wavelengths [18]. A laser operating near this wavelength could allow for a greater penetration depth into the skin while selectively affecting lipid rich tissues such as sebaceous glands. Previously reported results of studies near this wavelength have employed the use of a free electron laser (FEL) [18, 19]. Thus, there has been no convenient and portable laser system emitting near this wavelength despite its potential utility.

In this chapter, I present experimental results, based on the absorption spectra of fat and penetration depth calculations in the dermis, which show that wavelengths near 1720 nm are optimum for applications targeting lipid-rich tissues such as sebaceous glands located deep into the dermis. We have developed an all fiber based Raman laser emitting at 1708 nm, constructed using commercially available telecommunications components and then performed three main studies using the 1708nm laser. First, I show histochemical evaluation of sections of treated tissues to verify the ability of the 1708 nm laser to selectively damage lipid-rich tissue. This study was performed on three tissue types, an *ex vivo* porcine heart tissue cross section consisting of pericardial adipose and myocardium, an *ex vivo* intestinal visceral fat consisting of fat with embedded blood

vessels and an *ex vivo* porcine skin tissue cross section consisting of epidermis, dermis and subcutaneous fat. For the same fluence level, the adipose tissue in the heart cross section suffered significantly more pronounced thermal damage (at least five times greater depth of damage) compared to the adjacent myocardium. Similarly, in the visceral fat treatments, the fat appears to be selectively damaged while the embedded blood vessels appear to be undamaged. In the case of porcine skin tissue cross section, no thermal damage was observed in the epidermis or dermis while the subcutaneous fat layer was seen to be thermally damaged. Then, as a potential application of the 1708 nm light for the treatment of acne by thermally damaging sebaceous glands, *ex vivo* human skin was treated, first without any surface cooling. While histological results for skin treatments without cooling showed thermal damage in the dermis at depths > 1mm, there was also clear injury to the epidermis that warranted the need for a cooling method to protect the epidermis. In the third study, a cold window based cooling method was designed and built to spare thermal damage to the epidermis during treatment. Histochemistry results for 1708 nm laser treatments on human skin with contact cooling indicated thermal damage to sebaceous glands at depths of up to ~1.65 mm into the dermis with no injury to the epidermis. Finally, in the discussion section, I compare the penetration depth and treatment mechanisms of the 1708 nm laser with some of the other common infrared lasers used in acne treatments and discuss the 1708 nm laser as a potential tool for selectively damaging lipid-rich tissues, such as sebaceous glands, for acne treatment.

## 2. Materials and Methods

This section is organized as follows. We first discuss the wavelengths near 1720 nm as the choice of wavelength for a laser designed to target adipose tissue, based on the absorption spectra for fat and water, and penetration depth calculations. We then explain the 1708 nm laser design and details for the setups used for our laser treatments. Both the porcine heart and skin tissue experiments and the human skin treatment without cooling utilized the scanning laser treatment setup, while a special setup was designed and built for human skin experiments with contact cooling. We then provide details for the three samples, porcine heart tissue, porcine skin tissue and human skin tissue with the

corresponding laser treatment parameters used in our experiments. Finally, we describe the histochemistry protocol used to visualize live versus killed tissue followed for all the samples in this paper.

### 2.1 Wavelength Selection and Penetration Depth Calculations

The desired penetration depth of light for targeting sebaceous glands should be such that it is able to affect a majority of the glands, including those located deep in the dermis. The histochemical analysis of human skin sections presented in this paper (results section) show that within skin, the sebaceous glands can be located as deep as ~1.5 – 2 mm below the skin surface. During a laser treatment, heat is immediately generated within the zone of optical penetration by the direct absorption of laser energy. This heating then subsequently decreases with tissue depth, as the incident beam is attenuated due to absorption and scattering effects.

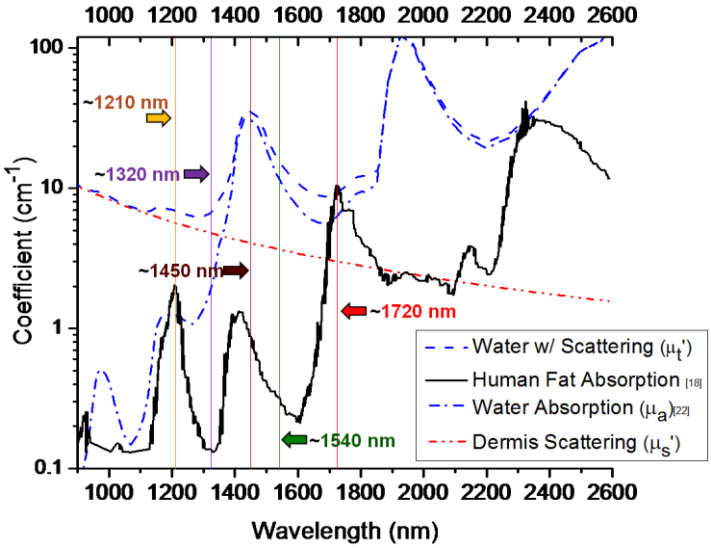


*Fig. 2.1. Infrared spectra showing the coefficients for water ($\mu_a$) and human fat absorption, effective scattering in the dermis ($\mu_s'$)and combination of water absorption with the effective scattering in the dermis ($\mu_t'$); also noted are common wavelengths of IR lasers used in acne treatments.*

For the calculations for penetration depth, I have used the Beer's law in an anisotropic media, where the fluence $\phi(z)$ falls exponentially with depth as given by $\phi(z) = \phi_0 \exp(-\mu_t' z)$; $\phi_0$ is the incident fluence, $\mu_t'$ is the reduced attenuation coefficient and $\mu_t' = \mu_a + \mu_s'$, where $\mu_a$ and $\mu_s'$ are the absorption and effective

scattering coefficients respectively [20, 21]. The penetration depth is defined as the depth at which the fluence is reduced to 1/e of the incident value and is equal to $1/\mu_t'$. Figure 2.1 shows the infrared absorption spectra for fat [18] and water [22], and the $\mu_t'$ values in the dermis which is the combination of water absorption and effective scattering loss in the dermis, calculated using the formula by Jacques [23]. Using the data from Fig. 2.1, the penetration depth at 1708 nm was calculated to be ~ 1.1 mm ($\mu_a$ ~ 6.1cm$^{-1}$, $\mu_s'$ ~3.1 cm$^{-1}$). It is worth noting that adult skin optics is quite variable in scattering properties, the degree of melanin pigmentation and amount and distribution of blood perfusion. The values used for scattering in our calculations are the average skin's optical properties [23]. We also calculated the penetration depth at 1708 nm using the data for properties of human skin samples taken from different parts of the body, provided by Troy et al [24] to be in the range of ~ 0.6 to 0.9 mm ($\mu_a$ ~ 4.3 – 6.6 cm$^{-1}$, $\mu_s'$ ~ 6.8 – 9.9 cm$^{-1}$).

The absorption spectra for fat and water in Fig. 2.1 suggest that lasers in the lipid absorption bands near 1720 nm (~ 1700-1740 nm) and 1210 nm (~ 1190-1225 nm) appear to be ideal for applications such as acne treatments that require a high enough penetration depth to thermally affect the sebaceous glands located relatively deep in the dermis. As seen in Fig. 2.1, the absorption by water greatly exceeds that of fat over majority of the spectrum except at the lipid absorption bands around 1210 nm and 1720 nm where absorption by fat exceeds that by water [18]. However, once the scattering loss in the dermis is accounted for, only the lipid absorption band around 1720 nm remains higher than that of water. In addition, fatty tissues have lower values for heat capacity and thermal conductivity which would also tend to favor the heating of fat [25]. Anderson et al have shown using photothermal excitation spectra for porcine fat and porcine skin, normalized to the FEL pulse energy, that the laser induced heating of fat at 1720 nm was ~1.7 times that of the skin; the induced heating at 1710 nm was also seen to be about the same as that at 1720 nm [18]. Sakamoto et al have also claimed that the laser (FEL) induced heating of artificial sebum was ~ 2 times that of water at 1710 nm and 1720 nm and ~1.5 times higher in human sebaceous glands compared to water at these wavelengths [19]. Fig. 2.1 shows that the absorption coefficient for fat at 1708 nm

is about five times larger than at 1210 nm and at least ten times larger than that for other commonly used IR lasers emitting at 1320 nm, 1450 nm and 1540nm, all of which have been studied as possible treatments for acne [8-14]. Thus, the wavelengths around 1720 nm (including 1708 nm) potentially have the capability to penetrate deep enough into the skin and target fat/lipid-rich tissues such as sebaceous glands including those located at depths greater than ~1 mm into the dermis, with minimum damage to the surrounding tissue.

### 2.2 1708 nm Laser Design

The experimental setup for the 1708 nm laser used in our treatments is illustrated in Fig. 2.2 and consists of two main stages: an amplified 1542 nm source followed by a Raman oscillator. The setup is made entirely of telecommunication components and fusion spliced together with no free-space elements. The 1542 nm laser is built using a ring cavity structure with an ~3.5 m long Erbium/Ytterbium co-doped fiber amplifier (EYFA) with a 12 μm/130 μm core/cladding diameter. Two 8 W 940 nm and three 10 W 976 nm heat sink-cooled multimode pump diodes are coupled into the gain fiber through a 6 x 1 pump combiner. The amplified spontaneous emission noise within the gain fiber has a peak emission at ~1542 nm and serves as the seed for the laser. The laser cavity structure is realized by feeding 1 % of the EYFA output back into the input end of the same fiber. By pumping the system with ~ 46 W average power in the counter propagation mode, a total power of ~11 W at 1542 nm was measured at the output of the first stage.

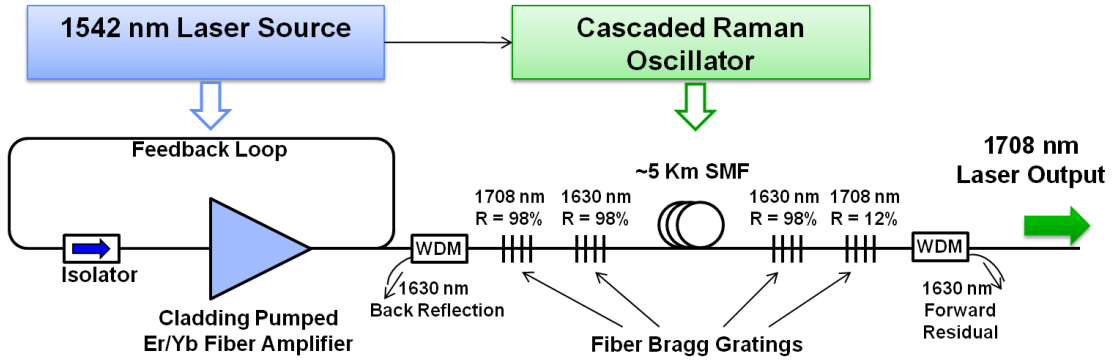


*Fig. 2.2. 1708 nm Raman fiber laser setup showing the two main stages; amplified 1542 nm source (left) and the cascaded Raman oscillator (right).*

The second stage of the 1708 nm laser is a cascaded second-order Raman oscillator. It consists of Fabry-Perot cavities composed of two sets of fiber Bragg gratings (FBGs). The FBGs are placed around a ~5 Km spool of fused silica fiber (SMF 28) which serves as the gain medium and provides sufficient Raman gain at 1708 nm. The Raman gain spectrum in fused silica fiber has a large gain bandwidth spanning over 40 THz with a dominant peak at 13.2 THz from the pump wavelength [26]. When pumped at 1542 nm, this peak gain corresponds to wavelengths of about 1654 nm and 1784 nm for the first and second-order Raman amplification wavelengths (Stokes wavelengths) and is slightly higher than the frequency down shift that is needed for our design. Therefore, in order to get a final output closer to ~ 1720 nm and based on the availability of the FBGs, the center wavelengths of the two-stage FBGs were chosen to be 1630nm and 1708nm respectively and are well within the Raman gain bandwidth. It is worth noting that it is possible to get the laser output at ~1720 nm using our design, provided that FBGs at 1720 nm are used. We chose the 1708 nm FBGs since they were the commercially available FBGs closest in wavelength to 1720 nm at the time. The center wavelengths of the FBGs provide the selective feedback for the first and second order Raman amplifications. The input FBG array is composed of a pair of high reflectivity (98%) FBGs with central wavelengths at 1630 and 1708 nm respectively, while the output FBG array is composed of a high reflectivity (98%) FBG at 1630 nm and a low reflectivity (12%) FBG centered at 1708 nm acting as the laser output coupler. The residual 1630 nm light is removed from the system using a wavelength division multiplexer added on both sides of the Raman oscillator and a 1600 nm bulk long pass filter before the final output blocks any residual pump at 1542 nm. The output spectrum of the laser was examined using an optical spectrum analyzer. We observed a sharp peak at 1708nm (3 dB bandwidth of < 1 nm), along with two small residual peaks at 1542nm and 1630nm which were lower than 15dB compared to the main laser peak at 1708 nm. A maximum time averaged power of ~4.0 W at 1708nm was measured at the output using a thermal power meter.

## 2.3 Scanning Laser Treatment Setup without Cooling

The experimental setup for the 1708 nm laser treatments without cooling is shown in Fig. 2.3. The laser output from the fiber end is collimated using an aspheric lens and has a 2 mm $1/e^2$ Gaussian beam diameter (calculated using a knife-edge measurement). A variable attenuator is placed in the beam path to adjust the laser power levels as required for the experiments. The sample of interest is mounted on to the sample holder attached to a stepper motor stage and is scanned across the laser beam. The stepper motor stage has a minimum step size of 1 micron and the desired scan rate is controlled using a computer. Scanning is done in order to increase the area of laser treatment to maximize the chance of being able to observe a laser affected region after performing the sectioning and histochemistry.

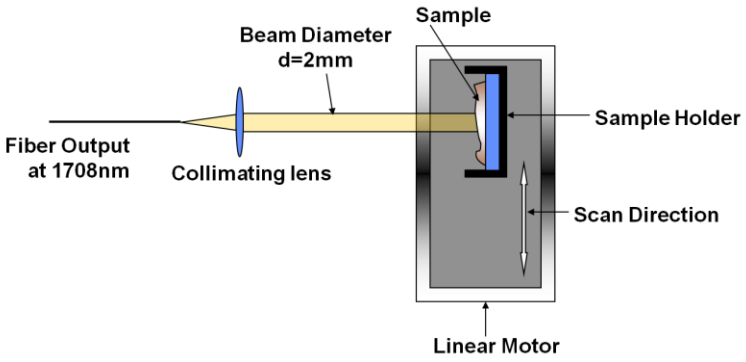


*Fig. 2.3. Scanning laser treatment setup without surface cooling. The sample is placed on a holder and scanned across the laser beam using a computer controlled stepper motor stage.*

## 2.4 Laser Treatment Setup with Contact Cooling

The cold window laser treatment setup used for *ex vivo* human skin samples is illustrated in Fig. 2.4. The laser output from the fiber is collimated using an aspheric lens to give a $1/e^2$ Gaussian beam diameter of 2mm. A special sample holder is designed to cool and protect the epidermis during treatments and is shown in Fig. 2.4. The holder is machined out of aluminum and consists of two main blocks. The first block (B1) faces the incident laser beam and is connected to two water baths using a set of tubes and valves. The water baths are kept at 37 deg C and 2 deg C, respectively and is used to cool or heat the block, as required. A sapphire window (~ 86% transmission at 1708 nm) with a diameter of ~ 2 cm is fastened on the front side of this block to allow the laser beam to be delivered to the skin samples. The sapphire window makes direct contact

with the skin surface during laser treatments. Aluminum and sapphire are both excellent conductors of heat and ensures that the surface of the skin is kept near the same temperature as the water cycled through the block. The second block (B2) of the sample holder consists of a heater incorporated into the block and set to ~ 37 deg C at all times to duplicate the temperature of the human body. Prior to laser treatment, the skin sample is placed between the two blocks of the holder with the top surface of the skin making contact with the sapphire window and the bottom surface with B2.

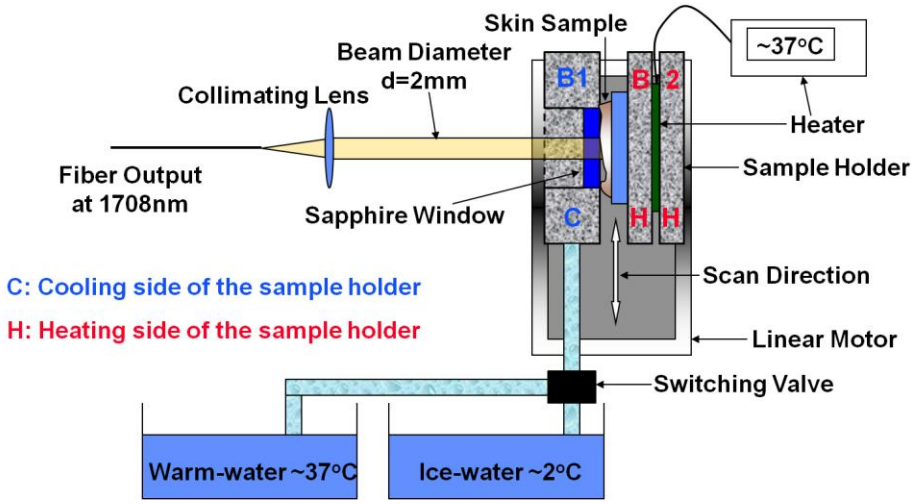


*Fig. 2.4. Ex vivo skin laser treatment setup with surface cooling to protect the epidermis. Block B2 is always kept at ~37°C and block B1 is initially kept at ~37°C and then cooled to ~2°C starting 5 seconds prior to laser exposure.*

To mimic *in vivo* conditions that human skin experiences, B1 is initially heated to ~ 37 deg C for five minutes before laser treatment. The warm water flow is then stopped and the cold water flow at ~2 deg C is started. B1 is pre-cooled for 5 seconds before starting the laser treatment and is then kept at this temperature during the laser exposure. The cooling creates a temperature gradient across the skin surface and is designed to prevent thermal damage to the skin surface during the treatments, allowing the epidermis to be spared. B1 is switched back to the warm water flow after the laser exposure to mimic restoration of skin temperature by blood flow. This procedure is then repeated for the next treatment area.

## 2.5 *Ex Vivo* Porcine Tissue Experiments

To study the efficacy of the 1708 nm laser in selectively targeting fat/lipid-rich tissues, we performed selectivity studies on two tissue types; first on an *ex vivo* porcine heart tissue cross section and then on an *ex vivo* porcine skin tissue cross section. The heart tissue cross section is comprised of two main tissue types, pericardial adipose and myocardium. Scanning the laser over the heart cross section allows for a simultaneous side by side comparison of the effects of the 1708 nm laser on the two tissue types. For our experiments, the heart tissue cross section was excised and both the pericardial fat and the myocardium were treated with the same laser fluence level.

The porcine skin tissue is comprised of epidermis, collagen rich dermis and subcutaneous fat. This is similar in nature to human skin tissue. The laser was again scanned across the cross section to provide a side by side comparison of the effects of the 1708 nm laser on the epidermis, dermis and the subcutaneous fat. For our experiments, the skin tissue cross section was excised and the epidermis, dermis and subcutaneous fat were all treated with the same laser fluence level.

The porcine heart and skin were obtained from a local butcher shop and transported to the laser lab under refrigerated conditions within hours of extraction and kept in a refrigerator at 5-7 deg C until the experiments were performed. All laser treatments were performed less than 48 hours after obtaining the porcine tissues. The tissue samples were brought to room temperature of ~23 deg C and then mounted on the scanning laser treatment setup without cooling. The tissue cross sections were then exposed to the 1708 nm laser by scanning across the laser beam. The porcine heart and skin tissue cross sections were scanned (single pass) across the 1708 nm laser (spot diameter of 2 mm) at a scan rate of 2 mm/s and a power level of 750 mW and 800 mW respectively.

## 2.6 *Ex Vivo* Human Skin Tissue Experiments

The human skin laser treatment study consisted of two parts. In the first part, the laser treatments on the skin were performed without any surface cooling using the scanning laser treatment setup. This was done to study the laser effects on the epidermis and the dermis as well as to test the need for a cold window to protect the epidermis,

while being able to cause thermal damage at depths > 1 mm into the dermis. The human skin samples were scanned (single pass) across the 1708 nm laser beam at power levels ranging from ~175 mW to 410 mW at a scan rate of 5mm/minute without any active surface cooling. In the second part, a cold window cooling method was employed using the laser treatment setup with contact cooling. Skin samples were exposed to the laser at power levels ranging from ~620 mW to 885 mW (measured before the sapphire window) for 3 seconds with a 5 second pre-cool period. These conditions correspond to a laser exposure with average fluence values ranging from ~60 J/cm$^2$ to 85 J/cm$^2$. All fluences were measured before the sapphire window. Spot exposure instead of scanning were used in this experiment to allow for the cooling and heating cycles needed by the cold window experiments.

The *ex vivo* human facial skin samples used in our study were obtained from redundant skin discarded following reconstruction of Mohs micrographic surgery defects. Skin samples were not linked to patients' identities. Tissue was obtained from the Cutaneous Surgery and Oncology unit at the University of Michigan, Department Of Dermatology. The samples were kept in Dulbecco's modified eagle medium (D-MEM), high glucose 1X (from GIBCO) and transferred under refrigerated conditions to the laser treatment lab where they were stored in a refrigerator at 5-7 deg C until the experiments are performed. The skin samples were kept in a warm water bath at ~37 deg C for about an hour prior to the laser treatments. All laser treatments were performed less than 48 hours after obtaining the skin samples.

**2.7 Histochemistry Protocol**

Following laser treatments, all samples were immediately placed in optimal cutting temperature compound (OCT$^{TM}$), frozen in liquid nitrogen and stored at -80 deg C until frozen sections could be cut. Cryostat-cut sections were made and mounted on glass slides, and stored at -80 deg C until used for histochemical staining of dehydrogenase activity.

Dehydrogenase enzyme activity is a proxy for cell viability: cells that are alive when frozen maintain dehydrogenase activity, but cells that are dead do not have this activity. In live cells that are frozen, dehydrogenase activity reduces the slightly yellow

water soluble Methylthiazolyldiphenyl-tetrazolium bromide (MTT) substrate into a water insoluble dark blue to black precipitate. Thus, in the MTT histochemical assay, live cells stain dark blue while dead cells remain clear [27]. Reduced MTT is moderately soluble in fat where the reduced compound gives a reddish-violet color.

Sections of tissue were processed for histochemical detection of mitochondrial dehydrogenase enzyme activity using MTT as a substrate. The staining method is outlined below for preparing the MTT assay and follows the protocol described in Neumann et al [28]. The incubation medium was prepared under aerobic conditions at room temperature immediately before processing.

1) 1.0 ml β-Nicotinamide adenine dinucleotide, reduced disodium salt hydrate (β – NADH) (from Sigma Aldrich, N8129), 2.5 mg/ml distilled water
2) 2.5 ml MTT (from Sigma Aldrich, M2128), 2.0 mg/ml distilled water
3) 1.0 ml phosphate-buffered saline (pH 7.4), 2.0 mg/ml
4) 0.5 ml Ringer's solution

The volume of the incubation medium was adjusted proportionally depending on the number of sections to be stained. The sections were immersed in the MTT incubation medium under aerobic conditions with no ambient light for about 30 minutes, rinsed in DI water and dried afterwards. The sections were then examined using a microscope (WILD Makroscop M420) and photos were taken using a digital camera (NIKON Coolpix 5000). The microscope magnification was set at 12.5 X for all images except for the *ex vivo* porcine skin image and the ex *vivo* human skin (treated without cooling) images which were taken at 10 X and 25 X respectively.

## 3. Experimental Results

The results section is organized as follows. We first present the results for the 1708 nm laser treatments on the porcine heart and skin tissue cross sections. In the case of porcine heart tissue, we show the ability of this laser to selectively damage the pericardial fat with minimal effect on the myocardium. Similarly, for the porcine skin tissue treatments, we show that the 1708 nm laser can selectively damage the subcutaneous fat with no damage to the dermis or the epidermis. Next, we present the results for human skin samples treated with no cooling. Histochemical analysis shows damage to the epidermis and the

dermis and verifies the need for a cooling method to be incorporated into the 1708 nm laser treatments. Finally, we present the results for the 1708 nm laser treatments on human skin with a cold window. The histochemical analysis in this case shows clear damage to sebaceous glands located as deep as ~ 1.65 mm into the dermis while sparing any injury to the epidermis.

### 3.1 *Ex Vivo* Porcine Heart Tissue Histology

The ability of the 1708 nm laser to cause selective damage to fat/lipids was verified first using a porcine heart tissue cross section. Fig 2.5 shows the histochemistry of a porcine heart tissue cross section consisting of pericardial fat and myocardium after laser exposure (750 mW, 2mm spot, single pass scanning exposure at 2mm/s scan). The laser was scanned across the cross section and both the pericardial fat and the myocardium were exposed to the same laser parameters. As shown in Fig. 2.5, the top layer of the pericardial fat extending to about 0.5 mm deep was not stained, indicating thermal damage. The myocardium on the other hand was heavily stained (blue coloration) except for the most superficial ~0.1 mm where there is perhaps somewhat decreased staining, indicating possible very shallow thermal damage. Thus, it is observed that the depth of thermal damage in the pericardial fat is at least 5 times as great as that in the myocardium. The results with the heart tissue suggest that by choosing appropriate power levels and exposure times, it would be possible to cause selective thermal damage to tissues highly enriched in fat/lipid with minimal damage to surrounding tissues (myocardium in this case) using the 1708 nm laser.

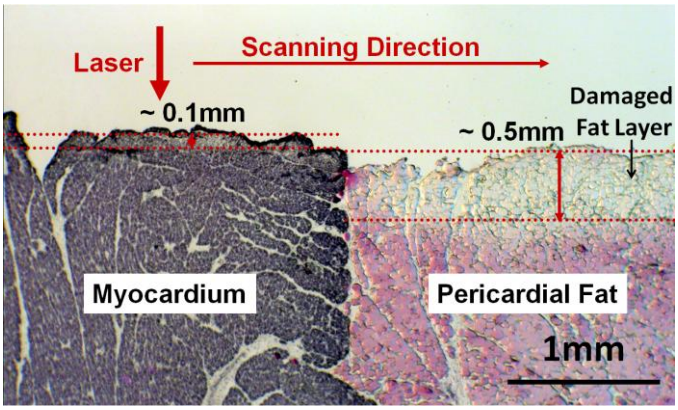


*Fig. 2.5. Histology of ex vivo porcine heart tissue cross section treated with the 1708 nm laser (2mm spot, 2mm/s scanning exposure) at 750 mW showing damage to pericardial fat with very little damage to the myocardium. Both the pericardial fat and myocardium were exposed to the same laser parameters.*

### 3.2 *Ex Vivo* Porcine Visceral Fat Histology

The ability of the 1708 nm laser to selective target and damage fat is further verified by treating samples of porcine visceral fat obtained from the intestine. Figure 2.6 shows the histochemistry of a porcine visceral fat cross section consisting of fat and embedded blood vessels after laser exposure (600mW, 2 mm spot, single pass scanning exposure at 2mm/s scan.). The laser was scanned across the entire cross sections and both fat and blood vessels were exposed to the same laser parameters. As seen in Fig. 2.6, the fat layer up to ~1.6 mm is not stained and indicated thermal damage. However, the blood vessels within this depth treated with the laser are stained and showed no indication of thermal damage. Thus, the results with the porcine visceral fat show a clear evidence of the selective lipid targeting ability of the 1708 nm laser.

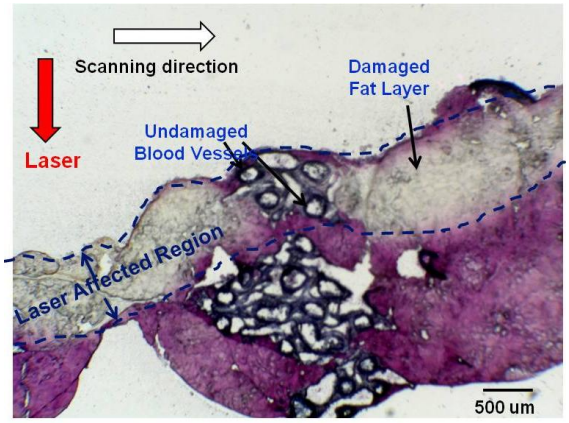


*Fig. 2.6. Histology of ex vivo porcine intestinal visceral fat cross section treated with the 1708 nm laser (2mm spot, 2mm/s scanning exposure) at 600mW showing damage to the fat with no damage to the embedded blood vessels. The fat and the blood vessels were all exposed to the same laser parameters.*

### 3.3 *Ex Vivo* Porcine Skin Tissue Histology

In order to verify the fat/lipid targeting ability of the 1708 nm laser in a tissue similar to human skin i.e. with more collagen content, we also performed the 1708 nm laser treatments across a cross section of porcine skin. Fig. 2.7 shows the histochemistry of a porcine skin tissue cross section consisting of the epidermis, collagen rich dermis and subcutaneous fat, after laser exposure (800 mW, 2 mm spot, and single pass scanning exposure at 2mm /s scan). The laser was again scanned across the cross section and the epidermis, dermis and the subcutaneous fat were all exposed to the same laser parameters. As seen in Fig. 2.7, the subcutaneous fat layer was not stained to a depth of

about 0.6 mm and indicates thermal damage. On the other hand, the epidermis and the collagen rich dermis were well stained and showed no indication of thermal damage at this fluence. Thus, the results with the porcine skin tissue, like the heart tissue results, suggest that by choosing appropriate laser power and exposure levels, it would be possible to selectively damage fat/lipid-rich tissues with little to no damage to the surrounding tissues (dermis and epidermis in this case) using the 1708 nm laser.

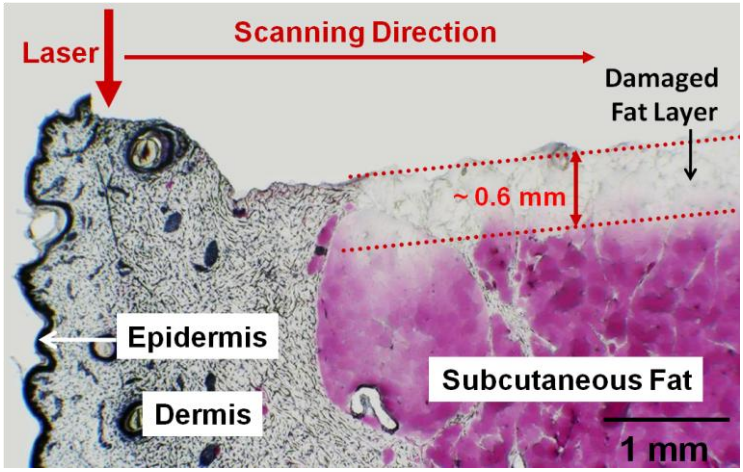


*Fig. 2.7. Histology of ex vivo porcine skin tissue cross section treated with the 1708 nm laser (2mm spot, 2mm/s scanning exposure) at 800mW showing damage to the subcutaneous fat with no damage to the epidermis or the dermis. The epidermis, dermis and the subcutaneous fat were all exposed to the same laser parameters.*

### *3.4 Ex Vivo* Human Skin Histology without Surface Cooling

Once the preferential targeting of adipose by the 1708 nm laser was verified by the porcine heart and skin tissue results, the next step was to use the 1708 nm laser to damage sebaceous glands in human skin. The human skin treatments were first performed without any cooling of the surface to study the effects on the epidermis and the dermis. Fig. 2.8 shows the histochemistry in a section of human skin after 1708 nm laser exposure and no cooling at A) 375 mW, 2 mm spot, single pass scanning exposure at 5 mm/min and B) 275 mW, 2 mm spot, single pass scanning exposure at 5 mm/min. The areas in the figure that are not stained (whitish region) indicate thermal damage. The zone of thermal damage extends to a depth of ~1.1 mm and ~ 0.9 mm into the dermis in Fig. 2.8 (a) and (b) respectively. The sebaceous glands in this region are seen to be damaged. The epidermis is also seen to be damaged in both cases. The top inset in Fig. 2.8 (a) shows an example of a partially damaged sebaceous gland and the bottom inset

shows an undamaged sebaceous gland for comparison. Similarly, the top and bottom insets in Fig. 2.8 (b) show a damaged and undamaged sebaceous gland respectively. This result shown in Fig. 2.8 verified that without cooling the epidermis, causing sufficient thermal damage in the dermis at depths of $\geq 1$ mm to affect sebaceous glands would also significantly damage the epidermis. The sebaceous glands in Fig. 2.8 were measured to be located as deep as ~1.5 mm from the skin surface.

Figure 2.8 also shows some indication of selective damage of the sebaceous glands towards the outermost regions of the laser damage area. The laser beam used in the experiments is a Gaussian beam and gives rise to the damage profile shown in Fig. 2.8. The maximum depth of damage occurs at the peak of the Gaussian beam where the beam intensity is highest and this depth of damage decreases away from the center of the beam. Thus, for the histochemical sections shown in Fig. 2.8, there is a gradient of laser energy levels along the boundary of the damaged area. The portion of sebaceous glands at the boundary of the clearly damaged dermal area in Fig. 2.8 seems to be thermally affected but the surrounding dermal connective tissue (marked as live cells in the figure) along the same boundary looks unaffected. Selectivity issues will be commented on further in the discussion section.

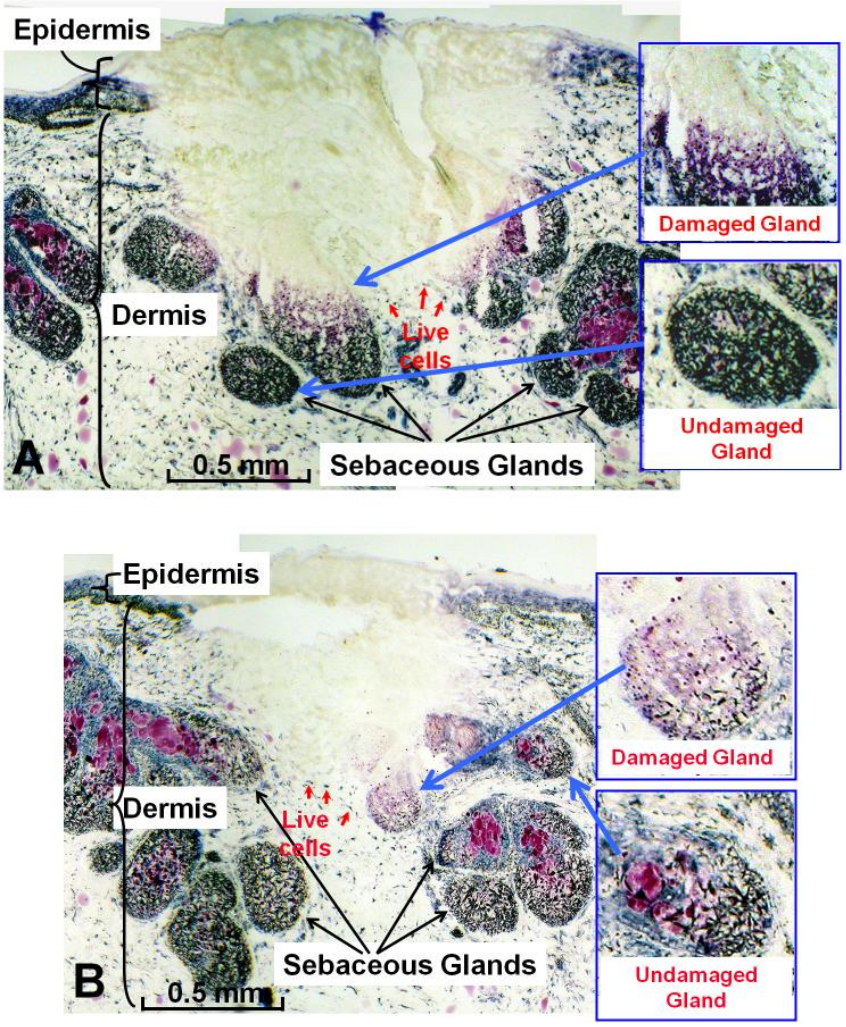


*Fig. 2.8. Histology of ex vivo human skin treated with 1708 nm laser (2mm diameter spot and 5 mm/min scanning exposure) at (a) 375mW and (b) 275mW showing thermal damage to the epidermis and dermis, extending to ~ 1mm into the dermis from the skin surface; insets show damaged and undamaged sebaceous glands.*

### 3.5 *Ex Vivo* Human Skin Histology with Active Surface Cooling

The results from the skin treatments without any cooling demonstrated the need for a cooling technique to be incorporated into the treatment, in order to spare the epidermis. Thus, the laser treatment of skin with the application of a cold window was examined. Figure 2.9 shows the MTT histochemistry of human skin treated with 1708 nm laser (5 seconds pre-cool; 2mm diameter spot exposure for 3 seconds) at 725 mW (A, B) corresponding to ~70 J/cm$^2$ average fluence, and 830 mW (C, D) corresponding to ~80 J/cm$^2$ average fluence. The images in Fig 2.9 show that the application of a cold window was effective in protecting the epidermis which is clearly undamaged as

indicated by the MTT staining. In contrast, thermal damage to the dermis has occurred. At 70 J/cm$^2$ (panels A and B) thermal damage extends to ~1.3 and 1.4 mm respectively from the skin surface. At 80 J/cm$^2$ (panels C and D) thermal damage was measured to be as deep as ~1.4 and ~1.65 mm respectively, into the dermis. Sebaceous glands within this region of the dermis are not stained, indicating that they suffered thermal damage by the 1708 nm laser. Figure 2.9 also provides a clear comparison between damaged and undamaged sebaceous glands as indicated by the MTT histochemical procedure. Again, the laser beam used in the treatments is Gaussian and the maximum depth of thermal damage seen in Fig. 2.9 corresponds to the peak of this Gaussian beam. The application of the cold window has spared any injury to the epidermis and the dermal tissue at depths of ~0.3 – 0.4 mm from the skin surface. While the sebaceous glands in Fig. 2.9 (a) and (b) were measured to be as deep as ~1.5 mm from the skin surface, the sebaceous glands in Fig. 2.9 (C) and (D) were seen to be located as deep as ~2mm from the skin surface.

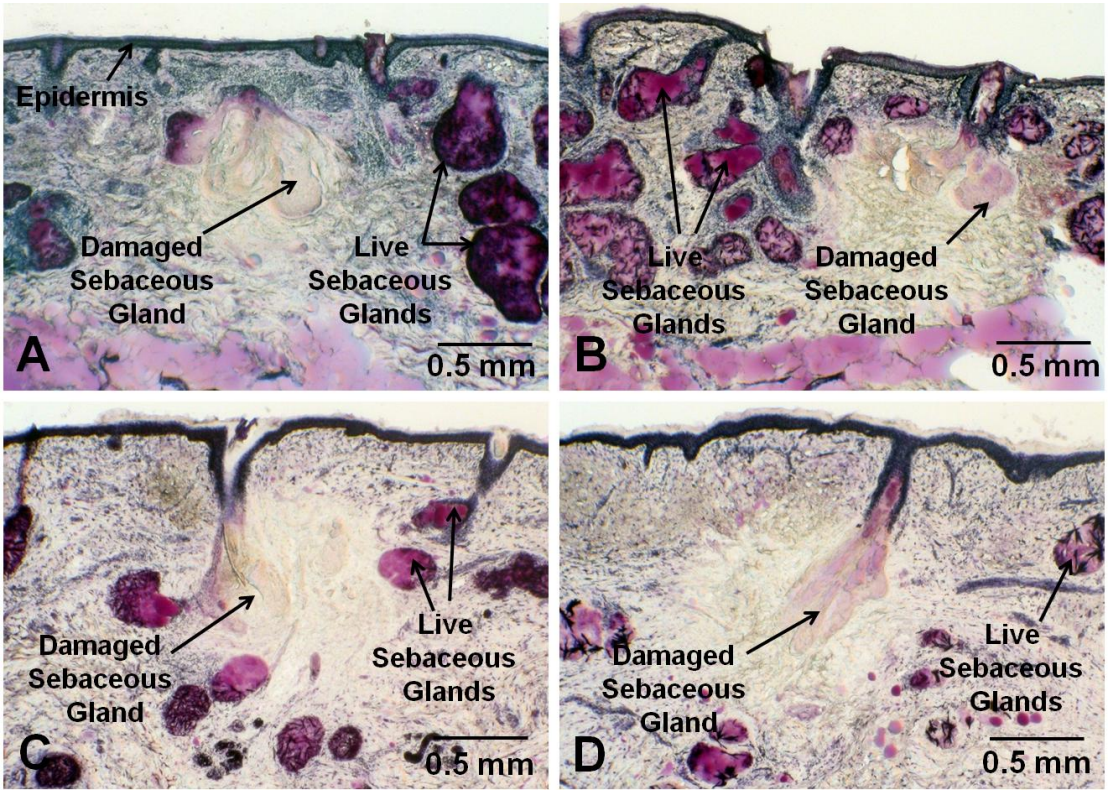


*Fig. 2.9. MTT histochemistry of ex vivo human skin treated with 1708 nm laser and cold window (5 seconds pre-cool; 2mm diameter spot exposure for 3 seconds) at 725 mW (A, B) corresponding to ~70 J/cm$^2$ average fluence and 830 mW (C, D) corresponding to ~80 J/cm$^2$ average fluence.*

Figure 2.10 plots the maximum depth of damage we were able to measure in the dermis from the MTT histochemistry, for a range of 1708 nm average fluences with the application of the cold window. Depth of damage ranged from ~1.25 mm to 1.65 mm for the six different treatment areas at average fluences ranging from 65-80 J/cm$^2$ (5 s pre-cool; 2 mm diameter spot exposure for 3 s). One possible reason for the difference between the maximum depth of damage for the two sets of treatment areas each at 70 and 80 J/cm$^2$, respectively, as shown in Fig. 2.10 could be explained by the sectioning process used for histology. We retained one 20 micron section of the sample for every 100 microns and, therefore, it is possible to have passed over the section with the largest depth of thermal damage corresponding to the peak of the laser beam (Gaussian beam) used in the treatments. It is also possible that there were small differences in the skin thickness and composition that could have affected the depth of thermal damage for a given fluence level. We did not observe any noticeable damage to the sebaceous glands or the surrounding dermis at an average fluence of ~60 J/cm$^2$. For treatments at an average fluence of ~85 J/cm$^2$, we observed significant thermal damage to both the sebaceous glands and the surrounding dermal tissue but the epidermis remained undamaged. The data in Figs. 2.9 and 2.10 show that it is possible to cause thermal damage to sebaceous glands located at depths of up to ~1.65 mm from the surface of the epidermis, using light at 1708 nm while avoiding injury to the epidermis by the application of a cold window during laser treatment.

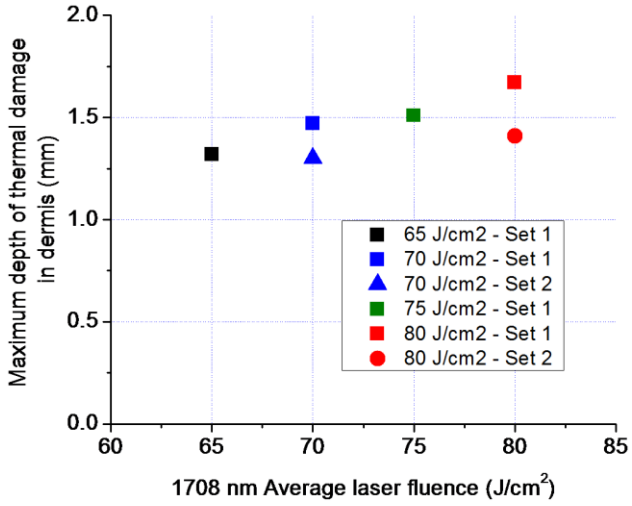


*Fig. 2.10. Maximum depth of thermally induced damage in the dermis as measured from MTT histochemistry results at different 1708 nm average fluences.*

## 4. Discussion and Conclusions

A number of infrared treatments for acne have been reported in the literature, particularly at wavelengths of 1450 nm, 1540 nm and 1320 nm [8-14]. These wavelengths target the water content in the dermis and cause non-specific thermal damage including injury to sebaceous glands, but this effect on sebaceous glands was seen to be quite transient [8, 9]. In addition, lasers at 1450 nm and 1540 nm have been reported to have a calculated penetration depth in skin ranging from ~ 300 - 600 microns [9, 11, 13], making these wavelengths theoretically less effective at targeting sebaceous glands located deeper into the dermis. It is interesting to note that 1320 nm laser has a calculated penetration depth of ~1.5 mm [12]. However, there is a low absorption coefficient for fat coupled with high scattering loss at this wavelength, as shown in Fig. 2.1. This would indicate that a much higher energy and a larger volume of tissue would need to be heated to cause sufficient thermal alteration of the sebaceous glands to be of clinical significance as compared to the other, longer wavelength infrared lasers noted above [29].

The lipid absorption band at 1210 nm is also of interest for applications targeting lipid- rich tissues as suggested from the absorption spectra for fat and water in Fig 2.1. Anderson et al have shown that it is possible to cause damage to the subcutaneous fat of porcine tissues with little or no injury to the overlying skin using a FEL at wavelengths near 1210 nm delivered through a cold sapphire window [18]. It is worth noting that once scattering in the dermis is accounted for, the combination of water absorption and scattering effects in the dermis is larger than the fat absorption at 1210 nm, as shown in Fig 2.1. The data is Fig. 2.1 also suggests that the penetration depth at ~1210 nm would then be only slightly higher than that at ~1720 nm. However, the absorption for fat at ~1720nm is about five times larger than at ~1210 nm and still above the combination of water absorption and dermis scattering at ~ 1720 nm indicating that wavelengths around ~1720 nm might be better suited for applications targeting fat/lipid rich tissues.

In this study, a laser source at 1708 nm, in the lipid absorption band near ~1720 nm was developed and used to study the effectiveness of this wavelength to target lipids and cause thermal damage to sebaceous glands located relatively deep in the dermis, as a potential treatment for acne. An approach using a wavelength such as 1708 nm, which is

preferentially absorbed by lipids, could be more effective in destroying sebaceous glands and improving conditions like acne vulgaris. The *ex vivo* porcine heart tissue results in Fig 2.5 show that, when the pericardial fat and myocardium are treated with the same 1708 nm laser fluence, the pericardial fat is selectively damaged with minimum damage to the myocardium. Similarly, the ex vivo porcine intestinal visceral fat results in Fig. 2.6 clearly show the ability of the 1708 nm laser to selectively damage fat without damaging the embedded blood vessels. Finally, the *ex vivo* porcine skin tissue results in Fig 2.7 show that for the same 1708 nm laser fluence exposure across the tissue cross section, the subcutaneous fat layer is selectively damaged, with no damage to the dermis and the epidermis. This would indicate that it should be possible to cause selective thermal damage to lipid rich tissues with minimum damage to the surrounding tissues by choosing optimal treatment parameters, including selection of a specific wavelength as with the 1708 nm laser used in our study.

The penetration depth into the dermis is another factor to consider, besides preferential absorption, when attempting to effectively damage sebaceous glands located deep in the dermis. As the absorption spectra in Fig. 2.1 show, 1708 nm is a near optimum wavelength of operation for this goal since it corresponds to a local water absorption trough, allowing for a sufficient penetration depth, and a lipid absorption peak, allowing for selective absorption of energy by sebaceous glands. Our histochemistry results in Figs. 2.8 and 2.9 show that a majority of the sebaceous glands are located within ~1.5 mm into the dermis and can even extend to ~ 2 mm from the skin surface in some cases. We calculated the penetration depth in skin of 1708 nm light to be ~ 1.1 mm, and our results in Figs. 2.9 and 2.10 indicate a maximum depth of thermal damage zone in the dermis of up to ~1.65 mm from the skin surface for an average fluence of ~80 J/cm$^2$. The results in Fig. 2.9 indicate that it is possible to cause thermal damage to majority of the sebaceous glands in human skin using the 1708 nm laser while sparing the epidermis by applying a cold window. The cold window parameters used in our study was able to spare the epidermis and ~0.3 to 0.4 mm of the dermis from the skin surface. It should also be possible to modify the cooling parameters to adjust the spared-tissue depth within some range if required.

The absorption spectra for fat and water also suggest that it should be possible to cause selective damage to lipid rich tissues like sebaceous glands at wavelengths around ~1720 nm. In addition, since the laser beam used for the *ex vivo* human skin treatments was Gaussian in nature, there was a gradient of laser energy level along the boundary of the damaged area in a given histological section. It was expected then, that there would be some indication of selectivity for sebaceous gland damage. However, the evidence for selectivity is not clear in our histology sections. Certainly, sebaceous glands are efficiently destroyed by laser exposure, but surrounding dermal tissue at a similar depth also appeared to be thermally altered in most cases. While the absorption coefficient for lipids around 1720 nm is greater than that for water, the ratio of the absorption coefficient for water and lipid is still small. Since sebaceous glands should cool more slowly than the surrounding skin after laser exposure, it might be possible to optimize treatment parameters for selective destruction of the gland [29]. For example, increased selectivity and thus more efficient sebaceous gland destruction may also be achievable with altered pulse durations [19]. Further research examining the effects of altered treatment parameters is warranted. Finally, it is worth noting that type I collagen also has an absorption peak at ~1720 nm [30]. Since there is a significant amount of collagen in the dermis, its presence might also affect the therapeutic window for causing selective damage to the sebaceous glands in human skin.

In summary, we have developed an all fiber based Raman laser source at 1708 nm, a wavelength near the lipid absorption peak at ~1720 nm, capable of thermally damaging sebaceous glands located deep into the dermis. The 1708 nm laser is shown to be effective in selectively targeting and thermally damaging fat/lipid rich tissues as indicated by the *ex vivo* porcine heart and porcine skin tissue results. Thermal damage to sebaceous glands at depths up to ~1.65 mm (at an average fluence of 80J/cm$^2$) in human skin without apparent injury to the epidermis is also demonstrated using the 1708 nm laser and contact cooling. These results indicate that the 1708 nm laser may offer a more efficient way to target lipid-containing structures in the skin and, thus, imply the potential use of this device as a better approach to the treatment of acne vulgaris. Further research and clinical studies using the 1708 nm laser are warranted to determine the optimal

treatment parameters for selective destruction of sebaceous glands and to evaluate the efficacy of the 1708 nm laser as a potential therapy for the treatment of acne.

## References


1. A. S. Glaich, P. M. Friedman, M. H. Jih, and L. H. Goldberg, "Treatment of inflammatory facial acne vulgaris with combination 595-nm pulsed-dye laser with dynamic-cooling-device and 1,450-nm diode laser," Lasers in Surgery and Medicine 38, 177-180 (2006).
2. J. C. Harper, "An update on the pathogenesis and management of acne vulgaris," J Am Acad Dermatol 51, S36-S38 (2004).
3. W. P. Baugh and W. D. Kucaba, "Nonablative Phototherapy for Acne Vulgaris Using the KTP 532 nm Laser," Dermatol Surg 31, 1290-1296 (2005).
4. S.-E. Chang, S.-J. Ahn, D.-Y. Rhee, J.-H. Choi, K.-C. Moon, and H.-S. Suh, "Treatment of Facial Acne Papules and Pustules in Korean Patients Using an Intense Pulsed Light Device Equipped with a 530- to 750-nm Filter," Dermatologic Surgery 33, 676-679 (2007).
5. T.-Y. Tzung, K.-H. Wu, and M.-L. Huang, "Blue light phototherapy in the treatment of acne," Photodermatol Photoimmunol Photomed 20, 266-269 (2004).
6. J. I. Na and D. H. Suh, "Red Light Phototherapy Alone Is Effective for Acne Vulgaris: Randomized, Single-Blinded Clinical Trial," Dermatologic Surgery 33, 1228-1233 (2007).
7. J. S. Orringer, D. L. Sachs, E. Bailey, S. Kang, T. Hamilton, and J. J. Voorhees, "Photodynamic therapy for acne vulgaris: a randomized, controlled, split-face clinical trial of topical aminolevulinic acid and pulsed dye laser therapy," Journal of Cosmetic Dermatology, 9, 28-34 (2010).
8. K. Mariwalla and T. E. Rohrer, "Use of lasers and light-based therapies for treatment of acne vulgaris," Lasers in Surgery and Medicine 37, 333-342 (2005).
9. D. Y. Paithankar, E. V. Ross, B. A. Saleh, M. A. Blair, and B. S. Graham, "Acne treatment with a 1,450 nm wavelength laser and cryogen spray cooling," Lasers in Surgery and Medicine 31, 106-114 (2002).
10. M. Jih, P. Friedman, L. Goldberg, M. Robles, A. Glaich, and A. Kimyaiasadi, "The 1450-nm diode laser for facial inflammatory acne vulgaris: Dose-response and 12-month follow-up study," Journal of the American Academy of Dermatology 55, 80-87 (2006).
11. E. V. Ross, F. P. Sajben, J. Hsia, D. Barnette, C. H. Miller, and J. R. McKinlay, "Nonablative Skin Remodeling: Selective Dermal Heating with a Mid-infrared Laser and Contact Cooling Combination," Lasers in Surgery and Medicine 26, 186-195 (2000).
12. S. Dahan, J. M. Lagarde, V. Turlier, L. Courrech, and S. Mordon, "Treatment of Neck Lines and Forehead Rhytids with a Nonablative 1540-nm Er:Glass Laser: A Controlled Clinical Study Combined with the Measurement of the thickness and the Mechanical Properties of the Skin," Dermatol Surg 30, 872-880 (2004).
13. M. A. Bogle, J. S. Dover, K. A. Arndt, and S. Mordon, "Evaluation of the 1,540-nm Erbium:Glass Laser in the Treatment of Inflammatory Facial Acne," Dermatologic Surgery 33, 810-817 (2007).
14. J. S. Orringer, S. Kang, L. Maier, T. Johnson, D. Sachs, D. Karimipour, Y. Helfrich, T. Hamilton, and J. Voorhees, "A randomized, controlled, split-face clinical trial of 1320-nm Nd:YAG laser therapy in the treatment of acne vulgaris," Journal of the American Academy of Dermatology 56, 432-438 (2007).

15. J. S. Orringer, S. Kang, T. Hamilton, W. Schumacher, S. Cho, C. Hammerberg, G. J. Fisher, D. J. Karimipour, T. M. Johnson, and J. J. Voorhees, "Treatment of Acne Vulgaris With a Pulsed Dye Laser," JAMA: The Journal of the American Medical Association 291, 2834-2839 (2004).
16. A. S. Zelickson, J. S. Strauss, and J. Mottaz, "Ultrastructural Changes in Sebaceous Glands Following Treatment of Cystic Acne with Isotretinoin," The American Journal of Dermatology 8, 139-143 (1986).
17. J. Goldstein, H. Comite, H. Mescon, and P. Pochi, "Isotretinoin in the treatment of acne," Arch Dematol 118, 555-558 (1982).
18. R. R. Anderson, W. Farinelli, H. Laubach, D. Manstein, A. N. Yaroslavsky, J. Gubeli, K. Jordan, G. R. Neil, M. Shinn, W. Chandler, G. P. Williams, S. V. Benson, D. R. Douglas, and H. F. Dylla, "Selective photothermolysis of lipid-rich tissues: A free electron laser study," Lasers in Surgery and Medicine 38, 913-919 (2006).
19. F. H. Sakamoto, A. Doukas, W. Farinelli, Z. Tannous, M. Shinn, S. Benson, G. Williams, F. Dylla, and R. R. Anderson, "Selective Photothermolysis to Target Sebaceous Glands," American Society for Laser Medicine and Surgery Abstracts (2008).
20. D. J. Maitland, J. T. Walsh Jr, and J. B. Prystowsky, "Optical properties of human gallbladder tissue and bile," Applied Optics 32, 586-591 (1993).
21. O. F. Stumpp, A. J. Welch, T. E. Milner, and J. Neev, "Enhancement of transepidermal skin clearing agent delivery using a 980 nm diode laser," Lasers in Surgery and Medicine 37, 278-285 (2005).
22. K. F. Palmer and D. Williams, "Optical properties of water in the near infrared," JOURNAL OF THE OPTICAL SOCIETY OF AMERICA 64, 1107-1110 (1974).
23. S. L. Jacques, "http://omlc.ogi.edu/news/jan98/skinoptics.html" (1998), retrieved.
24. T. L. Troy and S. N. Thennadil, "Optical properties of human skin in the near infrared wavelength range of 1000 to 2200 nm," Journal of Biomedical Optics 6, 167-176 (2001).
25. T. A. Balasubramaniam and H. F. Bowman, "Thermal Conductivity and Thermal Diffusivity of Biomaterials: A Simultaneous measurement Technique," Journal of Biomechanical Engineering 99, 148-154 (1977).
26. M. N. Islam, "Raman Amplifiers for Telecommunications 1 Physical Principles," in *Springer Series in Optical Sciences*, W.T. Rhodes, ed. (Springer, 2004).
27. T. Mosmann, "Rapid Colorimetric Assay for Cellular Growth and Survival: Application to Proliferation and Cytotoxicity Assays," Journal of lmmunological Methods, 65, 55-63 (1983).
28. R. A. Neumann, R. M. Knobler, F. Pieczkowski, and W. Gebhart, "Enzyme histochemical analysis of cell viability after argon laser-induced coagulation necrosis of the skin," Journal of the American Academy of Dermatology 25, 991-998 (1991).
29. E. V. Ross Jr and N. Uebelhoer, "Acne," in *Lasers and Lights*, D. J. Goldberg, ed. (Elsevier Saunders, 2005).
30. A. A. Urbas and R. A. Lodder, "Near-Infrared Spectrometry in Cardiovascular Disease," in *Handbook of Near-Infrared Analysis*, D. A. Burns and E. W. Ciurzak, eds. (2008).

# Chapter III

# Renal Denervation Using Focused Infrared Fiber Lasers: A potential Treatment for Hypertension

## 1. Introduction

In this chapter, we demonstrate a novel technique for renal denervation using focused infrared fiber lasers. Both *in vitro* and *in vivo* treatments are performed and the histochemistry results are presented. The histochemistry results show that focusing the laser can cause adventitial damage without injuring the endothelium. Three laser wavelengths at 980 nm, 1210 nm and 1700 nm are studied as candidates for renal denervation based on the absorption spectral and penetration depth calculations. While all three wavelengths are capable of damaging renal nerves, only 980 nm and 1210 nm lasers show evidence of penetrating deep enough to cause nerve damage, while also saving the endothelium. *In vitro* results also suggest that the effect of focusing is attenuated as the wavelength dependent absorption in tissue increases. We also perform *In vivo* renal denervation in sheep using a designed laser catheter prototype. *In vivo* results show evidence of transmural renal artery (including nerves) damage at depths of > 1.5 mm from the lumen wall. Some sections also show damage to the media/adventitia at depths of > 1mm without any apparent injury to the endothelium. However, in these cases, there are no clearly identifiable nerves or the damage does not extent deep enough due to non optimum treatment parameters. The position of the catheter and the focus in the renal artery cross section is a critical factor to consider in this treatment. In our current trials, the catheter capabilities are limited and have no maneuverability once inside the artery. We also discuss some of the possible catheter improvements and treatment parameters that could make focused infrared lasers

an attractive energy source for renal denervation, where it might be possible to damage the renal nerves with little to no damage to the endothelium and other non target artery tissues.

Hypertension is a major public health concern with an estimated one third of the adult population in the developed world suffering from this condition [1, 2]. Despite the availability of numerous effective pharmacologic agents and efforts to diagnose hypertension, only half of the treated patients are controlled to established blood pressure (BP) targets [2-4]. Effective pharmacology treatments may be limited by various factors such as patient adherence, physician inertia, inadequate doses, inappropriate combination s of antihypertensive drugs, noncompliance with dietary restrictions, side effects of medications and drug ineffectiveness [5-7].Thus, the development of new approaches for the management of hypertension that could potentially overcome these issues is a priority, especially for patients with so-called resistant hypertension, i.e. patients unable to achieve target BP values despite multiple drug therapies at the highest tolerated dose and are at a high risk of major cardiovascular events [8, 9]. A variety of studies have been performed, which suggests that hyper activation of the sympathetic nervous system plays an important role in initiating and maintaining hypertension [5, 10]. Sympathetic nerve fibers innervate all organs involved in cardiovascular control such as the heart, peripheral blood vessels and the kidneys. The sophisticated network of efferent (brain to kidney) and afferent (kidney to brain) sensory nerve fibers residing in the kidney and their signaling pathways provide the basis for the influence of integrative structures in the brain stem on renal effectors contributing to BP control [10]. An increase in the renal sympathetic nerve activity is suggested as a contributing factor in the development and maintenance of hypertensive states [11]. Studies of renal denervation in animals performed using surgical and chemical techniques, have also further helped to establish the roles of renal sympathetic nerves in hypertension [12, 13].

Recently, a minimally invasive radiofrequency (RF) ablation catheter based approach has been developed and used for renal denervation [8, 14]. In this procedure, a specially designed catheter is inserted into the femoral artery and advanced into one of the renal arteries and the RF energy is applied to the endoluminal surface to deliver thermal injury to the renal sympathetic nerves. The procedure is performed on both sides

with four to six sites ablated in a longitudinal and rotational manner at each site to cover the full circumference [5]. Clinical studies have also been performed to assess the safety and efficacy of a percutaneous catheter based approach, designed to ablate renal sympathetic nerves using an RF generator via the lumen of the main renal artery (Symplicity$^{TM}$ , Medtronic, CA, USA). In a safety and proof of principle study and in a separate randomized trial, this approach was shown to reduce blood pressure successfully, without serious adverse events in patients with resistant hypertension [8, 14]. Durability of treatment effect up to two years has also been reported in a cohort of 153 patients with resistant hypertension treated using the catheter based RF denervation technique [15]. Recent publications have also confirmed the efficacy of renal denervation for the treatment of resistant hypertension [16-18].

Although well received by clinicians, there are limitations of renal denervation using the RF technique[19]. Procedural limitations include the catheter instability, triggering frequent treatment interruptions and the overall duration of the procedure, which consists of a minimum of eight two minute ablations, the time required to reposition the device continuously and the associated patient discomfort or pain [20]. While further research is necessary to assess long term safety and efficacy of RF denervation, an underlying mechanism to cause renal denervation using RF has been attributed to a localized temperature rise or hyperthermia [21]. Morphological assessment of porcine renal arteries after RF denervation show acute transmural tissue coagulation and loss of endothelium resulting in local thrombus formation [22]. Vascular smooth muscle cells express what is called tissue factor (TF), a protein on their surfaces. Endothelial cells cover the smooth muscle cells in the renal artery preventing exposure of TF to proteins in the blood that initiate the clotting cascade. When endothelial cells are killed and removed from the wall, TF becomes accessible to clotting factors often resulting in thrombus formations [23-25]. While sub acute and longer term studies of RF renal denervation show almost completely re-endothelialized lumen, a treatment modality for renal denervation minimizing the duration of treatments and the acute loss of endothelium and or/damage to non target tissues would be desirable.

The experience with thermal injury to the endothelium and other non-target tissues has generated an interest in the exploration of alternative ablative energy forms.

Recently, ultrasound therapy has been investigated as an alternate suitable modality for denervation of renal nerves [20, 21]. Clinical trials have also been performed investigating the use of ultrasound (Paradise$^{TM}$, ReCor Medical,NY,USA) for renal denervation. In this case, a percutaneous catheter based approach is used and consists of a cylindrical transducer that emits ultrasound energy circumferentially, once in the renal artery. A water balloon in the catheter is used to center the transducer in the artery and to cool the arterial wall to minimize damage to the endothelium and non-target tissue. Preliminary clinical study using this technique have been performed on a cohort of 11 patients, where an average of 5.1 ultrasound emissions was delivered in each subject for a total treatment duration of less than four minutes and indicate ultrasound therapy to be a promising treatment for resistant hypertension [20].

Laser treatments are another alternative energy form widely used for a variety of medical therapeutic and diagnostic applications [26] . The availability of fiber coupled laser devices with sufficient average powers have also led to the development of minimally invasive catheter based medical treatments as well [26-29] . Fiber lasers are potentially advantageous for renal denervation over other ablation techniques for the following reasons. Lasers can be easily collimated or focused to get a better control of the treatment area. Focusing the laser could also help in creating a temperature gradient along the depth of the treatment site, making it possible to damage target structures like the renal nerves with minimal injury to the endothelium and other non-target structures without the use of an external cooling mechanism. It is also possible to choose an optimum laser wavelength depending on the treatment requirements. For renal denervation, the wavelength must be capable of penetrating deep enough to reach the renal nerves (~2 mm), but not too deep to damage the abdominal, pelvic or other lower extremity nerves. In addition, choosing a wavelength that can target specific tissue components can help in achieving selective tissue damage. For example, reports of selectivity using a ~1700nm laser for targeting lipid rich sebaceous glands in human skin has been reported in literature [30]. Since the myelin sheaths surrounding the nerves are rich in lipid content, it might be possible to achieve similar selective damage of the renal nerves using the same laser wavelength. Finally, fiber coupled lasers are available in high average powers (> 40 W) and depending on the treatment delivery (focused or

collimated), the total treatment time is likely to be less than both RF and ultrasound technique, thus, reducing patient discomfort and pain during the procedure.

In this article, we investigate the use of focused infrared lasers for renal denervation and the ability to cause thermal damage to the renal nerves, while saving the endothelium/part of the media. First, we identify three laser wavelengths at 980 nm, 1210 nm and 1700 nm for renal denervation based on the absorption spectra and penetration depth calculations A histochemistry comparison of the laser induced thermal damage performed at each of the three wavelengths show depths of damage in tissue extending to ~ 5 mm, ~4 mm and ~3 mm for 980 nm, 1210 nm and 1700 nm, respectively. Next, the *in vitro* laser renal denervation results are presented. Treatments are first performed using a collimated laser beam and show that laser penetration deep enough to cause denervation will also cause significant damage to the endothelium as well. In an effort to damage nerves without damaging the endothelium and without the use of an external cooling mechanism, we then perform the treatments using a focused light configuration at the three wavelengths. While all three wavelengths are capable of adventitial damage, only 980 nm and 1210 nm show evidence of penetrating deep enough to achieve renal denervation, while causing little to no damage to the endothelium. Next, *in vivo* renal denervation treatments in sheep are performed using a designed laser catheter prototype. Histochemistry results in sheep show clear evidence of laser renal denervation with depths of damage extending > ~1.5 mm from the lumen wall. Evidence of adventitial damage at depth of >~1mm from the lumen wall without injury to the endothelium and part of the media are also observed in some sections. Finally, the catheter design improvements, possible treatment parameters and selective damage issues are discussed before ending with our conclusions.

## 2. Materials and Methods

In this section, we begin with a discussion for the choice of 980 nm, 1210 nm and 1700 nm wavelengths for renal denervation based on the absorption spectra and penetration depth calculations. The laser treatments configurations in this article use a collimated laser or a focused laser setup, both of which are covered in this section. Finally, we describe the catheter design used for in-vivo laser treatment experiments in sheep and

provide details about the animal preparations for surgery, the interventional procedures, as well as the renal artery extraction procedure. The histochemistry protocol used for laser damage analysis is also outlined in this section.

### 2.1 Wavelength Selection and Penetration Depth Calculations

The primary requirement for the choice of wavelength is that it should be able to penetrate at least up to the depth in tissue to cause damage to the renal nerves , majority (>75%) of which are within ~1.5 mm from the lumen wall in humans [11]. In addition, it might be possible to cause selective damage to the nerves using specific laser wavelengths to target the nerves or nerve components with little damage to the no target tissues. For example, wavelengths with strong lipid absorption could potentially target the lipid rich myelin sheaths [31] that surround the nerves and cause injury with minimal collateral tissue damage. Although, not a critical issue for contact based renal treatments, it is also important to consider the absorption/scattering effects in blood for *in vivo* experiments, if there is blood in between the laser delivery and the lumen wall.

For our penetration depth calculations, we have used the Beer's law in anisotropic media, where the fluence $\phi(z)$ falls exponentially with depth as given by $\phi(z) = \phi_0 \exp(-\mu_{eff} z)$, where $\mu_a$ is the magnitude of the absorption coefficient, $\mu_s^{'}$ is the reduced scattering coefficient and $\mu_s^{'} = \mu_s(1-g)$, where $\mu_s$ is the scattering coefficient and g is the anisotropy coefficient. The reduced attenuation coefficient ( $\mu_{eff}$ ) and penetration depth ( $\delta$ ) are then calculated using the following formulas [32, 33]:

$$\mu_{eff} = \sqrt{3\mu_a(\mu_a + \mu_s(1-g))} \qquad if\ \mu_a << \mu_s;\ \mu_a < \mu_s^{'} \qquad (1)$$

$$\mu_{eff} = \mu_a + \mu_s(1-g) \qquad if\ \mu_a \geq \mu_s^{'} \qquad (2)$$

$$\delta = 1/\mu_{eff}$$

The penetration depth is defined as the distance at which the fluence is reduced to 1/e of the incident value and is equal to $1/\mu_{eff}$. We will first consider the penetration depth in tissue, followed by the penetration depth in blood. Since the tissue is mostly water, we assume for our calculations that the tissue absorption characteristics are similar to water. For the scattering calculations, we use the scattering coefficients in the dermis.

Fig. 3.1 shows the absorption spectra for water [34] and adipose [35] and the scattering coefficient in the human dermis (http://omlc.ogi.edu/news/jan98/skinoptics.html ; 1998). As seen in Fig. 3.1, wavelengths around ~1700 nm and ~1210 nm are attractive for targeting lipid rich structures such as the myelin sheaths surrounding the renal nerves and at the same time are near relative water absorption minima, allowing for good penetration depths. On the other hand, 980 nm is an attractive wavelength for deeper penetration depths, since it has the lowest water absorption of the three wavelengths, and is easily available in fiber coupled modules with high average powers of > 30W. Therefore, based on the penetration depths and potential for selective damage, the three wavelengths that we study for renal denervation in this paper are 980 nm, 1210 nm, and 1700 nm.

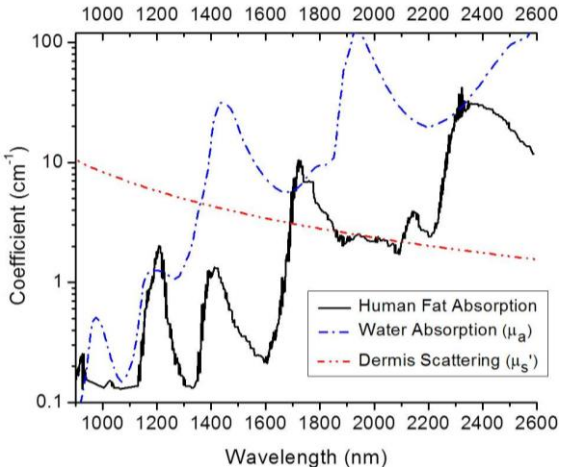


*Fig. 3.1. Infrared spectra showing the coefficients for water ($\mu_a$) and human fat absorption, effective scattering in the dermis ($\mu_s'$).*

Table 3.1 shows the calculated attenuation coefficients and the penetration depths in tissue at 980nm, 1210 nm and 1700 nm, respectively. The penetration depths in tissue are calculated using equations (1) and (2) to be ~2.7mm, ~1.9mm and ~1.1mm for 980nm, 1210nm and 1700nm respectively. While all three wavelengths have penetration depths of > 1 mm, only 980nm and 1210nm have the required penetration depth of > 1.5mm to damage majority of the renal nerves.

*Table 3.1. Penetration depth calculations in tissue for 980 nm, 1210 nm and 1700 nm.*

| **Wavelength (nm)** | $\mu_a$ **(cm$^{-1}$)** | $\mu_s'$ **(cm$^{-1}$)** | $\mu_{eff}$ **(cm$^{-1}$)** | $\delta$ **(mm)** |
|---|---|---|---|---|
| 980 | 0.5 | 8.5 | 3.7 | ~2.7 |
| 1210 | 1.3 | 5.8 | 5.3 | ~1.9 |
| 1700 | 6 | 3 | 9 | ~1.1 |

Table 3.2 shows the calculated attenuation coefficients and penetration depths in blood at the three wavelengths. The absorption and scattering coefficients are for blood (5% hematocrit concentration) [36]. In this case, the penetration depths are calculated using equations (1) and (2) to be ~2mm, ~2mm and ~1.1mm for 980nm, 1210nm and 1700nm respectively. Once again, both 980nm and 1210nm have higher penetration depths than 1700nm. Thus, both 980nm and 1210nm are attractive laser wavelengths for renal denervation with the necessary penetration depths to reach and damage the nerves.

*Table 3 2. Penetration depth calculations in blood (5% hematocrit concentration) for 980 nm, 1210 nm and 1700 nm*

| **Wavelength (nm)** | $\mu_a$ **(mm$^{-1}$)** | $\mu_s'$ **(mm$^{-1}$)** | $\mu_{eff}$ **(mm$^{-1}$)** | $\delta$ **(mm)** |
|---|---|---|---|---|
| 980 | 0.20 | 0.22 | 0.50 | ~2.0 |
| 1210 | 0.18 | 0.27 | 0.49 | ~2.0 |
| 1700 | 0.65 | 0.24 | 0.89 | ~1.1 |

Once again, the calculations presented here suggest that 980 nm and 1210 nm laser are capable of deeper penetration depths and are more suitable for renal denervation than 1700 nm. However, 1700nm is potentially capable of causing more selective damage to the renal nerves than 1210 nm due to the higher lipid absorption and is therefore, included in our *in vitro* studies.

### 2.2 Laser Sources Used for Treatments

A summary of the laser sources used in our studies is shown in Table 3.3 and Fig 3.2. The laser sources are all fiber based infrared lasers and are either commercially available fiber coupled laser diodes or fiber lasers designed and built by us. The 980 nm (IPG, MA,

USA) and 1210 nm (QPC, CA, USA) lasers are commercially available fiber coupled laser diodes. The 1700 nm laser used in our experiments is either a commercially available laser diode (QPC, CA) or a Raman fiber laser that we developed in lab [37]. The 980 nm laser diode fiber has a core/cladding diameter of 100/125 microns, 0.15 fiber NA and a maximum output power of ~30W. The 1210 nm laser diode fiber has a core/cladding diameter of 400/440 microns, 0.22 fiber NA and maximum output power of ~12W. The center wavelength is specified as 1211.76nm with a spectral width FWHM of 4.59 nm at full power. The 1700 nm laser diode also has a core/cladding diameter of 400/440 microns, 0.22 fiber NA and a maximum output power of ~7W. The center wavelength is specified as 1694nm with a spectral width FWHM of 12 nm at full power. The 1700 nm Raman fiber laser has a core cladding diameter of 10/125 microns, 0.13 fiber NA and a maximum output power of ~4 W. The center wavelength, in this case, is measured to be ~1708 nm with an FWHM of ~1 nm. Further details, including the setup and components of the 1700 nm laser are given in Chapter II.

*Table 3.3. Laser Sources used for the in vitro renal denervation study*

| Laser Source | Max Power(W) | Center Wavelength (nm) | FWHM at Full Power (nm) | Fiber Core/Cladding Diameter (mm) | Fiber NA |
|---|---|---|---|---|---|
| 980 nm | 30 | 976 | - | 105/100 | 0.22 |
| 1210 nm | 12 | 1211.76 | 4.59 | 400/440 | 0.22 |
| 1700 nm (diode) | 7 | 1694 | 12 | 400/440 | 0.22 |
| 1700 nm (Fiber) | 4 | 1708 | 1 | 10/100 | 0.13 |

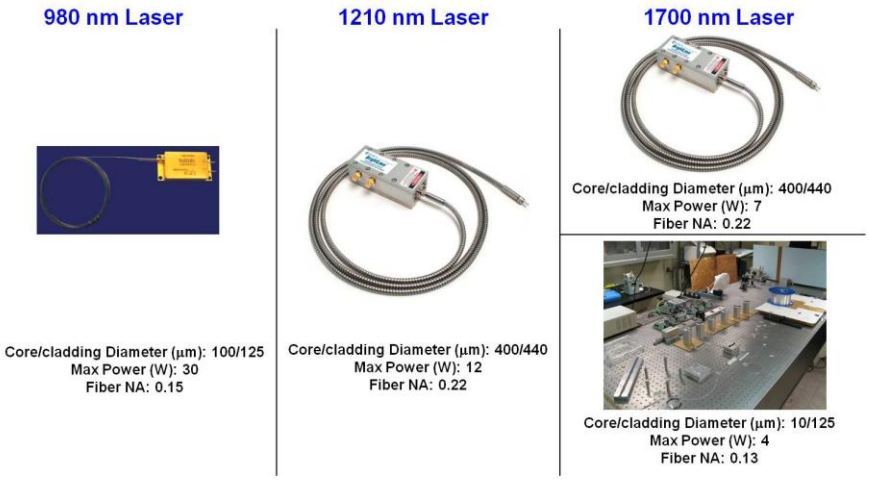


*Fig. 3.2. The laser sources used in the renal denervation study, 980 nm laser diode, 1210 nm laser diode, 1700 nm laser diode and our developed fiber laser source.*

## 2.3 Treatment Setup for in-vitro Wavelength Comparison Experiments

Figure 3.3 shows the setups used for the *in vitro* experiments. We perform our *in vitro* studies with both collimated (Fig. 3.3a) and focused (Fig. 3.3b) laser beams. Both setups use an aspheric lens and the $1/e^2$ beam diameter is calculated using a knife edge measurement. The sample is mounted on to the sample holder attached to a stepper motor stage and is scanned across the laser beam. The stepper motor has a minimum step size of 1 microns and the scan rate is controlled using a computer. Scanning is done in order to increase the area of laser treatment to maximize the chances of observing a laser affected region after performing the sectioning and histochemistry analysis.

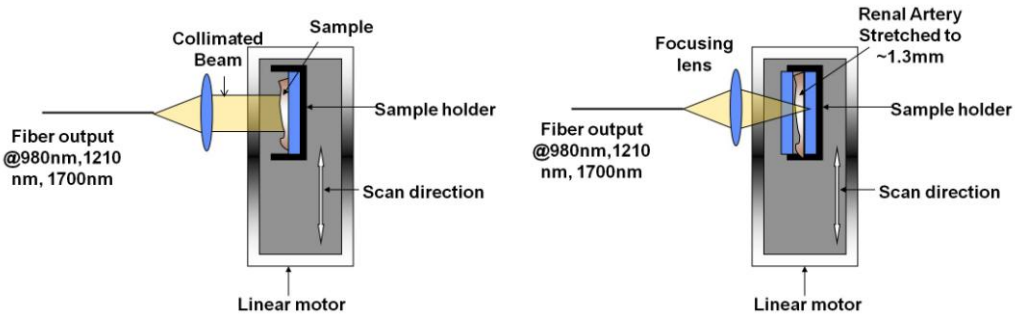


(a) (b)

*Fig. 3.3. Experimental setups used for the in vitro experimental studies. (a) Collimated laser beam setup and (b) Focused laser beam setup.*

The depths of damage at 980 nm, 1210 nm and 1700 nm in tissue are first studied using a homogenous tissue sample (chicken breast, in our case). The chicken breast was

obtained from a local grocery store. The samples are kept in a warm water bath at ~37 deg C for about an hour prior to the laser treatments using the collimated setup.

*In vitro* renal denervation experiments are performed using renal arteries obtained from cows/pigs/sheep. Since, majority (~75%) of the renal nerves in humans are within ~1-1.5mm from the artery wall, we mimic this *in vivo* dimension, where the effects of blood pressure thin the lumen wall thickness and bring the nerves closer to the wall, by stretching the *in vitro* renal artery samples so that distance for the tissue top (lumen wall) to bottom (around the nerves) is ~1.3 mm. This is done by compressing the tissue sample between two glass slides with a ~1.3 mm spacer in between. Thus, in all the *in vitro* renal denervation, the thickness of the sections from the lumen wall to the bottom of the section is ~ 1.3 mm during the laser treatments. The *in vitro* denervation histochemistry results have a true/actual scale length included for comparison between sections, but are not an accurate representation of the absolute length scale. *In vitro* renal denervation studies are performed first using the collimated setup and then using the focused laser setup

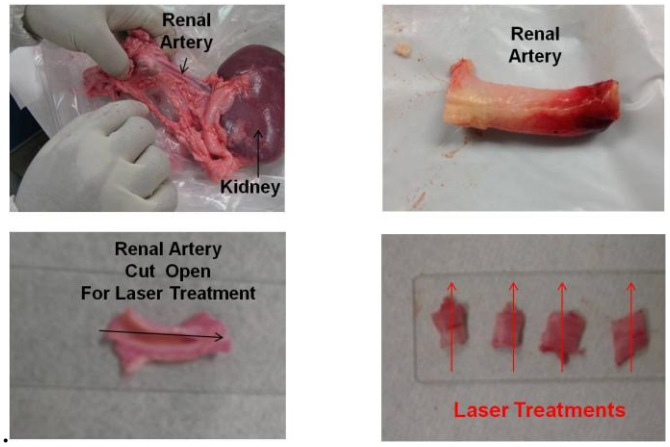


*Fig. 3.4. Extraction of the renal artery and sample preparation for the in vitro experiments. The renal artery is first identified and extracted. The artery is then sectioned (along dashed lines) and prepared for laser treatments.*

The entire kidney and arteries along with a piece of aorta are obtained from a local butcher shop, kept in Dulbecco's modified eagle medium (D-MEM), high glucose 1X (from GIBCO) and transported to the laser lab within hours of extraction, where they are stored in a refrigerator at 5-7 deg C, until the experiments are performed. The samples are kept in a warm water bath at ~37 deg C for about an hour prior to the laser treatments. All treatments are performed less than 48 hours after obtaining the samples. For the *in*

*vitro* experiments, the renal artery is cut into 3-4 sections and each section is then scanned across the laser with the beam incident on the lumen wall. Figure 3.4 shows an example, where the renal artery is extracted, sectioned and prepared for the in vitro laser treatments.

## 2.4 Catheter Design for *in vivo* Renal Denervation

The *in vivo* laser treatments are delivered to the renal artery using a catheter based approach. The catheter distal end design used for the *in vivo* experiments is shown in Fig. 3.5 and consist of five main components: glass ferrule to hold the fiber, air gap to adjust focal length, GRIN lens, right angle prism and an outer steel tube. In order to make the bend from the aorta to the renal artery and to fit inside the renal artery, the distal end has to be less than 1 cm in length and less than 2.2 mm outer diameter (OD). This was verified using a Tygon tube based artery model.

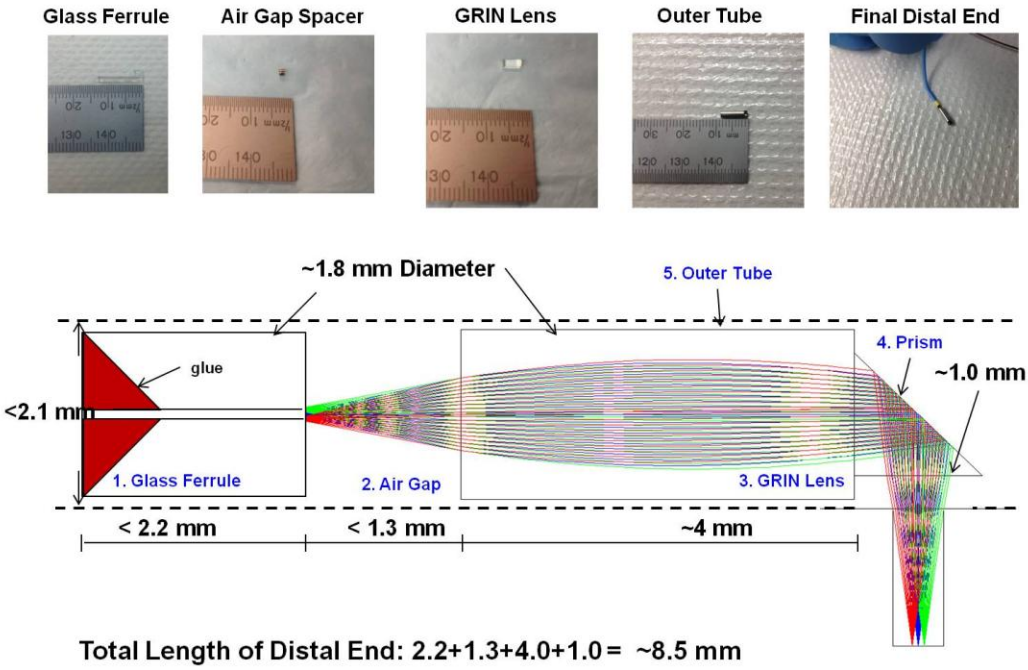


*Fig. 3.5. Distal end design for the catheter used to deliver the in vivo treatments.*

The first component is the glass ferrule to hold the optical fiber is place. The glass ferrule has an OD of ~1.8 mm and an inner diameter (ID) of ~0.129 mm to fit the 0.125 mm cladding fiber. The glass ferrules come in standard 13 mm lengths. They are polished down using a diamond grinder to a length of ~2.2 mm to fit within our required total

length specifications. Figure 3.5 shows an example of a standard fiber-glass ferrule and a finished product. The fiber is held in place inside the ferrule using UV cured optical adhesive (NOA 63).

The next component is the air gap spacer between the fiber and the GRIN Lens (Edmund Optics, #64532, NJ). The final focal distance between the outer steel tube and the focus is determined by the spacer by adjusting the distance between the fiber and the GRIN lens. The spacers are hypodermic steel tubes, which are precision machined down to specific lengths. The spacer tubes have an OD of ~1.65 mm and an ID of ~1.58 mm. We use GRIN lens as the focusing optic in this catheter design. The lens has an OD of ~1.8 mm and a length of ~4 mm. Figure 3.6a shows the ZEMAX simulation results for the range of focal lengths in tissue obtained using this GRIN lens at various air gap spacer lengths i.e. fiber-GRIN lens distances. Thus, the desired range of focal lengths is obtained by adjusting the spacer lengths between the fiber and the GRIN lens. Figure 3.6b also shows the corresponding ZEMAX beam diameters at the artery wall with the distal end in contact and at the focal spot. The refractive index in tissue is assumed to be ~1.38.

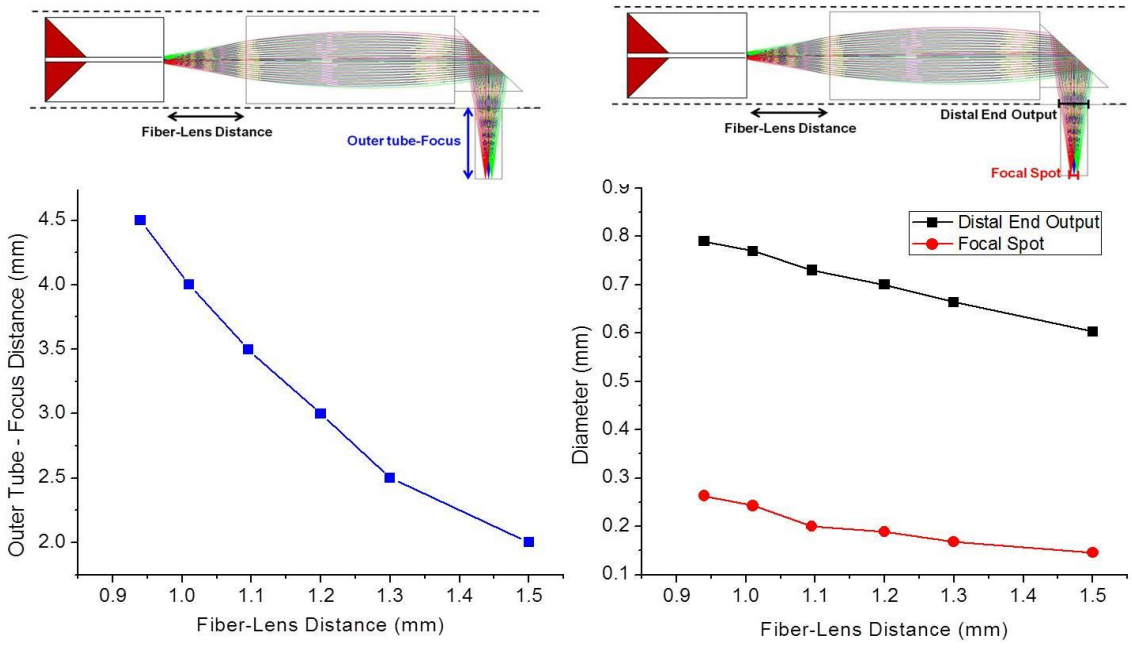


(A) (B)

*Fig. 3.6. ZEMAX Simulation results of the distal end performance in tissue (a) Outer tube – focus vs. the air gap length. (b) Estimate of the beam diameters at the distal end output and at the focus.*

The next component is the right angle prism (Tower Optical Corporation, FL) used to rotate the light by 90 degrees towards the renal artery wall. The prism is made of glass and the hypotenuse is aluminum coated to act like a mirror. The prism is glued on to the GRIN lens using UV cured optical adhesive (NOA 63).

The outer tube is the final component and holds all the optical components together. The hypodermic steel tube is ~8.5 mm long and has an ID of ~ 1.8 mm and an OD of less than 2.15 mm. The prism is protected by the outer tube and a 2 mm wide opening at the end of the tube allows the light from the prism to exit. Thus, the entire distal end is ~ 8.5 mm in length with an OD of less than 2.15 mm. In order to provide push ability to the distal end, the distal end and fiber is pushed though braided polyimide tubing, which is then glued to the metal outer tubing.

The finished catheter is then guided through a 5 French (F) FR4 catheter to help provide stronger push ability in combination with the polyimide tubing. Figure 3.7 shows a tygon tube model of the aorta (~1 cm diameter) and artery (~0.5 mm diameter) made to test and verify that the final catheter is able to fit within these dimensions. The fiber end is connectorized with an SMA connector to allow for a convenient connection with the laser. The entire finished catheter is then packaged and sterilized using ethylene oxide prior to the *in vivo* experiments.

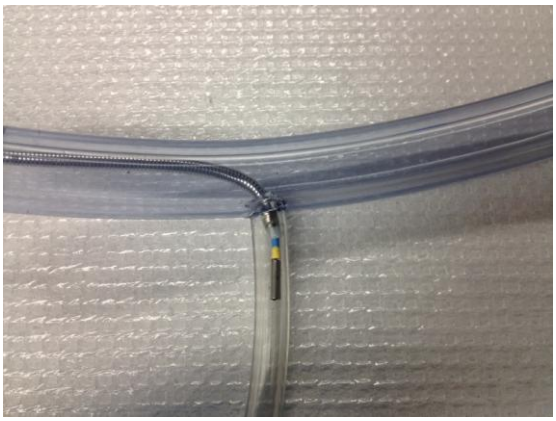

*Fig. 3.7. Tygon tube model used to test that the final catheter is able to make the bend and get to the renal artery. The aorta and renal artery diameters are assumed to be 1 cm and 0.5 mm respectively.*

The current catheter prototype does not have any maneuvering ability once inside the renal artery. We are not able to adjust the position such that the catheter is in the optimum position in the artery for the laser treatments. Since the treatments use a focused

laser beam in order to damage the nerves with minimum impact on the endothelium, it is important for the focus to be close to the location of the renal nerves, majority of which lie in 1-1.5mm region from the renal artery wall. One optimum condition for our treatment is for the distal end to make contact with the artery wall and then have the laser focus be ~2mm. Since, we are not able to control the distal end position once inside the artery; we use two catheter distal ends with two different focal lengths to improve our chances of at-least getting close to the optimum condition. For the *in vivo* experiments, the two focal lengths in tissue (outer tube to focus) for the two catheters are estimated to be ~2.8±0.3 mm and ~3.8±0.3mm, respectively. The average diameter of the renal artery in sheep/goat is ~5mm (range from ~4-6mm) and this choice of focal lengths should allow us to penetrate deep enough to achieve renal nerve damage and possibly save the endothelium as well. It is worth mentioning that we choose the two focal lengths to maximize our chances of getting close to the ideal conditions of focusing close to the nerves, but the best way to guarantee this is to use a specifically designed catheter delivery system that is able to control and maneuver the position of the distal end within the renal artery cross section. Catheter design improvements are further discussed in the discussion section. The focal length measurements are performed in air and estimated using an aperture. The focal length is tissue is then estimated as the focal length in air multiplied by the refractive index (~1.38) in tissue.

### 2.5 Animal Interventional Procedures

The animal use protocol was reviewed and approved by the University Committee for the Use and Care of Animals. We used 3 female adult sheep weighing 51-60 kg. The sheep were fasted for 24 hours prior to the procedure to aide in decreasing incidents of bloat, regurgitation, and increase visualization during fluoroscopy. Each sheep was given pre-op xylazine, 0.2mg/kg IM, to aide in calming the animal for restraint. A tourniquet was then placed behind the elbow, the hair clipped from the catheter site, and then cleaned with alcohol. An 18g angiocatheter was placed in the cephalic vein, secured in place, and flushed with heparinized saline. Propofol, 4-6 mg/kg IV, was then administered for anesthetic induction and to aide in endotracheal intubation. A 10-11 mm endotracheal tube was used for intubation and the tubes secured in place with a ⅝ TUBEGAUZ® tied

behind the ears. The animals were then placed on oxygen and isoflurane anesthesia using an adult unilimb breathing tube and 3-4 L rebreathing bag. Ophthalmic ointment was placed in the eyes. The analgesics buprenorphine 0.01 mg/kg intramuscular & carprofen 4 mg/kg subcutaneous were given to aide in alleviating postoperative pain & swelling. The antibiotic cefazolin 22 mg/kg IV was administered pre-operatively for prophylactic measures.

The wool was clipped & vacuumed from the femoral access site and EKG electrode sites.

The animals were then transferred to the operating suite and placed on a fluoroscopy table in ventro-dorsal position with the aid of a Hug-U-Vac positioner and leg ties. A Surgivet Advisor was utilized to monitor Non-invasive Blood pressure, EKG, pulse rate, oxygen saturation, respiratory rate, body temperature, and end tidal carbon dioxide. Reflexes were checked periodically. Lactated Ringers was given intravenously at 10 ml/kg/hour throughout the procedure. A rumen tube was placed & maintained during the procedure to aide in the prevention of bloat and regurgitation of rumen contents. The access site was surgically prepped with a minimum of 3 alternating scrubs of 2% chlorhexidine digluconate scrub (ChlorHex-Q SCRUB by Vedco, Inc.) and 70% isopropyl rubbing alcohol ,USP (MediChoice distributed by Owens & Minor) and a final prep of 2% chlorhexidine gluconate solution (Chlorhexidine by VetOne) was applied.

A 6 F sheath was inserted in the right femoral artery after application of lidocaine. A perclose device was used to pre-close the artery [38]. An 8 F 45 cm arrow sheath was then introduced through the arteriotomy. Heparin in the dose of 100 IU/kg was administered. Through the arrow sheath, a 5 French FR4 or an IMA catheter was used to engage the renal artery. A rosen wire was then advanced into the renal artery and the diagnostic catheter (FR4 or IMA) was advanced into the renal artery. Over the wire and the diagnostic catheter, the arrow sheath was advanced into the distal renal artery. The diagnostic catheter and the wire were removed and the laser catheter gently advanced out of the sheath and up to the renal artery bifurcation if possible. Treatment was provided for 5 seconds and the catheter and sheath was slowly withdrawn back in steps of approximately 5 mm and treatments provided until the catheter was in the aorta. Attempts were made to turn the catheter as it was withdrawn with the intent of providing treatment

along a spiral but this could not be reliably done. All three animals survived the procedure and were allowed to recover for ~24 hours post laser treatment.

The sheep were sedated with 0.3mg/kg intramuscular xylazine (Rompun, Bayer Animal Health) and humanely euthanized ~24 hours after the laser procedure with intravenous sodium pentobarbital at a dose of 1 ml/4.5 kg body weight (Beuthanasia, 390 mg/ml, Merck Animal Health). Sheep were placed in left lateral recumbency and the body wall was opened. Surrounding viscera was removed, exposing the kidneys and abdominal aorta. The abdominal aorta and vena cava were incised cranial and caudal to the branch points of the renal arteries and veins, allowing removal of the kidneys and their major vascular attachments en bloc. The renal arteries were finely dissected from the attachments at the abdominal aorta and the renal hilus. A thin layer of adventitial adipose tissue was retained with the renal arteries to avoid inadvertent damage of small adventitial blood vessels (vasa vasorum). The harvested renal arteries were placed in optimal cutting temperature compound (OCT$^{TM}$), frozen in liquid nitrogen and stored at -80 deg C until frozen sections could be cut. Total time from euthanasia to renal artery placement in media was approximately 20-30 minutes. Cryostat-cut sections were made and mounted on glass slides, and stored at -80 deg C until used for histochemical staining of dehydrogenase activity. To identify laser damage in the processed sections, we use the methylthiazolyldiphenyl-tetrazolium bromide (MTT) histochemical assay, a proxy for dehydrogenase enzyme activity for cell viability. [37] Cells that are alive when frozen maintain dehydrogenase activity, but cells that are dead do not have this activity. In live cells that are frozen, dehydrogenase activity reduces the slightly yellow water soluble MTT substrate into a water insoluble dark blue to black precipitate. Thus, in the MTT histochemical assay, live cells stain dark blue while dead cells remain clear. The volume of incubation medium was adjusted proportionally depending on the number of sections to be stained. The sections were immersed in MTT incubation medium under aerobic conditions with no ambient light for about 30 minutes, rinsed in DI water and dried afterwards. The sections were examined using a microscope (WILD Makroscop M420) and photos were taken using a digital camera (NIKON Coolpix 5000).

# 3. Experimental Results

The results section is organized as follows. We first study the depths of damage at 980 nm, 1210 nm and 1700 nm in a homogenous tissue sample to verify that these wavelengths can cause thermal damage deep enough to reach the nerves. Histochemical analysis shows that the depths of damage decreases as the wavelength increases. Next, we present the laser renal denervation results beginning with the *in vitro* renal denervation studies using both the collimated laser beam and focused beam setups at the three wavelengths. Histochemical analysis shows that renal nerve damage is achieved in both setups, whereas the endothelium and part of the media are seen to be saved only in the focused treatment setup. It is also seen that 980 nm and 1210 nm may be more optimal for renal denervation. Finally, we present the results for *in vivo* renal denervation experiments in sheep using the designed laser catheter discussed in section 2.4. The histochemical analysis shows clear evidence of laser induced thermal damage to the renal nerves at depths of > ~1.5 mm from the lumen wall using a focused 980 nm laser.

## 3.1 Wavelength Versus Damage Depths in Tissue

The laser induced thermal damage depths in tissue at 980 nm, 1210 nm and 1700 nm are first studied by treating a homogenous tissue sample (chicken breast) with the three lasers under similar conditions. In each case, the laser beam diameter ($1/e^2$) is ~3mm and the sample is scanned across the beam at 1mm/s. Figure 3.8 shows an example of the histochemistry in a section of chicken breast tissue treated with the highest possible power level at each of the three wavelengths. At the highest power levels used, we observe tissue damage up to depths of ~5 mm, ~4 mm and ~3 mm for the 980 nm, 1210 nm and the 1700 nm laser, respectively. Regions of the tissue that appear clear/white and not stained indicate thermal damage. Extreme tissue damage is observed only for 1700nm shown in Fig. 3.8c, where the laser caused the tissue water content to possibly boil and rupture the tissue. Figure 3.9 shows the average (over three samples) and standard deviation of the measured depths of damage versus power level at each of the three wavelengths. It is observed that after a certain power level, the tissue becomes “opaque” and the depth of damage remains fairly constant with further increase in power.

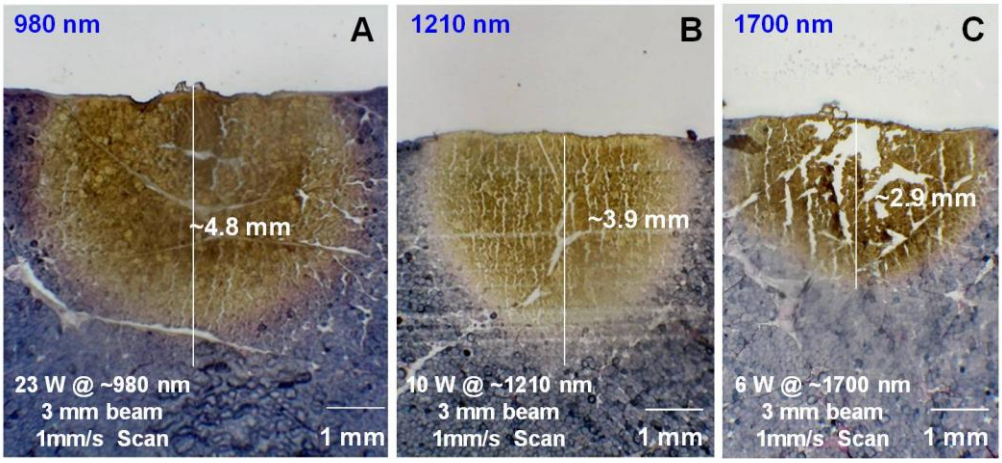


*Fig. 3.8. In vitro wavelength comparison study at (a) 980 nm( 23W) (b) 1210 nm (10 W) and (c) 1700 nm(6 W). The samples are all scanned across a 3mm diameter beam at 1 mm/s. Extreme tissue damage was observed in (c) using the 1700 nm laser.*

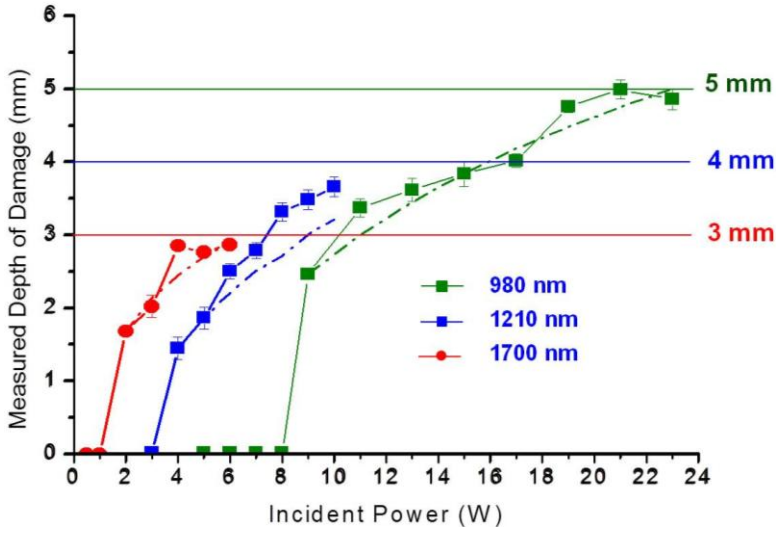


*Fig. 3.9. Measured depth of damage in chicken breast tissue treated with 980 nm, 1210 nm and 1700nm .The depths are measured from the histochemistry results. Dashed lines are estimated depth of damage using Beer's law and the reduced attenuation coefficients from Table 3.1.*

The depth of tissue damage follows the same trend for penetration depths calculated in section 2.1, with the depths decreasing with increasing wavelength. Table 3.4 compares the relationship between the penetration depths, the expected depth of damage from Beer's law and the measured depths of damage at highest power level for each of the three wavelengths. In order to calculate the expected depth of damage, we use the Beer's law and the attenuation coefficients from table 3 1. The earliest incident power level showing histological evidence of thermal damage in tissue is taken as the tissue damage threshold power. For eg, at 980 nm, we first observe damage at an incident

power of`~9 W corresponding to a peak incident intensity of 255 W/cm$^2$ ,with the damage zone extending to a depth of ~2.5 mm in the tissue. The peak intensity at 2.5 mm is then estimated from Beer's law to be ~102 W/cm$^2$ and is taken as the intensity threshold for tissue damage at higher incident powers. At the highest power level of 23 W, the depth at which the incident intensity drops down to this threshold value is calculated to be ~ 5mm and is close to the measured depth of ~4.8 mm from the histology results. The Beer's law model is neither the simplest nor the most complicated published laser damage model and may offer a useful compromise between accuracy and complexity of calculation [39] . The model used here assumes that the Beer's law is valid through the entire laser treatment duration and that the absorption of the incident laser power by the tissue does not decrease as the tissue becomes thermally denatured. Other factors not included in this simplified model are post laser thermal diffusion effects and thermal effects at intensities less than the calculated threshold intensities at each wavelength. As can be seen in table 3 4, the expected depths and the average measured depths of damage are fairly close. The difference between the expected and measured values is slightly higher for 1210 and 980 nm since the scattering effects are higher than absorption at these wavelengths compared to 1700m, where the Beer's law is expected to be more accurate. The slight difference between expected and measured values could also be due to the fact that we used absorption and scattering characteristics for water and dermis respectively, instead of the chicken breast tissue. However, the data presented here indicates that the model and effective attenuation coefficients used for calculating the penetration depth provides a fairly good estimation for laser induced damage depths in tissue for our purposes.

*Table 3.4. Comparison of trends between the penetration depth calculations and the measured depth of damage from the histochemistry results*

| **Wavelength** | **Penetration Depth (mm)** | **Expected Depth of Damage in Tissue at Highest Power (mm)** | **Average Measured Depth of Damage in Tissue at Highest Power (mm)** |
|---|---|---|---|
| 980nm | 2.7 | 5 | 4.8 |
| 1210nm | 1.9 | 3.2 | 3.7 |
| 1700nm | 1.1 | 2.9 | 2.9 |

From the data presented in Fig. 3.9 and Table 3 4, we can see that all three wavelengths are capable of causing damage >1.5mm required for renal denervation. However, unlike the 1700 nm laser, both 980 nm and 1210 nm lasers are capable of damaging tissue at depths > 3 mm without causing extreme tissue damage. Therefore, the 980 nm and 1210 nm laser wavelengths appear to be better candidates for laser renal denervation based on the tissue depths of damage achieved.

### 3.2 Laser Renal Denervation with a Collimated Laser Beam

After verifying that the three wavelengths are capable of damaging homogenous tissue at depths of > 2mm, we performed a damage depth study in the renal artery to verify that lasers can penetrate deep enough to damage the renal nerves. The 1700nm laser is used for the collimated beam laser denervation experiments. The damage depth study in the previous section showed that 1700 nm has the least damage depth. Therefore, if we are able to attain renal denervation at 1700nm, it should be possible to achieve renal denervation at 980nm and 1210nm due to the higher penetration depths at these wavelengths.

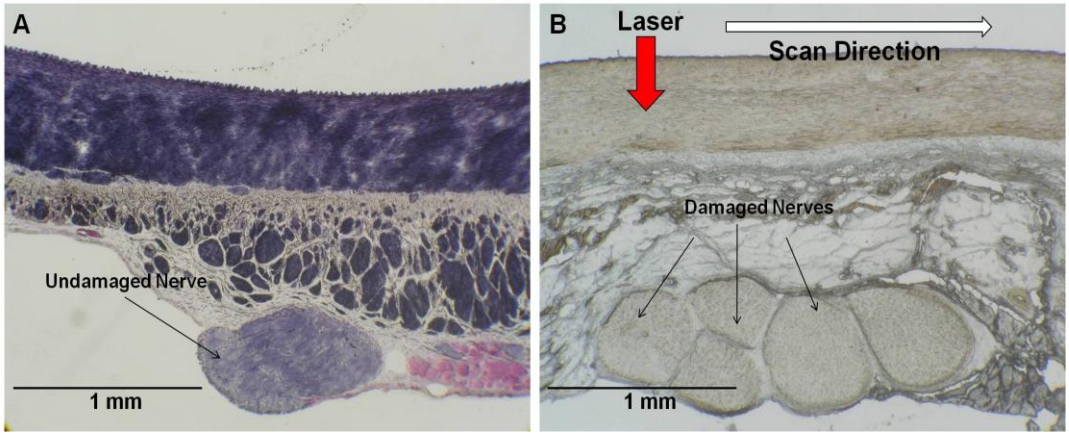


*Fig. 3.10. In vitro laser renal denervation in bovine renal artery (a) Untreated control section (b) Artery cross section treated with collimated 1700 nm laser (1.5W, 2mm beam,0.4mm/s scan) showing damaged nerves and artery tissue.*

Figure 3.10 shows an example of histochemistry of an untreated bovine renal artery section and a bovine renal artery section treated with the collimated laser setup at 1700 nm (1.5W, 2mm beam diameter, 0.4mm/s scan speed). The entire section in Fig. 3.10b is not stained (whitish region) and indicate thermal damage. As we can see from Fig. 3.10b for the treated case, the entire tissue section including the renal nerves are not

stained showing clear evidence of transmural thermal damage. Thus, the results presented in Fig. 3.10 using a collimated laser beam show that laser treatments can effectively damage the renal artery section including the renal nerves and demonstrate that without any external cooling mechanism or focusing of the laser beam, causing sufficient thermal damage to the renal nerves would also significantly damage the endothelium as well as the media above the renal nerves.

### 3.3 Laser Renal Denervation with a Focused Laser Beam

In contrast to collimated laser treatments, focusing the laser beam at a depth close to the renal nerves should allow for an intensity difference and hence, a temperature difference between the tissue top, close to the endothelium and the tissue bottom, where the nerves are located. Thus, a focused laser beam treatment should be able to cause thermal damage to the renal nerves, while sparing injury to the endothelium and part of the media. This is a significant advantage of laser based treatments. Compared to other energy sources, the laser output from a fiber can be easily focused to small beam spots using optical components like lenses and mirrors.

The focused laser in-vitro renal denervation studies are done in porcine renal arteries using the focused laser setup (0.4 mm/s scan speed) at 980 nm, 1210 nm and 1700 nm. For each wavelength, the renal arteries are exposed to a range of incident power levels, causing little or no damage to the artery section to causing complete damage to the entire section. In each case, the artery tissue is stretched during laser treatments so that the top to bottom thickness is ~1.3mm, and the beam diameters on the artery wall (tissue top) and adventitia (tissue bottom) are estimated to be ~1.2 mm and ~0.4 mm respectively.

Figure 3.11 shows the MTT histochemistry results for porcine renal artery cross sections treated with the three wavelengths over a range of incident power levels. For each wavelength, the first column shows an example where the treatment power is inadequate to reach the nerves, the middle column shows an example of the optimum condition, where we are able to observe nerve damage with little to no injury to the endothelium and finally, the last column shows an example, where the power level is high enough to cause transmural damage to the entire section from top to bottom at the

treatment site. For example, Fig. 3.11(a, b and c) show the histochemistry for treatments with the 980 nm laser. No damage is observed at ~1.5 W. At ~1.8 W, we see clear evidence of nerve damage with little to no damage to the endothelium. As the power is further increased to ~3 W, the entire depth of the tissue section is damaged at the treatment site. Thus, the optimum treatment power level for the 980 nm laser in this setup is ~ 1.8W. Similarly, Fig. 3.11 (e and h) show the optimum condition in this setup for 1210 nm and 1700 nm, respectively, where there is evidence of thermal injury to the nerve without any apparent damage to the endothelium.

For the focused denervation experiments, Beer's law and the focus advantage are countering effects, i.e. if the absorption is high, then most of the light will be absorbed close to the lumen and will not be able to penetrate deep enough to reach the nerves and makes the focusing advantage less useful. This can be further understood using a simple 1D Gaussian beam model that takes into account both the effects of focusing and absorption (Beer's law). The laser intensity distribution with tissue depth is given by:

$$I(r,z) = I_{peak} e^{(-2r^2/w^2(z))} e^{(-\mu_{eff} z)}$$

*where*

$$I_{peak}(z) = 2\frac{P_{inc}}{\pi w^2(z)}$$

$P_{inc}$ is the incident power on the tissue surface, w(z) is the beam waist radius. For a converging laser beam of radius R0 at the tissue surface, focused at a depth z=FD with a beam radius of RD at the focal spot, the beam waist (w(z)) with depth can be estimated by the following expression:

$$w(z) = R0\left(\begin{array}{ll} \frac{(RD-R0)z}{R0\times FD}+1 & if\ 0 \le z \le FD \\ \frac{(R0-RD)z}{R0\times FD} - \frac{(R0-2RD)}{R0} & if \quad z > FD \end{array}\right)$$

For the *in vitro* experiments shown in Fig. 3.11, The values for R0 and RD are ~0.6mm and ~0.2 mm, respectively. In the absence of absorption, one would then expect a peak intensity difference along the beam center (r=0) of ~9x between the endothelium and the renal nerves. Figure 3.12 shows the modeled intensity difference between artery surface and the nerve location for the optimum treatment conditions in Fig. 3.11, taking into account the effect of absorption as well as focusing. As seen in Fig. 3.12, once the effects

of absorption are taken into account, the intensity difference factor drops to ~5x for 980 nm, ~4x for 1210 nm and ~3x for 1700 nm. Therefore, Beer's law and focusing advantage are seen to be countering effects and a lower absorption is expected to be better for focusing applications at greater depths. Since 980 nm has the lowest effective attenuation, we can then expect to achieve the greatest intensity difference between the endothelium and the nerves at this wavelength.

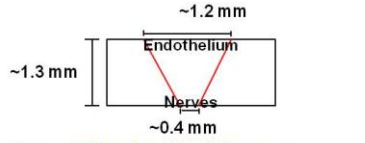


Expect 9X intensity difference between endothelium and nerves

| Wavelength (nm) | Modeled Intensity Difference Factor |
|---|---|
| 980 | ~5 X |
| 1210 | ~4 X |
| 1700 | ~3 X |

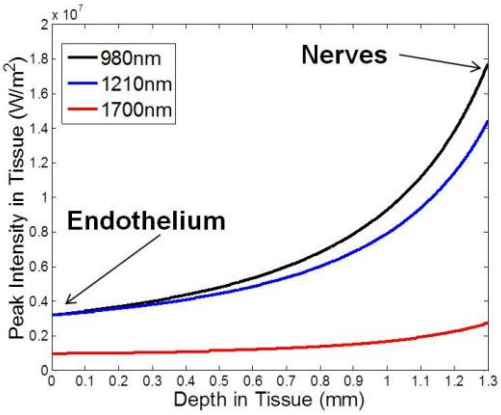


*Fig. 3.12. The beer's law and focusing advantage are seen to be countering effects. Without absorption, one would expect an intensity difference factor of ~ 9x between the endothelium and the nerves at the three wavelengths. Once absorption is taken into account, the calculated intensity difference factor drops to ~ 5x, 4x and 3 x for 980 nm, 1210 1nm and 1700 nm, respectively.*

Both 980 nm and 1210 nm have higher penetration depths (lower water absorption) compared to 1700 nm. The results in Fig. 3.11, show that both 980nm and 1210nm lasers are capable of causing significant nerve damage, with little to no injury to the endothelium and part of the media. On the other hand, the 1700 nm laser (higher water absorption) is only capable of causing partial nerve damage, while saving the endothelium. Thus, as expected from Fig. 3.12, the advantage of focusing the light is seen to be higher by using a wavelength with lower water absorption and higher tissue penetration. The results shown in Fig. 3.11 also do not show any clear evidence of selective nerve damage for laser treatments at 1210 nm and 1700 nm, wavelengths corresponding to the lipid absorption lines. Selectivity issues are further explored in the discussion section. Thus, from the results presented in this section, 980 nm laser appears to be the best candidate for renal denervation experiments due to the higher penetration depth and the ability to cause nerve damage with little to no endothelial injury. The *in vitro* results also suggest that for the 980 nm laser, after taking into account the effect of

focusing and absorption, an intensity difference factor of ~5x between the endothelium and nerve location should be able to achieve renal nerve damage with little to no injury to the endothelium. As an added advantage, 980nm lasers are also commercially available in fiber coupled diode modules with average powers of > 30 W.

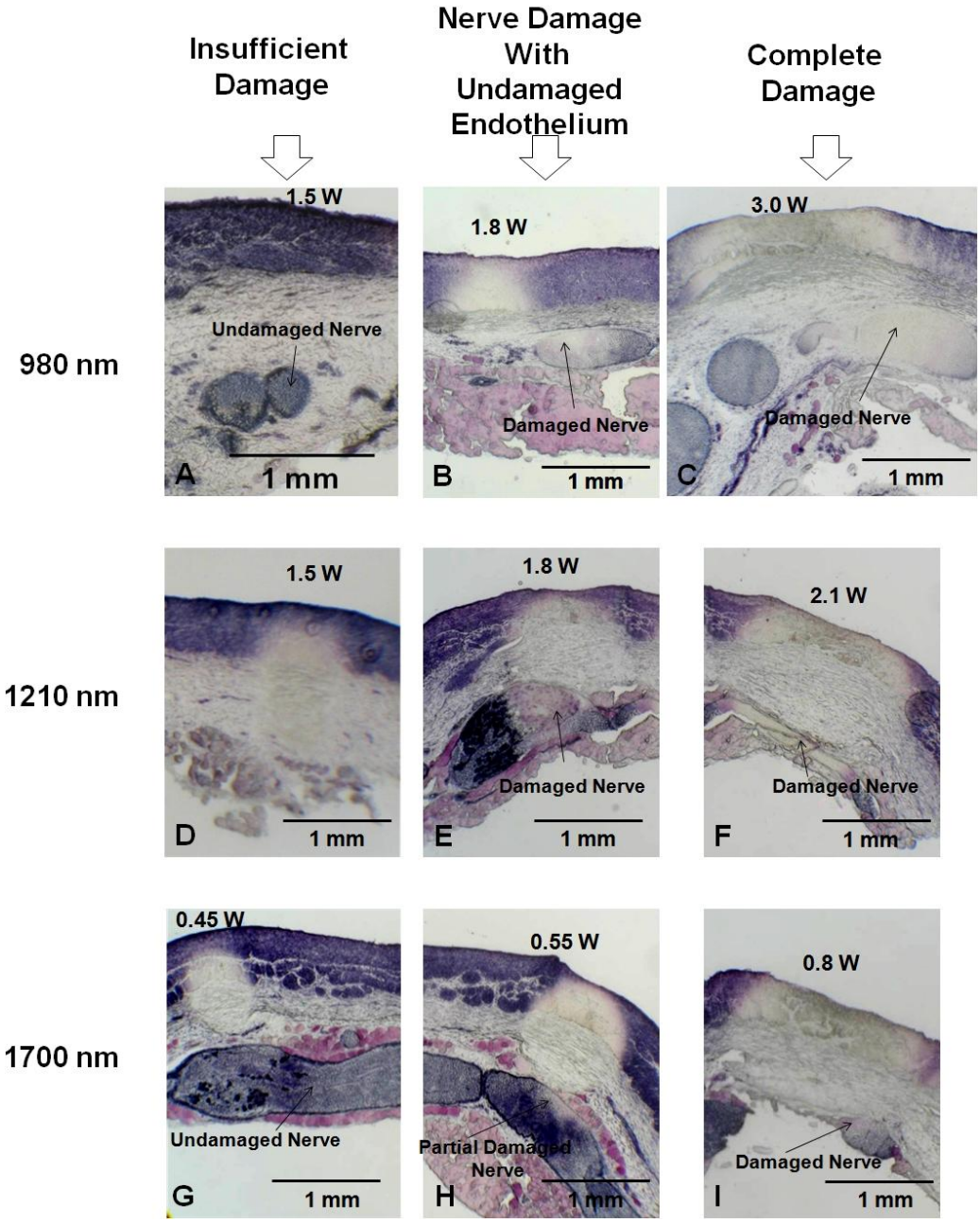


*Fig. 3.11. In vitro porcine renal denervation results using the focused laser setup at 980 nm(a,b,c), 1210 nm(d,e,f) and 1700nm (g,h,i), scanned at 0.4mm/s. Three cases are shown for each wavelength The first column shows inadequate damage. The middle column shows the optimum treatment condition achieved for each wavelength with thermal damage to the nerves and little to no damage to the endothelium. The third column shows treatment power levels high enough to cause transmural damage extending across the entire section.*

Adult sheep are used as the animal model for our *in vivo* trials, since the aorta and artery diameters in sheep are closer in dimension to humans. Renal studies have also been reported in literature using the sheep as the animal model [40]. Since the *in vitro* results in Fig. 3.11 are performed in porcine arteries, we also performed *in vitro* experiments in sheep as well, using the 980 nm laser to verify that we can achieve similar results as in Fig. 3.11. Figure 3.13 shows the renal denervation results in sheep using the 980nm laser treated with 2W and 3W respectively, scanned at 0.4 mm/s across the beam. In each case, the tissue is stretched during laser treatments so that the top to bottom thickness is ~1.3mm, and the beam diameters on the artery wall (tissue top) and adventitia (tissue bottom) are estimated to be ~1.2 mm and ~0.4 mm respectively. Fig. 3.13a shows an example, where the MTT histochemistry results shows evidence of nerve damage, while the endothelium and part of the media are still stained and indicate no laser damage. Fig. 3.13b shows an example, where the treatment power is high enough to cause transmural damage across the entire section including the nerves as well as the endothelium. The MTT histochemistry results in Fig. 3.13 are consistent with *in vitro* porcine renal denervation results using the 980 nm laser shown in Fig. 3.11. Thus, the histochemistry results presented in this section clearly demonstrate that a focused laser setup can achieve renal denervation by thermal damaging the renal nerves without causing injury to the endothelium and part of the media.

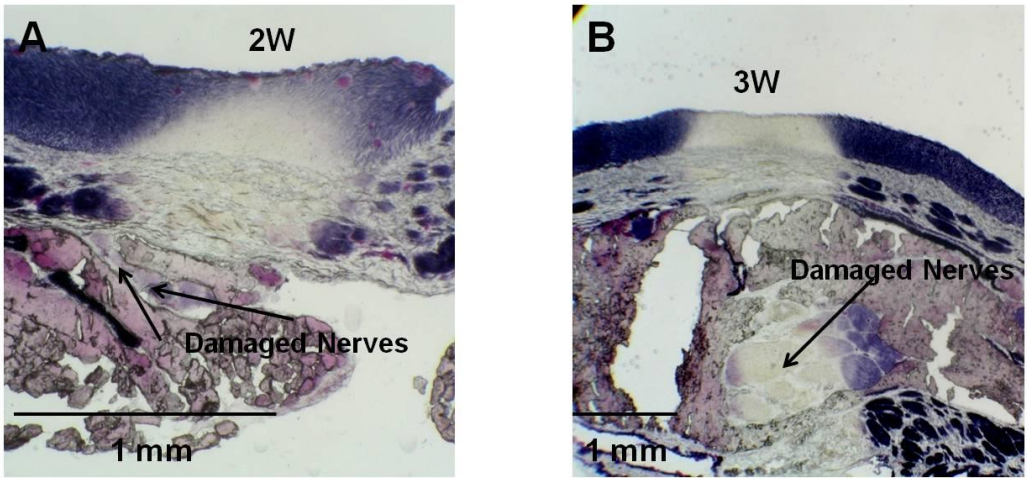


*Fig. 3.13. In vitro renal denervation in sheep using the 980nm laser scanned at 0.4mm/s (a) Histochemistry of treatment with 2 W showing damaged nerve with no apparent injury to the endothelium (b) Histochemistry of treatment with 3 W showing transmural damage to the nerve and arterial tissue across the entire depth.*

### 3.4 *In vivo* Renal Denervation in Sheep using a Focused 980nm Laser

After verifying that the focused 980 nm laser setup is capable of damaging renal nerves without injuring the endothelium, we attempt to obtain similar results *in vivo* in sheep using a catheter based treatment approach. The catheter design used for our *in vivo* trials is described in section 2.4. Two catheters with estimated focal lengths of ~2.8±0.3mm (FL1) and ~3.8±0.3mm (FL2) in tissue are used for the *in vivo* renal denervation experiments. The laser treatment powers range from 2.0-4.0 W with a treatment time of 5seconds at each treatment spot. The treatments are first administered in the renal artery section proximal to the kidney and then move progressively to the distal end closer to the aorta. The position of the catheter distal end is observed using fluoroscopy. The fluoroscope images of the laser catheter in the renal artery prior to the laser treatments are shown in Fig. 3.14.

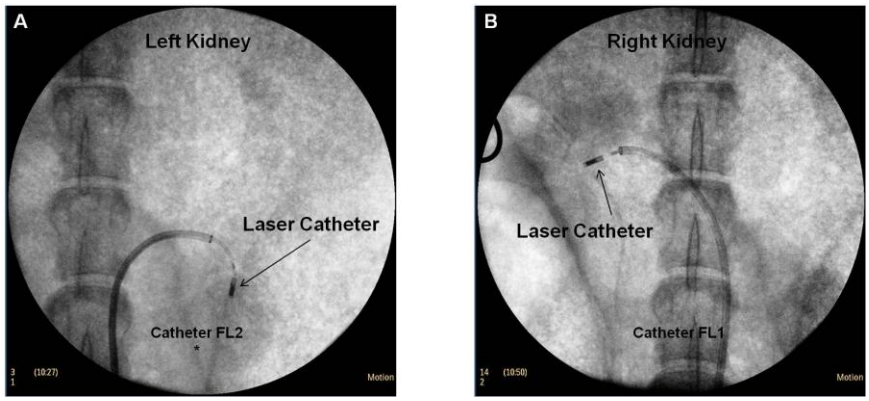


*Fig. 3.14. Fluoroscope image of laser catheters in sheep in vivo (a) Left kidney (b) Right kidney.*

Figure 3.15 shows the MTT histochemistry of *in vivo* ovine renal artery sections treated with the 980 nm laser for 5 seconds, using FL1 at 3.5-4.0 W (A and B), and FL2 at 2.5-3W (C and D). In Fig 3.15 (A and B) we see a distinct large nerve around the renal artery that is clearly damaged, as evidenced by the lack of staining. The depth of damage in this section is seen to extend > ~1.1 mm from the lumen wall. Fig. 3.15(C and D) shows another example, where the renal nerves in the treatment site are not stained and indicate thermal damage by the 980 nm laser. The depth of damage in this section is seen to extend > ~1.5 mm from the artery wall. The results presented in Fig. 3.15 clearly indicate that the 980nm penetrates deep enough (> ~ 1.5 mm) to cause thermal damage to the renal nerves and that it is possible to achieve renal denervation using this technique.

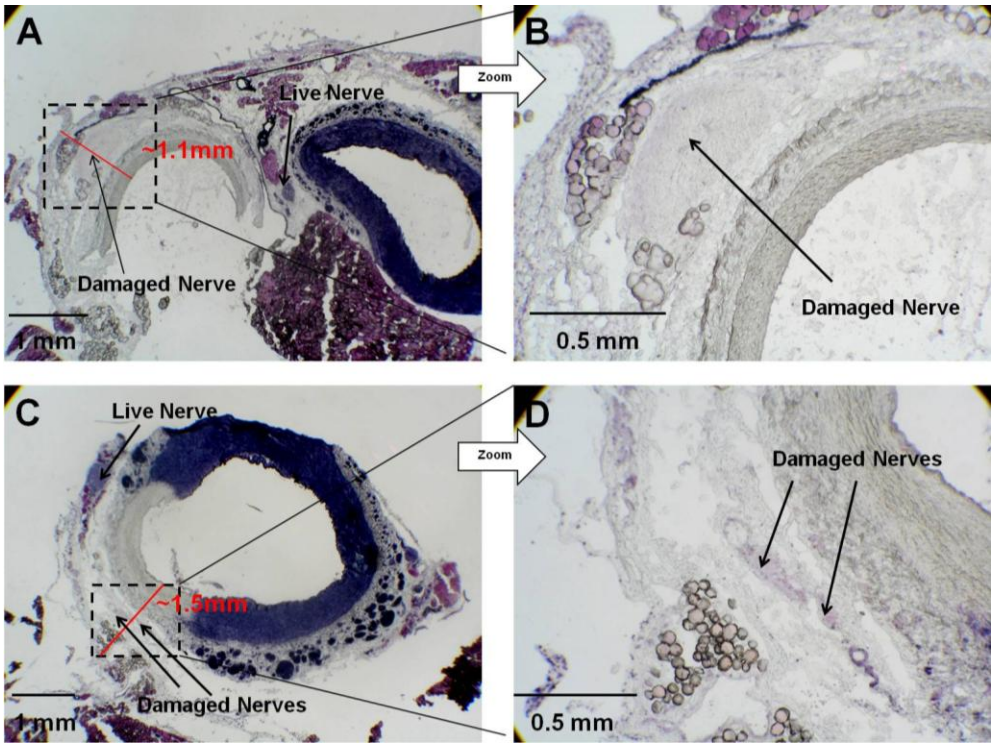


*Fig. 3.15. MTT histochemistry of sections from in vivo trials showing complete renal denervation with 980 nm laser at the treatment site using catheters FL1 (a and b) and FL2 ( c and d).*

While both examples in Fig. 3.15 show evidence of laser renal denervation using the 980 nm, the endothelium is also unstained as well, and indicates thermal injury. The laser treatments are delivered in a focused beam with a Gaussian profile. Therefore, the intensity is highest at the beam center and towards the focus and decreases as we move away from the focal spot. Since our results presented in Fig. 3.15 show the endothelium to be damaged as well, the beam intensity delivered must be higher than the damage threshold for the endothelium and media. One reason could be that the focal point is closer to the artery wall instead of the nerves, or that there is a lack of sufficient laser intensity difference between the artery wall and nerve site. To better understand the damage to the endothelium, we look at histochemistry of sections surrounding the artery sections with clear nerve damage. Figure 3.16 (A and B) show the histochemistry for sections surrounding those with nerve damage, shown in Fig. 3.15 (A and C), respectively. As expected, we see a decrease in the depth of damage as we move through the sections from top to bottom indicating that we are moving away from the focal spot and the incident intensity on the artery wall is decreasing. We do not see any sections in

this sequence with evidence of damage in the media or adventitia, without injuring the endothelium, which suggests that the minimum beam intensity delivered to the artery wall, has most likely already exceeded the threshold for damage.

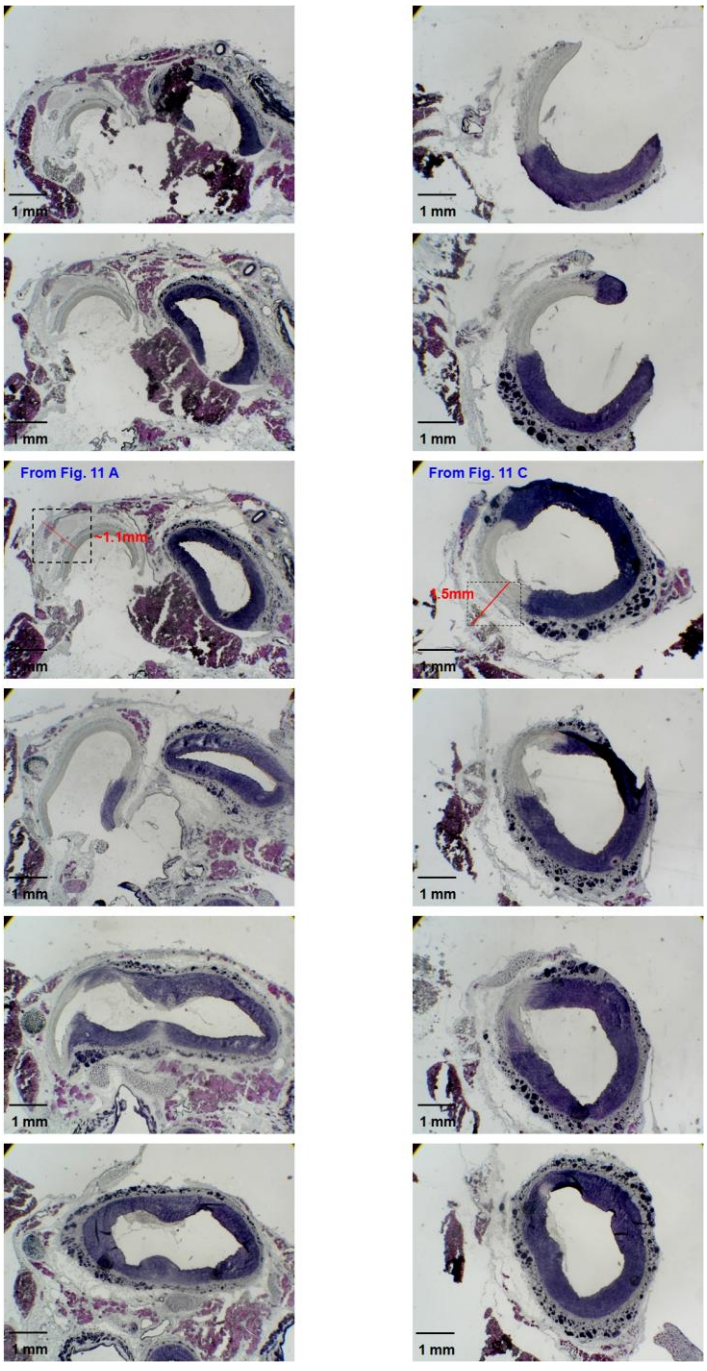


(a) (b)

*Fig. 3.16. Histochemistry sequence of sections surrounding the sections from Fig. 3.15, which show renal nerve damage after treated with . (a) catheter FL1 and (b) catheter FL2.*

For the distal end design (presented in section 3.2.4) in our *in vivo* trials, we used two focal lengths of ~2.8 and ~3.8mm, since the position of the distal end within the renal artery is not controllable. With an average artery diameter of ~5mm, the focal lengths were chosen to ensure that the focal spot was at some depth beyond the artery wall. The *in vitro* data presented in section 3.3 suggest that an intensity difference of at least ~5x between the endothelium and the nerve locations (accounting for the focusing and absorption effects) might be able to cause damage to the renal nerves at ~1.5 mm without injuring the artery wall. For the two designed distal ends and using the beam diameters from Fig. 3.6, we calculate the intensity difference factor for the two distal ends at various positions within the renal artery, which corresponds to the varying depths of focus beyond the artery wall. Fig. 3.17 shows the endothelium to focus intensity difference factor for the two catheters. We can see that for catheter FL1, the difference factor is > ~5x for a small range of distal end positions within< ~0.3mm from the artery wall. For catheter FL2, the difference factor is always less than 5x.This suggests that the catheter FL1 distal end should be quite close to the artery wall during the laser treatment to achieve nerve damage without damaging the endothelium. For catheter FL2, the difference factor is always less than 5x, suggesting that there may not be sufficient intensity difference to damage the nerves while saving the endothelium. It is worth mentioning that even with the ideal position of the distal end placement, the laser treatment parameters must be optimized to achieve denervation, while saving the endothelium. This is also clearly seen in Fig.3.11, where we see the varying levels of artery tissue damage for the same optical configuration as the laser power is increased.

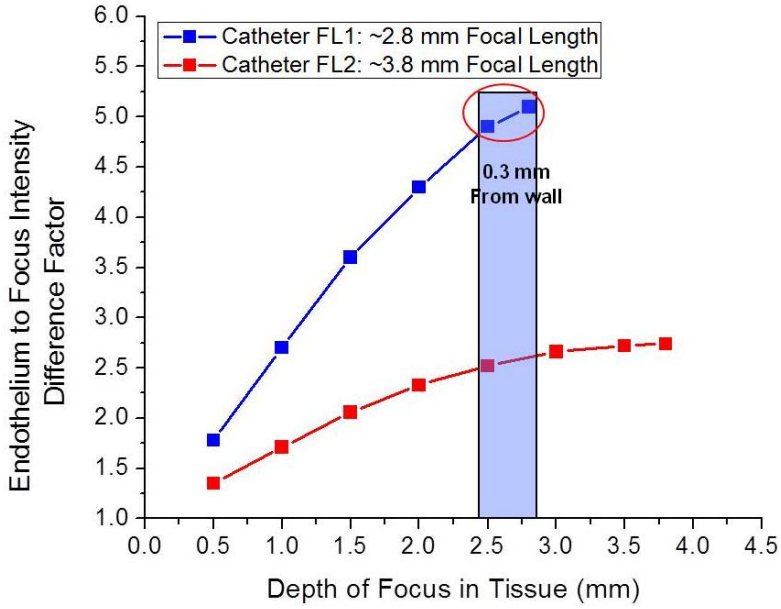


*Fig. 3.17. Catheter FL1 and FL2 intensity difference factor between the endothelium and the focus for various focus positions within the tissue. Both absorption and the focusing effect are taken into account.*

One of the advantages of focusing the laser beam, as we saw in our *in vitro* results, is the ability to achieve renal nerve damage with little to no injury to the endothelium. In our *in vivo* experiments, we were able to see some histological evidence of thermal damage in the media and adventitia without any damage to the endothelium. Figure 3.18 shows histochemistry examples of ovine renal artery cross sections, where the media/adventitia is damaged, but the endothelium remains undamaged. However, in these cases, there are no clearly identifiable renal nerves or the depth of damage does not extend deep enough to damage the renal nerves. Some possible reasons for the depth of damage not extending deep enough could be that the laser treatment powers or exposure times may not be sufficient and/or the focal spot may not be near the nerves, but closer to the media. While we have not observed *in vivo* histochemistry results showing clear nerve damage without injuring the endothelium, we have shown that it is possible to achieve renal denervation *in vivo* (Fig. 3.15) and the results presented in Fig. 3.18 suggest that the focused laser treatment can cause arterial damage at depths > ~1mm without causing any damage to the renal artery wall including the endothelium and part of the media. Some of the possible ways to potentially achieve renal denervation without damaging the non-target tissues in the renal artery including the endothelium are further discussed in the next section.

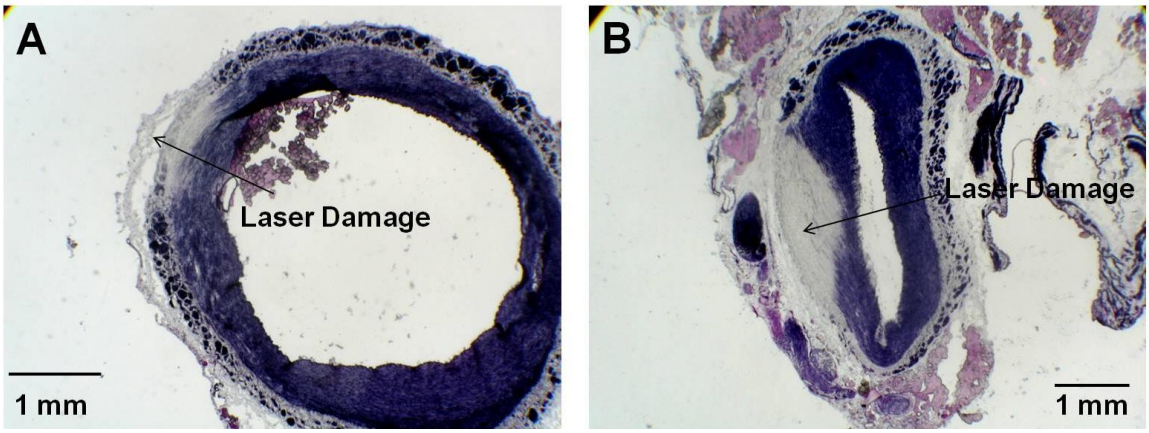


*Fig. 3.18. MTT histochemistry examples showing damage to the media/adventitia with little to no injury to the endothelium and artery wall. (A) catheter FL1 3.5-4W,5 seconds (B) catheter FL1, 2-2.5W, 5 seconds.*

## 4. Discussion

Renal denervation as recently become of great interest as a treatment for resistant hypertension. The current treatment modalities use either RF or ultrasound therapy. Both of these techniques either cause endothelial damage and local thrombus formation, or employ an external cooling mechanism to minimize the artery wall damage. In addition, their current energy delivery times are greater than 4 minutes. There is an interest in exploring other energy forms for renal denervation that could substantially reduce the treatment times as well as minimize the damage to the endothelium and other non-target arterial tissue. In this study, we investigate the use of lasers as an alternative energy source for renal denervation. Lasers have three potential advantages over current techniques. First, unlike RF and ultrasound with very high penetration depths (>1 cm), the laser penetration depth can be adjusted by using the right wavelength, such that the depth of damage extends only as deep as that required to reach the renal nerves and ensures that the abdominal, pelvic or lower extremity nerves are unaffected. The histological results in section 3.1 show tissue damage depths of ~5mm, ~4mm and ~3 mm for 980 nm, 1210 nm and 1700 nm respectively. Second, lasers can be easily focused, which helps to create an intensity gradient across the artery section and allow saving the endothelium and artery wall without using any external cooling mechanism. The *in vitro* results using both 980 nm and 1210 nm lasers presented in section 3.3 show clear evidence of renal denervation with little to no injury to the endothelium. Finally, the *in vivo* histochemistry results using the 980 nm laser presented in section 3.4 shows that it

is possible to achieve renal denervation using lasers. In this case, our treatment time at each spot is only 5 seconds. With an estimated total of 4-6 treatment spots in each artery, the total energy delivery time could be less than 1 minute for the denervation treatments, helping to minimize patient discomfort and pain.

The *in vivo* results presented in section 3.5 clearly show histological evidence of renal denervation using the 980 nm laser. However, the endothelium and artery wall is also injured in the current process. One of the major limitations in our animal trials is the current catheter capabilities. The catheter prototype used in the *in vivo* trials presented in this chapter does not have any maneuvering ability, once inside the renal artery. Thus, it is not possible for us to reliably keep the distal end in one position and turn it such that it is at a known distance from the vessel wall. In our treatments, the same catheter depending on where it is located within the cross section of the vessel, could be focused at the adventitia at one point and in the lumen at the other. A slight turn could move the focus elsewhere and the slight position change may result from change in catheter position, respiratory movements of the kidney or even the pulsality of blood flow. The catheter movement could also result in inadequate exposure times and/or the overlap of treatment sites leading to insufficient damage or excessive damage at the treatment site. For example, the histochemistry results in Fig. 3.16a seem to suggest a possible treatment spot overlap or distal end movement during treatment as evidenced by an almost circumferential damage profile. In addition, the actual power levels delivered to the artery wall are also dependent on the amount of blood between the distal end and the artery wall. Catheter maneuverability inside the renal artery plays a crucial role for renal denervation treatments, including current treatments that use RF and ultrasound therapy. In these treatment modalities, the position of the catheter distal end is critical to obtain the desired results, since the power, exposure times and the required penetration are highly dependent on the distance between the energy source and the artery wall.

One possible solution to fix the position of our laser catheter inside the renal artery is to use a technique similar to the RF treatments (http://www.medtronicrdn.com/intl/healthcare-professionals/symplicity-rdn-system/index.htm ), where the laser distal end would be kept in contact with the renal artery wall prior to the laser treatments. The distal end contact with the artery wall can be

monitored using the impedance measurements currently used in RF treatments. It might also be possible to ensure wall contact by monitoring the back reflection of laser light from the catheter. As the distal end gets closer to the artery wall, the light reflected back into the distal end from the artery wall will increase as well, which could be used to identify the position of the distal end within the artery. Once the position of the distal end within the renal artery is fixed, the next step is to optimize the focal length. The *in vitro* data presented in section 3.3 suggest that an intensity difference of ~5x between the endothelium and the nerve locations, taking into account the effects of absorption and focusing, should be able to damage renal nerves at ~1.5 mm without injuring the artery wall. In order to achieve the highest intensity difference between the endothelium and the nerves, it would be ideal to use a focusing optic with the highest numerical aperture for a given focal length. Majority of the renal nerves are at a depth of < 2mm from the artery wall [11]. With the available GRIN lens and the beam diameters calculated in Fig. 3.6, a focal length closer to ~2 mm is more optimal to damage renal nerves, while saving the endothelium. This is shown in Fig. 3.19, where we see that the intensity difference factor for a 2 mm focal length distal end remains > ~5x for focus positions at depths between ~1-2 mm in tissue, which should be sufficient to damage majority of the renal nerves, while saving the endothelium. Figure 3.19 also suggests that the distal end can be within ~1mm from the artery wall and should still be able to damage the renal nerves with minimal injury to the endothelium. Further modeling taking into account the heat transfer terms could be used to identify the optimum treatment parameters to cause renal nerve damage with minimal damage to the non-target artery tissue.

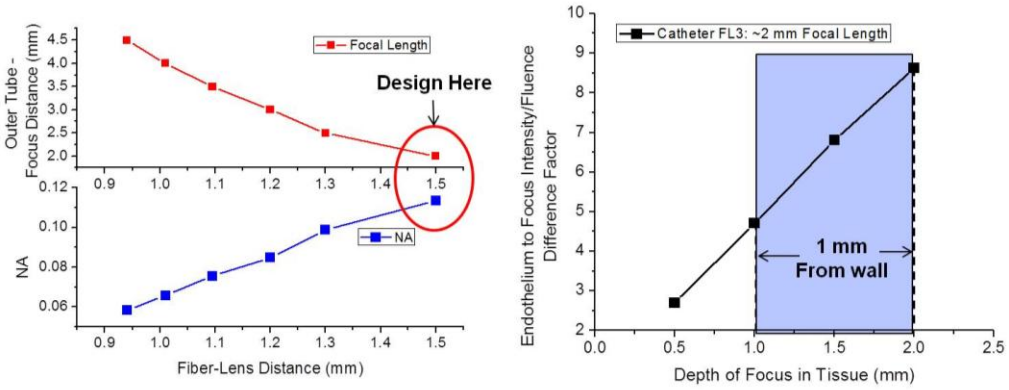


*Fig. 3.19. Catheter distal end design with a focal length of ~ 2mm. The intensity difference factor is calculated to be > 5x for focus positions at depths > 1 mm and suggests that it should be possible to*

*damage nerves without injuring the endothelium as long as the distal end is within ~ 1mm from the artery wall.*

Another potential solution is to have the distal end enclosed in water or saline cooled balloon. This would allow the laser to be at a fixed distance from the artery wall (either centered or close to the artery wall), while cooling the artery wall during treatments. An example of external cooling is demonstrated in chapter II, where we use an external cooling mechanism and perform laser treatments in human skin to damage sebaceous glands at depths of ~1.65 mm from the epithelium, while saving the top >0.5mm of the skin tissue from laser damage. Therefore, the combined effect of cooling and focusing has a high potential to minimize endothelial and most non-target tissue damage as well.

An advantage of using lasers is the potential for causing selective tissue damage. Since the myelin sheaths surrounding the nerves are rich in lipid content, it might be possible to selectively target the myelin sheaths to damage the renal nerves. As shown in Fig. 3.1, both ~1700 nm and ~1210 nm are close to strong lipid absorption lines. However, the ratio of the absorption coefficient for water and lipids is still small at these wavelengths. Our preliminary *in vitro* work in renal arteries comparing these wavelengths, show that without external cooling, ~1700 nm may not have the necessary damage depth to reach the renal nerves at ~1.5 mm without causing endothelial damage as well. We also did not observe any significant selective advantage of using the 1210 nm over the 980 nm laser treatments. Increased selectivity at 1210 nm and at 1700 nm (with external cooling) might be achievable by using altered pulse durations. For example, Anderson et al claim selective damage to sebaceous glands in human skin with external cooling using a pulsed 1720 nm laser. However, the optimal pulse duration ($\tau$) for selective photothermolysis is dependent on the target tissue structure and size ($\tau \cong d^2 / 27\kappa$ )[41], where $\kappa$ is the thermal diffusivity constant [41]. The nerve size and distribution varies significantly, from < ~100 μm to > ~1 mm[21] and assuming a $\kappa$ of $1.3\times10^{-3}$ $cm^2/s$ similar to [41, 42] , this corresponds to pulse durations from ~3 ms to 300 ms across the cross section of the renal artery. Thus, the significant variations in nerve dimension across the cross section of renal arteries might make selective denervation

more challenging. Our *in vitro* experiments for renal denervation also suggest that wavelengths with lower tissue absorption are more advantageous to leverage the focusing advantage to achieve denervation without damaging the endothelium. From this perspective, 1064 nm lasers are possibly an even better candidate for renal denervation due to the lower water absorption. However, higher energy delivery would be required to cause sufficient thermal alteration of the renal nerves.

Since the exact position and distribution of the nerves within the renal artery during treatments are unknown, current denervation techniques use an algorithm to deliver treatments in a circumferential manner to ensure that the nerves are damaged. The laser treatments can be delivered circumferentially using a rotating mirror or mirror designs, where the incident light is split into a circumferential beam [43] , which can then be used to damage the renal nerves. Another advantage of using lasers is that it might be possible to image and detect the position of the nerve prior to the treatments. Catheter based OCT techniques are currently in existence and have been developed for arterial imaging, with penetration depths of ~2-3 mm[44]. It remains unclear whether it is preferable to tailor the ablation to the proximal renal artery, where there are fewer larger nerve trunks or to the distal vessel, where there are more and smaller nerves. With a proximal strategy, missing a large nerve could compromise the therapeutic efficacy. On the other hand, a distal strategy would require treatment of a larger number of nerve targets to achieve complete denervation. The current RF technique uses a combination of proximal and distal ablation techniques [11]. Identifying the renal nerves using an imaging technique like OCT, before laser treatments could help to reduce the number to treatment spots, damage a larger percentage of nerves and possibly avoid unnecessary damage to the artery.

## 5. Summary

In this chapter, we demonstrate a novel technique for renal denervation using focused infrared fiber lasers. Renal denervation using a focused laser configuration can be used to damage the adventitial layer while saving the endothelium and part of the media. Both *in vitro* and *in vivo* data are presented and the histochemistry results clearly show evidence of renal nerve damage. Three laser wavelengths a ~980nm, ~1210 nm and ~1700 nm are

investigated based on the absorption spectra and penetration depth calculations. The focusing advantage and Beer's law are seen to be countering effects and a wavelength, such as 980nm and 1210 nm with lower absorption in tissue is seen to be more advantageous for renal denervation than 1700 nm. While all three wavelengths are capable of damaging renal nerves, only 980 nm and 1210 nm lasers show histology evidence of penetrating deep enough to cause nerve damage, while also saving the endothelium. The histochemistry results of *in vivo* renal denervation in sheep using a designed laser catheter prototype show clear evidence of renal denervation with depths of damage extending > ~ 1.5 mm from the artery wall. We also see some sections, where there appears to be laser induced damage to the media/ adventitia at depths of > ~1 mm without injury to the endothelium. However, in these cases there are no visible nerves at the treatment site or the depth of damage does not extent deep enough to cause renal denervation. The catheter capabilities are currently the limiting factor in our trials. We discuss some of the possible treatment parameters and catheter designs to minimize damage to the endothelium and non-target tissues. In this study, we show that focused infrared lasers are a viable technique for causing renal denervation with minimum damage to the endothelium/media and warrants further research to refine the treatment parameters and evaluate its efficacy as a potential treatment for resistant hypertension.

## References


1. D. Lloyd-Jones, R. Adams, M. Carnethon, G. D. Simone, T. B. Ferguson, K. Flegal, E. Ford, K. Furie, A. Go, K. Greenlund, N. Haase, S. Hailpern, M. Ho, V. Howard, B. Kissela, S. Kittner, D. Lackland, L. Lisabeth, A. Marelli, M. McDermott, J. Meigs, D. Mozaffarian, G. Nichol, C. O'Donnell, V. Roger, W. Rosamond, R. Sacco, P. Sorlie, R. Stafford, J. Steinberger, T. Thom, S. Wasserthiel-Smoller, N. Wong, J. Wylie-Rosett, and Y. Hong, "Heart disease and stroke statistics—2009 update: a report from the American heart association statistics committee and stroke statistics subcommittee," Circulation **119**, 480-486 (2009).
2. P. Kearney, M. Whelton, K. Reynolds, P. Muntner, P. Whelton, and J. He, "Global burden of hypertension: analysis of worldwide data," Lancet **365**, 217-223 (2005).
3. W. H. O. (WHO), "Global health risks: mortality and burden of disease attributable to selected major risks," (2009).
4. V. Roger, A. Go, D. Lloyd-Jones, R. Adams, J. Berry, T. Brown, M. Carnethon, S. Dai, G. d. Simone, E. Ford, C. Fox, H. Fullerton, C. Gillespie, K. Greenlund, S. Hailpern, J. Heit, P. Ho, V. Howard, B. Kissela, S. Kittner, D. Lackland, J. Lichtman, L. Lisabeth, D. Makuc, G. Marcus, A. Marelli, D. Matchar, M. McDermott, J. Meigs, C. Moy, D. Mozaffarian, M. Mussolino, G. Nichol, N. Paynter, W. Rosamond, P. Sorlie, R. Stafford, T. Turan, M. Turner, N. Wong, and J. Wylie-Rosett, "Heart disease and stroke statistics—2011 update: a report from the American Heart Association.," Circulation **123**, e18-e209 (2011).
5. G. Thomas, M. H. Shishehbor, E. L. Bravo, and J. V. Nally, "Renal denervation to treat resistant hypertension: Guarded optimism," Cleve Clin J Med **79**, 501-510 (2012).
6. S. Erdine, "Compliance with the treatment of hypertension: the potential of combination therapy," J Clin Hypertens **12**, 40-46 (2010).
7. I. Fergus, "Antihypertensive pharmacotherapy: adverse effects of medications promote nonadherence.," J Cardiometab Syndr **4**, E1-E3 (2009).
8. H. Krum, M. Schlaich, R. Whitbourn, P. A. Sobotka, J. Sadowski, K. Bartus, B. Kapelak, A. Walton, H. Sievert, S. Thambar, W. T. Abraham, and M. Esler, "Catheter-based renal sympathetic denervation for resistant hypertension: a multicentre safety and proof-of-principle cohort study," Lancet **373**, 1275-1281 (2009).
9. D. A. Calhoun, D. Jones, S. Textor, D. C. Goff, T. P. Murphy, R. D. Toto, A. White, W. C. Cushman, W. White, D. Sica, K. Ferdinand, T. D. Giles, B. Falkner, and R. M. Carey, "Resistant hypertension: diagnosis, evaluation, and treatment: a scientifi c statement from the American Heart Association Professional Education Committee of the Council for High Blood Pressure Research.," Circulation **117**, e510-526 (2008).
10. M. P. Schlaich, H. Krum, P. A. Sobotka, and M. D. Esler, "Renal Denervation and Hypertension," Am J Hypertens **24**, 635-642 (2011).
11. D. S. Atherton, N. L. Deep, and F. O. Mendelsohn, "Micro-Anatomy of the Renal Sympathetic Nervous System: A Human Postmortem Histologic Study," Clin. Anat. **25**, 628-633 (2012).

12. V. Campese, S. Ye, H. Zhong, V. Yanamadala, Z. Ye, and J. Chiu, "Reactive oxygen species stimulate central and peripheral sympathetic nervous system activity," Am J Physiol Heart Circ Physiol **287**(2004).
13. R. Katholi, "Renal nerves in the pathogenesis of hypertension in experimental animals and humans," Am J Physiol **245**(1983).
14. M. D. Esler, H. Krum, P. A. Sobotka, M. P. Schlaich, R. E. Schmieder, and M. Böhm, "Renal sympathetic denervation in patients with treatment-resistant hypertension (The Symplicity HTN-2 Trial): a randomised controlled trial," Lancet **376**, 1903-1909 (2010).
15. H. Krum, "Catheter-based renal sympathetic denervation for resistant hypertension: durability of blood pressure reduction out to 24 months. ," Hypertension **57**, 911-917 (2011).
16. H. Krum, M. Schlaich, P. Sobotka, M. Esler, F. Mahfoud, M. Böhm, M. Dunlap, K. Rocha-Singh, and R. Katholi, "TCT-12 Long-term Follow-up of Catheter-based Renal Denervation For Resistant Hypertension Confirms Durable Blood Pressure Reduction," J Am Coll Cardiol. **60**(2012).
17. S. Worthley, C. Tsioufis, M. Worthley, A. Sinhal, D. Chew, I. Meredith, Y. Malaiapan, and V. Papademetriou, "TCT-213 Safety And Efficacy Of A Novel Multi-Electrode Renal Denervation Catheter In Resistant Hypertension: 3 Month Data From The EnligHTN I Trial," J Am Coll Cardiol **60**(2012).
18. M. P. Schlaich, B. Bartus, D. Hering, F. Mahfoud, M. Böhm, E. A. Lambert, H. Krum, G. W. Lambert, and M. D. Esler, "311 Feasibility of Catheter-Based Renal Denervation and Effects on Sympathetic Nerve Activity and Blood Pressure in Patients With End-Stage Renal Disease," J Hypertension **30**, e91-e92 (2012).
19. S. C. Bertog, P. A. Sobotka, and H. Sievert, "Renal Denervation for Hypertension," J. Am. Coll. Cardiol. Intv. **5**, 249-258 (2012).
20. T. Mabin, M. Sapoval, V. Cabane, J. Stemmett, and M. Iyer, "First experience with endovascular ultrasound renal denervation for the treatment of resistant hypertension," Eurointervention **8**, 57-61 (2012).
21. Y. Sinelnikov, S. McClain, Y. Zou, D. Smith, and R. Warnking, "Renal denervation by intravascular ultrasound: Preliminary in vivo study," AIP. Conf. Proc **1481**, 337-344 (2012).
22. K. Steigerwald, A. Titova, C. Malle, E. Kennerknecht, C. Jilek, J. r. Hausleiter, J. r. M. N. hrig, K.-L. Laugwitz, and M. JONER, "Morphological assessment of renal arteries after radiofrequency catheter-based sympathetic denervation in a porcinemodel," J. Hypertens **30**, 2230-2239 (2012).
23. S. Butenas, T. Orfeo, and K. G. Mann, "Tissue Factor in Coagulation Which? Where? When?," Arterioscler Thromb Vasc Biol **29**, 1989-1996 (2009).
24. V. W. M. v. Hinsbergh, "Endothelium—role in regulation of coagulation and inflammation," Semin Immunopathol **34**, 93-106 (2011).
25. A. Breitenstein, F. C. Tanner, and T. F. Lüscher, "Tissue Factor and Cardiovascular Disease: Quo Vadis?," Circ J **74**, 3-12 (2010).
26. Q. Peng, A. Juzeniene, J. Chen, L. O. Svaasand, TrondWarloe, K.-E. Giercksky, and J. Moan, "Lasers in medicine," Rep. Prog. Phys. **71**, 056701 (2008).
27. V. Y. Reddy, P. Neuzil, A. d'Avila, M. Laragy, Z. J. Malchano, S. Kralovec, S. J. Kim, and J. N. Ruskin, "Balloon catheter ablation to treat paroxysmal atrial

fibrillation: What is the level of pulmonary venous isolation?," Heart Rhythm **5**, 353-360.
28. P. Liu, S. Ren, Y. Yang, J. Liu, Z. Ye, and F. Lin, "Intravenous Catheter-Guided Laser Ablation: A Novel Alternative for Branch Varicose Veins," Int Surg **96**, 331-336 (2011).
29. E. P. Gerstenfeld, "Have lasers finally found their niche in interventional cardiology?," Heart **98**, 525-527 (2012).
30. F. H. Sakamoto, A. G. Doukas, W. A. Farinelli, Z. Tannous, M. Shinn, S. Benson, G. P. Williams, J. F. Gubeli, H. F. Dylla, and M. R. Rox Anderson, "Selective Photothermolysis to Target Sebaceous Glands:Theoretical Estimation of Parameters and Preliminary Results Using a Free Electron Laser," Las Surg Med **44**, 175-183 (2012).
31. P. Morell and R. H. Quarles, "Characteristic Composition of Myelin," in *Basic Neurochemistry: Molecular, Cellular and Medical Aspects.,* 6 ed., G. Siegel, B. Agranoff, and R. Albers, eds. (Lippincott-Raven, Philadelphia, 1999).
32. D. J. Maitland, J. T. W. Jr, and J. B. Prystowsky, "Optical properties of human gallbladder tissue and bile," App Opt **32**, 586-591 (1993).
33. S. J. Jacques, "Laser-Tissue Interactions," in *The Surgical Clinics of North America*, W. H. Schwesinger and J. G. Hunter, eds. (W. B. Saunders Company, 1992), pp. 531-558.
34. K. Palmer and D. Williams, "Optical properties of water in the near infrared.," J Opt Soc Am **64**, 1107-1110 (1974).
35. R. Anderson, W. Farinelli, H. Laubach, D. Manstein, A. Yaroslavsky, J. Gubeli, K. Jordan, G. Neil, M. Shinn, W. Chandler, G. Williams, S. Benson, D. Douglas, and H. Dylla, "Selective photothermolysis of lipid-rich tissues," Lasers Surg Med **38**, 913-919 (2006).
36. A. Roggan, M. Friebel, K. D. rschel, A. Hahn, and G. M. ller, "OPTICAL PROPERTIES OF CIRCULATING HUMAN BLOOD IN THE WAVELENGTH RANGE 400–2500 NM," J Biomed Opt **4**, 36-46 (1999).
37. V. V. Alexander, K. Ke, Z. Xu, M. N. Islam, M. J. Freeman, B. Pitt, M. J. Welsh, and J. S. Orringer, "Photothermolysis of Sebaceous Glands in Human Skin Ex Vivo with a 1,708 nm Raman Fiber Laser and Contact Cooling," Lasers Surg Med **43**(2011).
38. D. L. Bhatt, R. E. Raymond, T. Feldman, and G. A. Braden, "Successful "pre-closure" of 7Fr and 8Fr femoral arteriotomies with a 6Fr suture-based device (the Multicenter Interventional Closer Registry) " Am J Cardiol **89**, 777-779 (2002).
39. J. T. Walsh.Jr, T. J. Flotte, R. R. Anderson, and T. F. Deutsch, "Pulsed C02 Laser Tissue Ablation: Effect of Tissue Type and Pulse Duration on Thermal Damage," Lasers Surg Med **8**, 108-118 (1988).
40. J. A. Whitworth, D. A. Denton, W. F. Graham, T. J. Humphery, B. A. Scoggins, and J. P. Coghlan, "THE EFFECT OF RENAL DENERVATION ON ACTHJNDUCED HYPERTENSION IN SHEEP," Clinical and Experimental Pharmacology and Physiology **8**, 203-207 (1981).
41. R. R. Anderson and J. A. Parrish, "Selective Photothermolysis: Precise Microsurgery by Selective Absorption of Pulsed Radiation," Science **220**, 524-527 (1983).

42. J. A. PARRISH, R. R. ANDERSON, T. HARRIST, B. PAUL, and G. F. MURPHY, "Selective Thermal Effects with Pulsed Irradiation from Lasers: From Organ to Organelle," J Investigative Dermatology **80**, 75s-80s (1983).
43. M. N. Islam, "Laser-based method and system for selectively processing target tissue material in a patient and optical catheter assembly for use therein," (2011).
44. W. Yan, M. R. Ward, G. Nelson, G. A. Figtree, and R. Bhindi, " Overcoming Limited Depth Penetration of Optical Coherence Tomography With Wire Bias FREE " J Am Coll Cardiol Intv **5**, e1-e2 (2012).

# Chapter IV

# Active Remote Sensing Using A Near Diffraction Limited High Power Short Wave Infrared Supercontinuum Laser

## 1. Introduction

In the previous chapters so far, we looked at discrete wavelength lasers in the infrared for medical applications either utilizing the selectivity or penetration depth advantage. I will now shift my focus from discrete wavelength sources to broadband laser sources in the infrared, which are attractive light sources for a variety of applications particularly in spectroscopy. In this chapter, I present the development of a 5W all-fiber packaged supercontinuum (SC) laser prototype spanning the short wave infrared (SWIR) wavelength band from ~1.55-2.35 μm. The SC laser is packaged and used in our first SC field trial, where the SC laser is kept on a 12 story tower at the Wright Patterson Air Force Base (WPAFB) and propagated through the atmosphere to a target kept 1.6 km from the SC laser. The SC beam quality and spectral output stability are studied after atmospheric propagation through 1.6 km. The SC laser beam is observed to be nearly diffraction limited with an $M^2$ value of <1.3, when measured using a SWIR camera. Spectral stability measurements at ~1.6 km show a relative variability of ~4-8% depending on the atmospheric turbulence effects at the time of measurement. Atmospheric turbulence is seen to play an important role and must be accounted for, when performing long distance measurements. The developed SC laser is also used as an illumination source for performing spectral measurements of various materials kept at a distance of 1.6 km from the laser. The SC reflectance measurements are compared with

in-lab measurements performed using a quartz-halogen lamp and are seen to be in good agreement.

Light generations in the SWIR wavelengths (~1-2.5 microns) are beneficial for a number of applications in defense, healthcare, quality control, etc [1-3]. Figure 4.1 below shows the atmospheric transmittance from the visible to the mid-IR wavelengths. High transmission is observed in the SWIR bands from ~1.5-1.8 μm and 2-2.5 μm wavelength regions. The presence of the so-called atmospheric windows [4], where losses during propagation are minimal, coupled with the lower scattering in the SWIR wavelengths (compared to the visible wavelengths) makes SWIR light sources particularly attractive for applications such as remote sensing, hyperspectral Light Detection and Ranging (LIDAR), which require long propagation distances through the atmosphere. In addition, a variety of detectors with high sensitivity are also available in this wavelength region[3]. High power broadband sources are also attractive for airborne laser scanning measurements, which has become a well established technique for surface topography measurements as well as for 3D characterization of targets [5-8]. The addition of broadband spectral data to the intensity based scanning can enable active imaging spectrometry in a single shot together with 3-D topographic mapping [8].

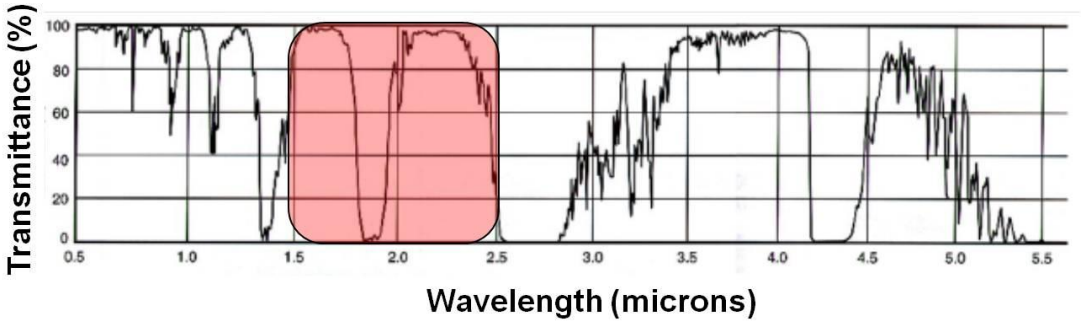


*Fig.4.1.Atmospheric transmission window from the visible to the mid-IR wavelength range (Source: Santa Barbara Research Center).*

Passive SWIR hyperspectral imagers have demonstrated the potential to detect targets of interest, but passive sources like solar illumination have several limitations, such as being confined to day-time operations, shadow regions and being limited by weather conditions [9, 10]. On the other hand, the spectra acquired with an active illumination source, such as SC lasers are not affected by illumination conditions or shadows and allow much more flexibility in measurement conditions and significantly

simplifies post processing [10]. SC lasers sources also have the advantages of conventional laser sources, and can be focused or collimated easily, and are capable of producing near diffraction limited beams[11]. In addition, SC laser sources have a broad wavelength spectrum and high average power, making them attractive light sources for performing measurements over long distances [12]. With the recent development of mature gain fibers, high power pump diodes, optical fibers of various materials, geometries and dispersion profiles, it is now possible to construct a broadband SC fiber laser platform for almost any wavelength of interest from the UV to the mid-IR[1].

The beam quality/divergence, output stability and the average power of the illumination source are three important factors to consider for long propagation distances. Infrared SC lasers have been studied as potential sources for hyperspectral LIDAR [13-15], but these experiments were performed at relatively short distances of < 100m using low power SC sources. Hyperspectral imaging devices generally require the illumination of large areas and hence, high optical powers[16]. Several steps can be taken to reduce the required power of illumination, but at the cost of lower operating SNR, reduced field of view of the sensor, moving the sensor closer to the target, or a combination of both [17]. Therefore, high average power SC laser sources with near diffraction limited beams maybe key enablers for a variety of practical long distance measurements, including air borne measurements.

In this chapter, we present the development of a 5 W SC SWIR laser covering the wavelength region for ~1.55 to 2.35 μm. The laser is packaged and is used as the active illumination source for field trials, where the SC laser is placed on a 76 m tall tower at WPAFB and propagated through the atmosphere to a target on the runway 1.6 km away. The SC laser output leaving the tower is collimated using a parabolic mirror and is used to perform spectroscopy measurements of various targets kept 1.6 km away. The SC beam quality and output spectral stability is also studied after atmospheric propagation through 1.6 km. The SC beam is seen to be nearly diffraction limited with fairly good output spectral stability. We demonstrate that SC laser sources are capable of propagating long distances through the atmosphere with good spectral stability and can be used reliably for long distance spectral measurements. The results presented in this chapter

suggest that SC lasers could potentially be used as active illumination sources for various long distance applications, such as air-borne measurements.

This chapter is organized as follows. In section 4.2, I begin with setups used for the WPAFB field trials to characterize the SC laser and to perform spectral reflectance measurements. This is followed by a description of the 5W SC laser prototype used in the 1.6 km field trials. The SC spectrum and preliminary beam quality measurements are also described in this section. Then, in section 4.4, I present the results of the field trial starting with the SC beam quality. Next, the diffuse spectral reflectance measurements performed at 1.6 km using the SC source as an illumination source are presented, followed by the SC output stability results after propagating 1.6 km through the atmosphere. Finally, in section 4.5, we discuss the experimental results, effects of atmospheric turbulence, long term SC stability results and scopes of the SC systems before ending with the conclusions.

## 2. Field Trial Setup

Field trials using the packaged SC prototype are conducted at the Air Force Research Labs, Wright Patterson Air Force Base (WPAFB), in Dayton, Ohio. The field trial layout is shown in Fig. 4.2. The SC laser is placed on a 76 m tall tower and propagated thorough the atmosphere to an 8' x 8' target panel kept 1.6 km away from the tower. The target panel consists of a plywood stand for placement of the target materials of interest used in our measurements. The panel is slightly tilted to create a normal surface with respect to the laser beam propagation angle of ~2.72 deg. The tower-target beam alignment is verified by observing the reflected beam at the tower from a retro-reflecting mirror placed at the target site.

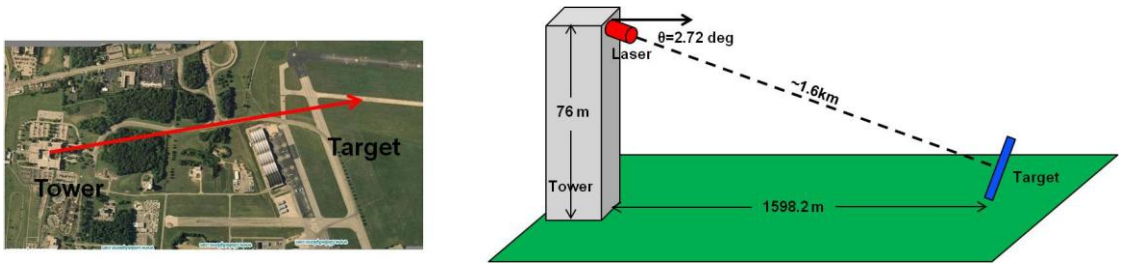


*Fig. 4.2. (a) Map view of 1.6 km tower to ground path at Wright Patterson Air force base (b) Diagram of tower-target test layout*

## 2.1 SC laser setup on tower

A He-Ne beam is used first for beam alignment between the tower and the target. The SC laser is then introduced into the beam path using a set of reflective mirrors. A beam shutter is used to block the beam when required, to make power measurements or background measurements at the target site. SC beam alignment is verified by observing the beam from a retro reflective mirror at the target site on to InGaAs camera on the tower. Figure 4.3 shows and image and a schematic of the laser layout on the tower. The final SC output power leaving the tower after the set of aligning mirrors is measured to be ~ 4.25 W. The SC laser output is directed along a slant path to a target panel on the ground.

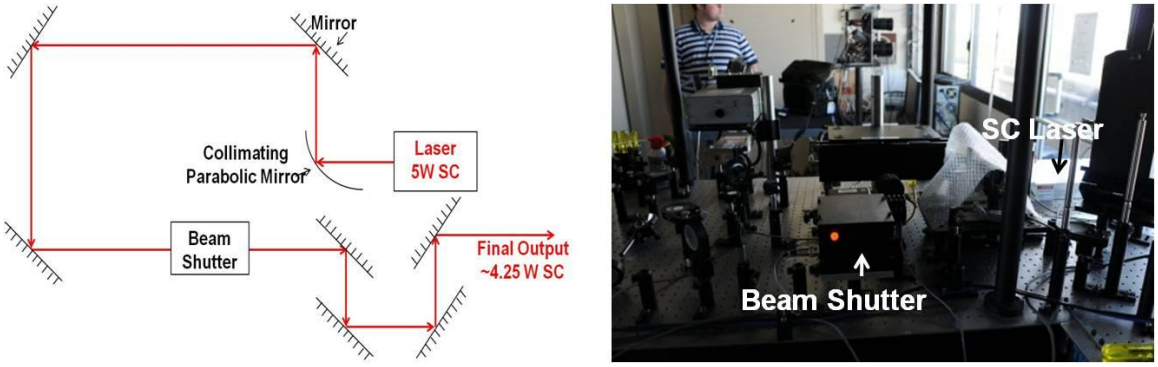


(a) (b)

*Fig. 4.3. (a) SC laser optical layout in the tower at the WPAFB. (b) ) SC laser in the tower at WPAFB.*

## 2.2 Beam Imaging Setup

The SC beam image as projected on the target is measured using a SWIR camera (FLIR Systems SC6702, MA). The camera uses an Indium Antimonide detector and covers the spectral range from ~1-5 microns. The detector resolution is specified as 640 x 512 microns, 15 micron pixels. The images are captured with a 4 ms integration time at 60 frames/second. Figure 4.4 shows the camera layout used in the field trials. The camera is placed ~5.6 m from the target at ~10 degree from the target normal and measures the reflected laser light used to characterize the SC beam quality and the atmospheric turbulence effects.

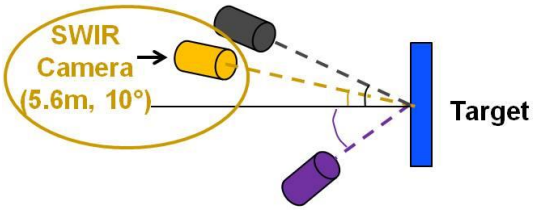



(a) (b)

*Fig. 4.4. (a) Overhead view of the SWIR camera setup used for the beam quality measurements and (b) an image of the SWIR camera*

### 2.3 Diffuse Spectral Reflectance Measurement Setup

The field spectroscopy measurements using the SC laser are performed using a grating based spectroradiometer SR1 (ASD Fieldspec3, CO) with InGaAs detectors that cover the wavelengths from 1-2.5 microns. Figure 4.5 shows the layout for SR1 used for the diffuse reflectance measurements in the field trials. The spectroradiometer is kept ~ 2 m from the target at an angle of ~30 degrees with respect to the target normal. Materials used for the spectral reflectance measurements include Tyvek, a white cotton cloth, wallboard, plywood, gray painted plywood, blue tarp, gray silt cloth and black silt cloth. In order to compare the reflectance data obtained using the SC laser, reference measurements are also performed in lab for each of the samples using a conventional quartz-halogen based tungsten filament lamp and a fiber optic probe attached to the same spectroradiometer SR1.

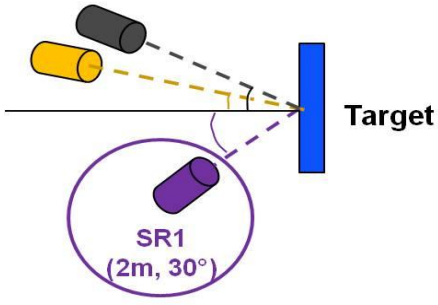


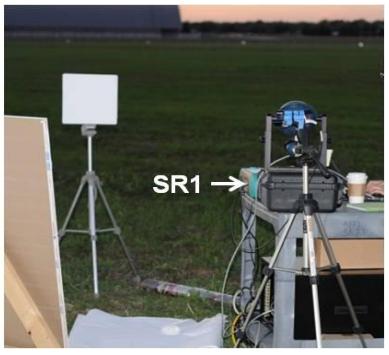


(a) (b)

*Fig. 4.5 (a)Overhead view of the spectroscopy setup showing locations from target to SR1. (b) Image of SR1 used for the diffuse reflectance measurements.*

## 2.4 Spectral Stability Measurements

The SC output stability is measured using a spectroradiometer SR2 (SVC HR-1024, NY), with InGaAs array detectors that cover the 1-2.5 micron spectral regions. Figure 4.6 shows the layout for SR2 used to measure the spectral output stability in the field trials. SR2 is kept ~4.7m from the target at ~6.6-22.5 deg from the target normal. Using the spectroradiometer, we measure the radiance spectra of the laser spot as projected on the target. The scan time for each measurement is 1s. A measurement sequence with SR2 consists of 60 of these sample scans, each taken every 5 seconds (the timing is limited by the software). The relative variability is then calculated from the measurement sequences.


(a) (b)

*Fig. 4.6 (a)Overhead view of the spectral stability measurement setup showing locations from target to SR2. (b) Image of SR2 used for the apectral stability measurements.*

## 3. SWIR SC Laser

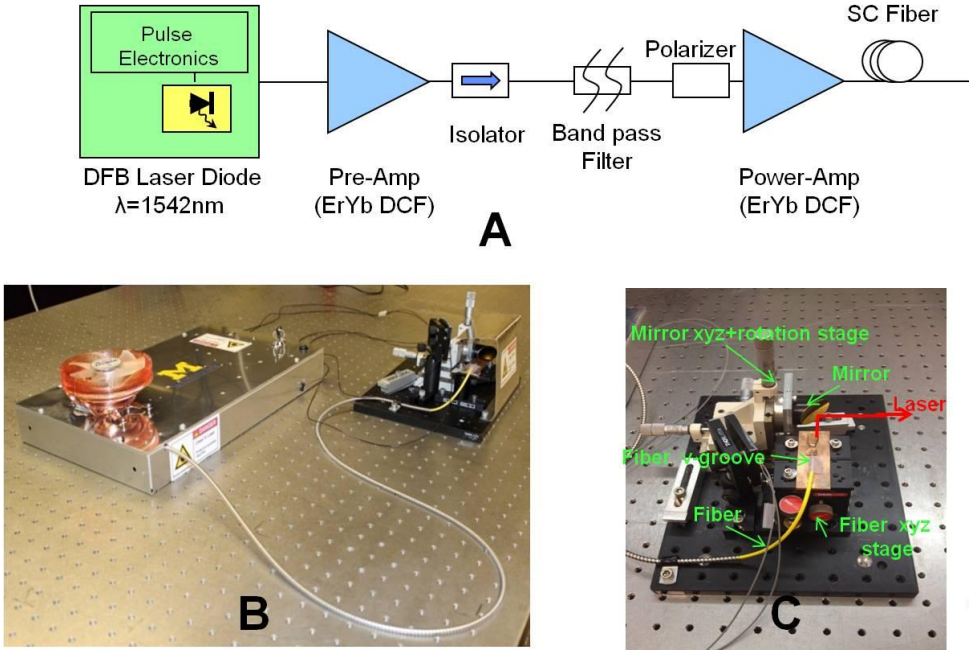


*Fig.4. 7. (a)Optical layout of the all-fiber integrated 5W SWIR SC laser. (b) Packaged 5W SC laser prototype. (c) Collimation setup for the SC final output.*

Figure 4.7a shows the optical layout of the all-fiber 5W SC laser and consists of an amplified 1.54 micron laser source followed by a spectrum broadening fused silica fiber. The amplified 1.54 micron laser source consists of a 1542 nm seed laser diode that is driven by electronic circuits to provide a 0.5 ns pulse at variable repetition rates from ~20 MHz down to a few KHz. These pulses are amplified by two Erbium Ytterbium fiber amplifier (EYFA) stages designated as the pre-amplifier and the power-amplifier respectively. The pre-amplifier consists of a ~2 m length of 12/130 microns (core/cladding diameter) EYFA pumped by a 940 nm diode laser, and the power amplifier consists of ~7 m length of 12/130 microns (core/cladding diameter) EYFA pumped by a ~25 W 940 nm diode. A 100 Ghz band pass filter is used after the pre-amplifier to filter out the amplified spontaneous emission. An in-line polarizer is used at the filter output to ensure that the input to the power-amplifier is in the optimum polarization. The amplified 1540 nm light is then spliced onto ~10 m length of 8/125 microns (core/cladding diameter), 0.125 NA, PM1550 fiber, which generates the SC through the interplay of various non-linear phenomena such as modulation instability and

stimulated Raman scattering[1]. The SC laser is packaged in a box with dimensions of 10”x17”x2” and is shown in Fig. 4.7b. The SC fiber output is collimated and mounted on to a breadboard to allow for easy integration into the WPAFB setup for the field trials. The SC collimation setup is shown in Fig. 4.7c and uses a 90deg off-axis parabolic gold coated mirror with a 25.4 mm focal length. The collimated beam diameter ($1/e^2$) at 1 m is measured to be ~6.5 mm.

Figure 4.8 shows the spectral output from the SC laser prototype corrected for the detector and grating response. The SC spectrum extends from ~1.55 to ~2.35 μm with a time averaged power of ~5.05 W in the entire continuum. The input to the EYFA comprises of 1.54 μm laser diode input pulses of ~0.5 ns duration at 8.3 MHz repetition rate. In this case, the power amplifier is pumped with ~ 25 W of 940 nm pump power and outputs ~ 7 W of average power around 1.54 μm. The pump (940 nm) to signal (1540 nm) efficiency at the output of the power-amplifier is observed to be ~ 28% and is typical of EYFA based SC systems. The SC output power scaling with pump power is shown in Fig 4.8b.

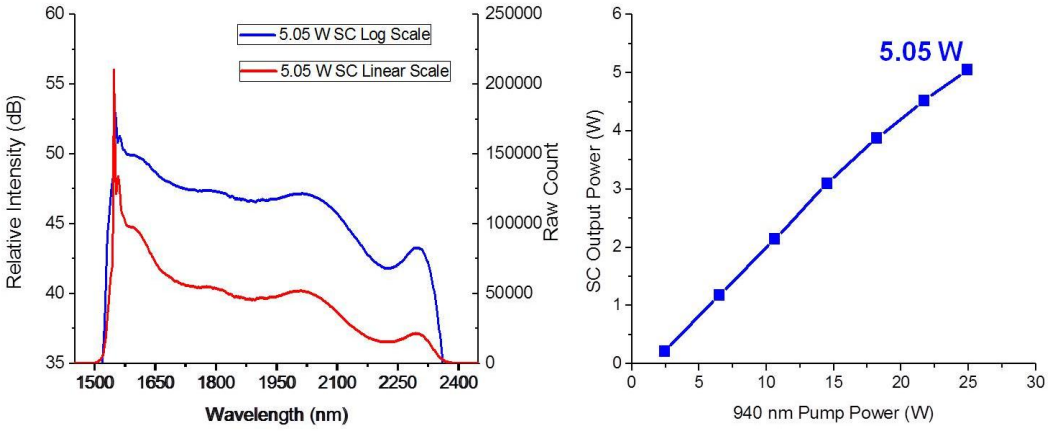


*Fig.. 4.8. (a) SC output spectrum spanning from ~1.55 to 2.35 μm with an average power of ~5W across the continuum. (b) SC output power scaling with 940 nm pump power.*

Before proceeding to the field trials at WPAFB, we verify that we are able to see the beam at a long distance and that the full angle divergence is close to our specification (our specification for the field trial was a full angle divergence of < 1 mrad). This experiment is performed at a local air field (Honey Acres airfield, Clinton, MI) shown in Fig. 4.9a and the beam diameter is measured after propagation through ~720 m. The

beam is projected on a black foam board and oberved using an infrared themal viewer. The thermal viewer only shows the heat distribution across the board and is not an accurate indicator of the beam diameter. Nevertheless, this would still give us a rough idea of the beam divergence. The infrared viewer image of the beam is shown in Fig 4.9b. The FWHM beam diameter is calculated as the distance between the two points, where the temperature is half of the maximum value. A slight ellipticity is oberved in the thermal image, which is most likely due to the target surface being at an angle with respect to the beam. The $1/e^2$ beam diameter is then apprximated as 1.69 x FWHM for a Gaussian beam. At ~720 m, the $1/e^2$ beam diameter from Fig. 4.9b is calculated to be ~44.5 cm. This corresponds to a full angle divergence of ~0.6 mrad and is well within our required specification of < 1 mrad.

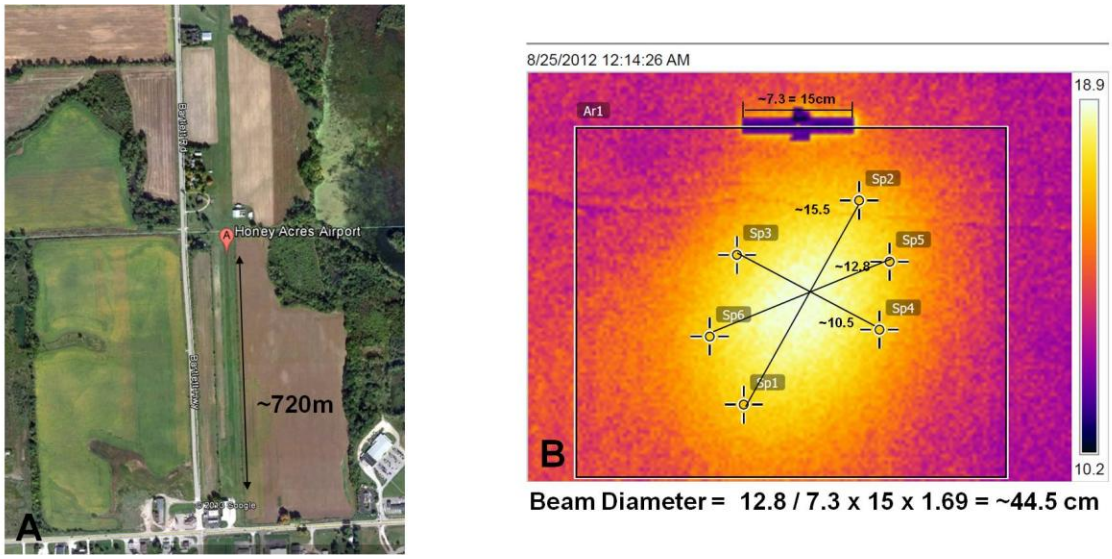


*Fig.4. 9. Preliminary beam divergence measurements (a) Map view of airfield ~720 m used for measurements. (b) Infrared thermal viewer image of the beam at ~720 m corresponding to a full angle divergence of ~0.6 mrad, well within our specification of < 1 mrad.*

## 4. Experimental Results

The results of the 1.6 km field trial are presented in this section beginning with the beam quality measurements, where the SC laser beam is seen to be nearly diffraction limited with an $M^2$ value of < ~1.25. Next the diffuse spectral reflectance measurements of various samples are performed at 1.6 km illuminated using the developed SC laser prototype. The spectral features for the various samples from the spectroscopy measurements using the SC laser are also compared to in-lab measurements using a

quartz-halogen lamp and are seen to be in good agreement. Finally, the output spectral stability measurements after propagation though 1.6 km of atmosphere is presented. The relative variability is measured to be ~4-8% and seen to depend on atmospheric turbulence effects.

### 4.1 SC Beam Quality Measurements

Figure 4.10a shows a camera image of the collimated SC laser beam profile as projected on a target after 1.6 km of atmospheric propagation. Tyvek material is used as the target for these measurements, since this material possesses high reflectance in this wavelength region. The profile shown is an average of 1000 frames measured using a 4 ms integration time. The beam diameter is measured as follows. First, the beam profile obtained using the camera is fit to a Gaussian profile. Then, the beam full width at half maxima (FWHM) is measured from the Gaussian fit. Figure 4.10 (a and b) shows a picture of the beam as projected on the target and the 3D image of the beam corresponding to the camera image. Figure 4.10c shows the beam profile through the beam cross section and the corresponding Gaussian fit.

At full power, the SC beam at 1.6 km is seen to be fairly Gaussian and symmetric (FWHMx=0.45 m, FWHMy=0.47 m), where the average FWHM is measured to be ~0.46 m, corresponding to a $1/e^2$ diameter of ~0.78 m. From the measured beam diameter and the ~1.6 km distance, the full angle beam divergence of the SC beam is then calculated to be $\theta_{SC\,Beam} = 2 \times \tan^{-1}\left(0.39/1600\right) = 0.487 mrad$. For an ideal Gaussian beam at the SC average wavelength of ~2 microns and a similar collimated beam waist diameter of ~6.5 mm as the SC beam, the full angle beam divergence can be calculated as $\theta_{Ideal} = 2 \times \lambda / (\pi \times w_0) = 2 \times 2 \times 10^{-6} / (\pi \times 3.25 \times 10^{-3}) = 0.392 mrad$.

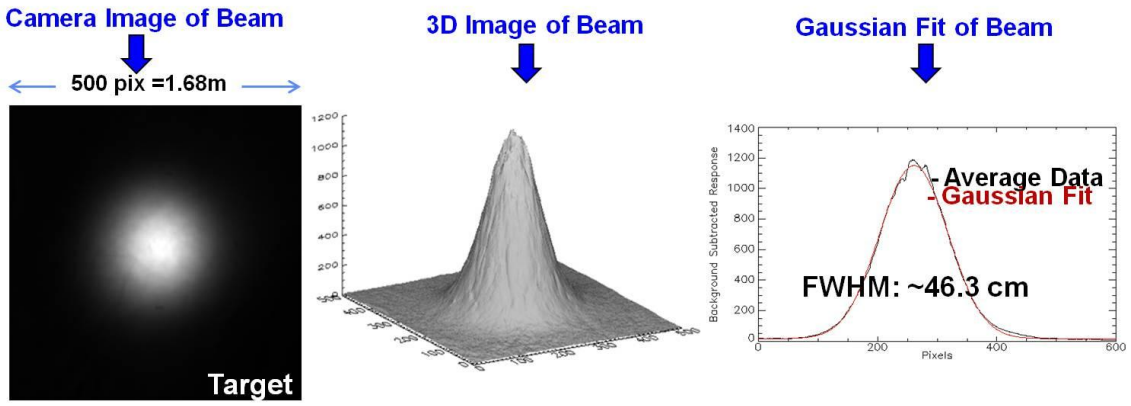


(a) (b) (c)

*Fig. 4.10. SC laser(EYFA system) beam profile measurements at ~1.6 km; 1000 frame average (a) Camera image of the beam (b) 3 D image of the beam (c) Gaussian fit and beam width measurement.*

The $M^2$ factor is a common measure of the laser beam quality and is used to quantify the ratio of divergence of the actual laser beam to an ideal Gaussian beam. An ideal Gaussian beam has an $M^2$ value of 1. Thus, the $M^2$ value indicates how close in divergence, and hence, diffraction limited the laser beam is, compared to an ideal Gaussian beam. The SC $M^2$ value is calculated using the ratio of the SC beam divergence and the ideal Gaussian beam divergence, and is seen to be $\theta_{SC\,Beam} / \theta_{Ideal} = \sim 0.487 / 0.392 = \sim 1.24$. The calculated SC $M^2$ value of ~1.24 from the measurements at 1.6 km indicates that the SC beam is nearly diffraction limited.

### 4 .2 SC Spectral Reflectance Measurements at 1.6 km

After verifying the SC beam propagation through 1.6 km, the tower based SC laser is used as an illumination source to perform spectral reflectance measurements of various materials, to determine if the laser provides enough signal at ~1.6 km to retrieve spectral information from the targets. The field measurements are performed after sun set to minimize solar illumination effects. In order to perform reflectance retrieval measurements using the spectroradiometer SR1, a spectrally-flat "white" reference material is required. A 2' x 2' spectralon, held at the same illumination/viewing angle as the various targets is used as the white reference for our measurements.

Figure 4.11 shows the retrieved spectral reflectance for the various samples measured using the SC laser averaged over at-least five measurements for each sample, and the corresponding in-lab reflectance measurements. The measurements are performed in wavelength steps of 1 nm. The in-lab measurements are collected in a more controlled setting using a quartz-halogen filament lamp as the light source and a fiber optic contact probe. The SC data in the wavelengths from ~1.8-1.95 microns is absorbed by the water in the atmosphere and has been removed from the figure. As can be seen in Fig. 4.11, the spectral reflectance curves for the various samples agree closely with the lab measurements, especially with respect to the spectral shape of the curves. For many of the materials, a reflectance offset exists between the lab measurements and the SC laser measurements. This is most likely the result of non-lambertian target surfaces and differences that exist between the illumination/viewing geometry for the lab and field measurements.

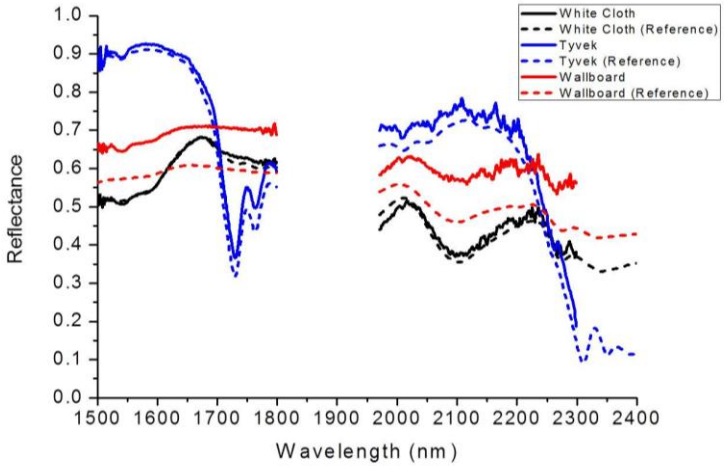


(a)

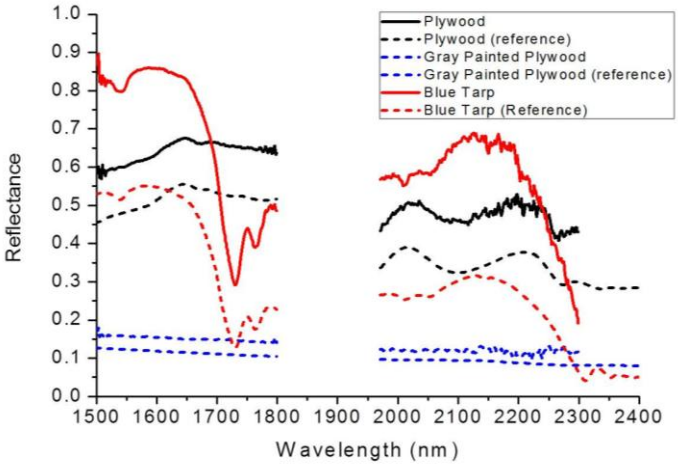


(b)

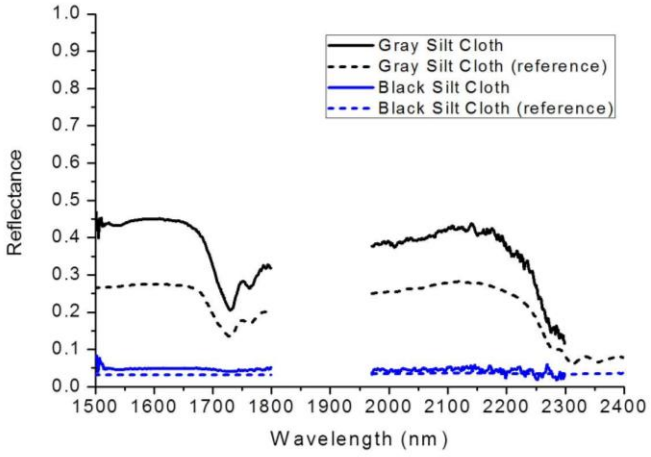


(c)

*Fig. 4.11. Spectral reflectance measurements at ~1.6 km using the SC laser(solid lines) and their comparison to in-lab measurements performed using a quartz-halogen lamp (dashed lines) . (a) Retrieved reflectance of white cloth, tyvek, and wallboard (b) Retrieved reflectance of plywood, gray painted plywood and blue tarp (c) Retrieved reflectance of gray and black silt cloth.*

The spectroradiometer SR1 used for the spectral reflectance measurements uses a grating with a linear 512 element detector for the VNIR (0.3-1μm), an oscillating grating and a detector for SWIR band1 (1-1.83 μm) and another grating/detector pair for the SWIR band 2 (1.8.-2.5 μm). Since our experiments with the SC laser cover the ~1.5-2.3 μm, we use 2 of the three spectral regions covered by SR1. The spectral offset for the samples measured in Fig. 4.11 using the SC appear to be a fairly constant offset compared to the reference spectrum, which suggests that the offset is likely wavelength independent. For eg, Fig 4.12 shows the spectral measurements for three samples: blue

tarp, plywood and gray silt cloth that have been corrected using constant factors in each wavelength band to match the corresponding reference spectrum in that band. As we can see in Fig. 4.12, majority of the spectral offset between the SC and the reference spectra is accounted for with a constant correction factor. Other possible reasons for the offset could be wavelength dependent scattering arising from the sample surface features (roughness, surface profile, etc), changes in the incident/reflection angle of the illumination , atmospheric effects, etc . The wavelength dependence of scattering on the surface features and the incident angle of illumination are further discussed in chapter VI. However, these factors appear to play a minor role in our current measurement configuration, since most of the SC spectral features overlap fairly well with the reference spectra after the application of just a constant offset factor.

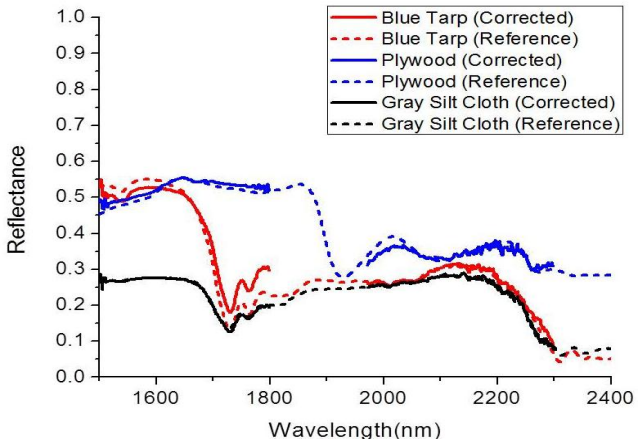


*Fig 4.12. Reflectance spectra for blue tarp, plywood and gray silt cloth corrected with constant offset factors in each of the SWIR wavelength bands. The SC measurements overlap fairly well with the reference measurements after the applications of a the constant offset factors in each on the SWIR wavelength bands.*

### 4.3 SC Output Stability Measurements

In order for the SC source to be useful as a broadband illuminator for various applications, it must provide stable irradiance. Using spectroradiometer SR2, we measure the radiance spectra of the laser spot as projected on the target at 5-second intervals (the timing is limited by the spectroradiometer software). The scan time for each measurement is 1sec, during which the spectroradiometer continuously collected and averaged data. Figure 4.13a shows a sample measurement sequence of 60 such scans. To quantify the variability, we calculate the RMS sample-to-sample difference in radiance at each wavelength band and divided by the mean radiance spectrum. Figure 4.13b shows the variability profiles for 8 measurement sequences over 2 days.

Radiometric variations in the field experiment include atmospheric effects that are not present at significant levels in the lab. The observed radiometric variability is between ~4-8%, depending upon the turbulence conditions.

The refractive index structure parameter ($Cn^2$) value is often used as a measure of atmospheric turbulence and is a function of the local differences in temperature, moisture and wind velocity. The $Cn^2$ values observed in the atmospheric surface layer generally range form $10^{-12}$ $m^{-2/3}$ to $10^{-16}$ $m^{-2/3}$, where higher values indicate a higher atmospheric turbulence [18]. The time stamps on the SC measurements are correlated to the scintillometer data collected by Air Force Research Lab to extract the ($Cn^2$) value corresponding to each SC measurement sequence. Although the $Cn^2$ values are measured at 880 nm, which is outside of the SC range, there is a general correlation between the $Cn^2$ and the relative variability. As seen in Fig. 4.13b, the SC relative variability seems to follow this trend as well, where higher variability is associated with higher $Cn^2$ value. Thus, atmospheric turbulence is an important factor to consider in measurements involving propagation through long distances in the atmosphere.

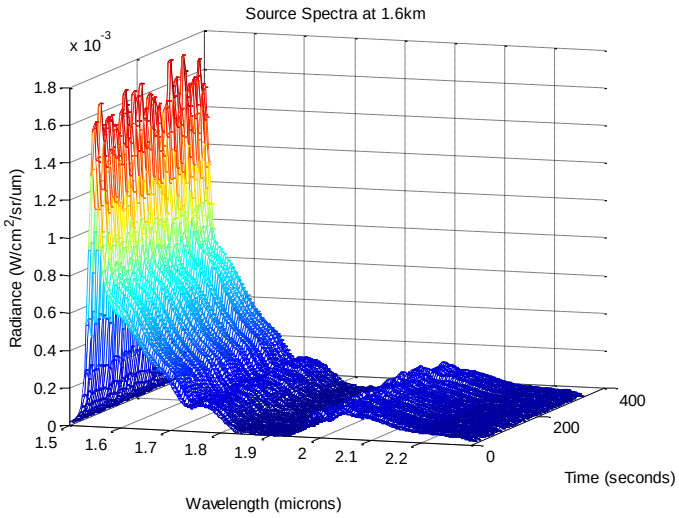


(a)

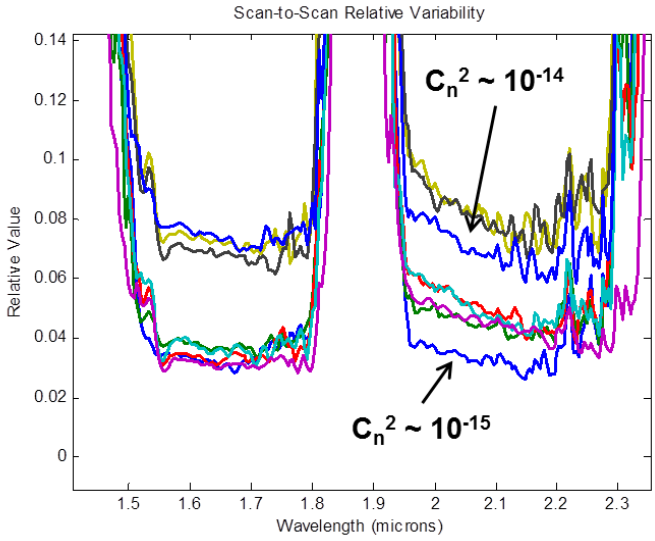


(b)

*Fig. 4.13. (a) Sample measurement sequence of radiance spectra at 1.6km range. (b) Relative scan-to-scan variability for 8 field measurements.*

On a quicker time scale, the SC amplitude fluctuations are also measured at various wavelengths tuned using a spectrometer and lockin amplifier shown in Table 4.1. The measurements are performed at an integration times of 100 ms (2 Hz sampling) using an InGaAs detector. The % fluctuation at each wavelength is calculated as the ratio of the standard deviation and the mean of the measured amplitudes. The fluctuations are measured at 1.6, 1.8, 2 and 2.2 μm. The measured amplitude fluctuations show that the SC laser is stable with < 0.5 % fluctuation across the spectrum at an integration time 100 ms. The fluctuations measured in lab give an indication as to the stability of the SC laser in the absence of external factors like atmospheric turbulence and the data in table4.1 suggests that the turbulence plays an important role in the stability of the SC laser after propagation through the atmosphere.

*Table 4.1. 5 W SWIR amplitude fluctuations at different wavelengths measured in lab**

| **Wavelength (nm)** | **% Fluctuation (Integration Time 100 ms)** |
|---|---|
| 1600 | 0.19 % |
| 1800 | 0.17 % |
| 2000 | 0.17 % |
| 2200 | 0.48 % |

*0.5 ns FWHM Pulse Width, 8 MHz Repetition Rate
* 2Hz sampling for 100 ms, with spectrometer, lock in and InGaAs detector
*% fluctuation= Stdev / Average

## 5. Discussion

SC lasers are attractive illumination sources for hyper-spectral imaging and remote sensing applications. These laser sources cover a broad wavelength region, can be easily collimated to provide near diffraction limited beams and are capable of producing high average power outputs. While the SC laser presented here cover the ~1.55-2.35 μm region of the SWIR band, the SC generation architecture presented in this paper allows for the customization of the various components to potentially generate an SC across the entire SWIR band(~1-2.5 μm), by choosing the appropriate gain and SC generation fibers [1]. The SWIR wavelength band is especially attractive for SC lasers, since this wavelength region allows the use of standard fused silica fibers for SC generation, which are generally much easier to handle and have a higher power damage threshold compared to other fibers, such as fluoride fibers [11]. As shown in section 3, we have developed an all fiber 5W SC laser covering the SWIR bands from ~1.55 to 2.35 μm, after which the long wavelength edge of the fused silica fiber based SC laser is limited by the soaring absorption of silica glass[19].

The beam quality measurements in section 4.1 show that the developed SC laser is capable of producing a nearly diffraction limited beam with an $M^2$ value < 1.3. Theoretical modeling of the SC laser beam propagation has also been performed and show good agreement with the measured laser beam profile[20]. It is worth noting that the measured beam diameters and the $M^2$ values depend strongly on the collimating optics used and how well collimated the beam is. In our case, we use a gold coated parabolic mirror to collimate the SC beam and to avoid any effects of chromatic aberration, but it was not possible for us to easily optimize the collimation during the field due to time limitations. High power SC lasers have also been reported in literature with $M^2$ values ranging from 1.06-1.08 [21].

The atmospheric turbulence affects SC output stability and adds an additional noise term that must be accounted for when trying to predict the operational performance of light sources [20]. Figure 4.14a shows a single frame camera image of the 5W SWIR beam at ~1.6km, where the effects of atmospheric turbulence on the beam are evident. Some of the possible ways to mitigate the turbulence effects on beam quality are averaging of multiple camera frames, performing background subtraction, etc. As an

example, Fig. 4.14b shows a 1000 frame average of the same laser beam after background subtraction, where the beam is seen to be much more stable. Thus, the effects of atmospheric turbulence must be considered in the laser system designs [22]. A variety of techniques, such as using adaptive optics, deformable mirrors, beam dithering etc, have been investigated in literature to mitigate the effects of atmospheric turbulence in laser beam propagation [23-25] .

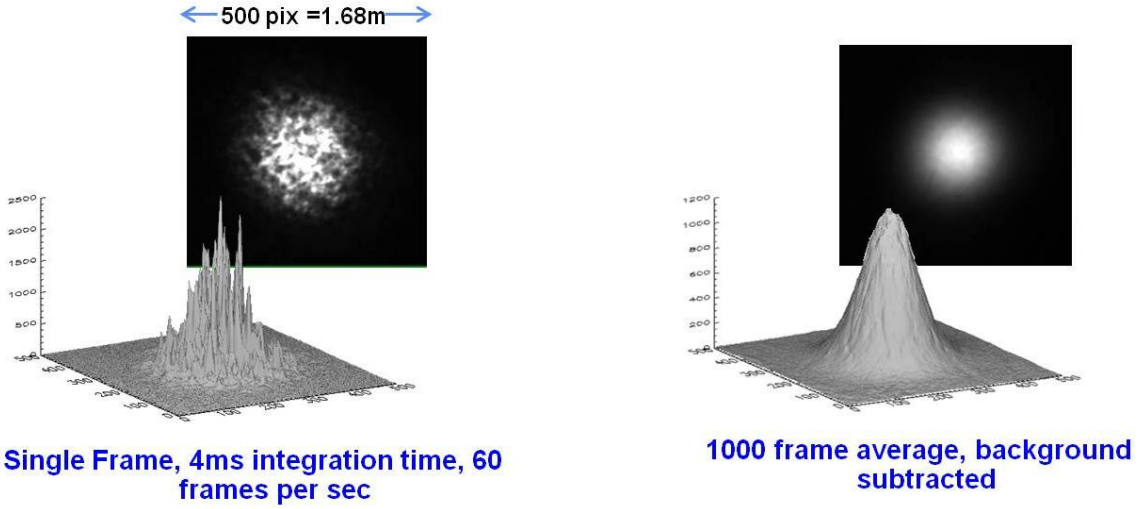


*Fig. 4.14. (a) Single frame image of the SC laser beam at ~1.6 km. showing effects of atmospheric turbulence. (b) 1000 frame average of the same beam with background subtraction showing a much smoother beam profile.*

The output power stability over long periods is another factor to consider in a practical light source for long term measurements. We have performed power stability measurements for a continuous >43 hour time period on the final system. The final power is measured at the output without a collimating mirror. The results are shown in Fig. 4.15 and show an average power of ~5.09 W with a standard deviation of 0.012 W, corresponding to a fluctuation of ~0.23%. The small variation is most likely due to the temperature fluctuations in the room temperature. Since our pump diodes are passively cooled, it is possible for the pump center wavelength to fluctuate with temperature, which could affect the final SC power level.

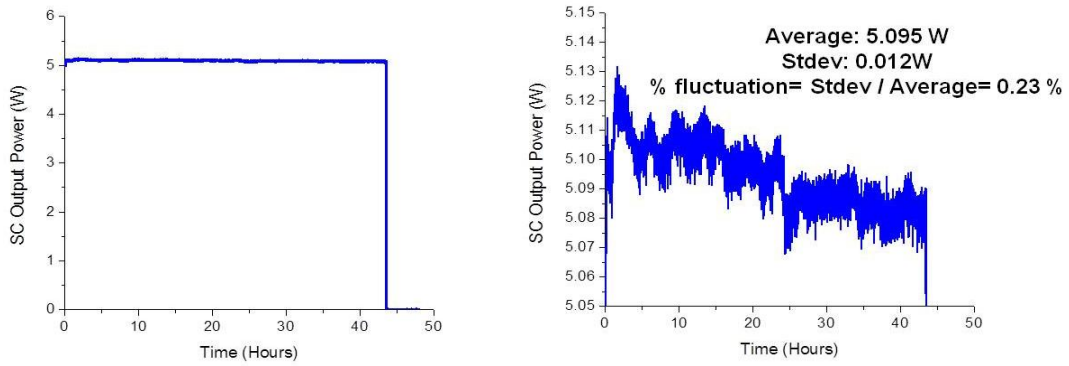


*Fig. 4.15. Long term power stability measurements of the 5 W SC prototype (Left) Zoomed in view (Right)*

High average power SC lasers are potential key enablers for practical long distance/airborne hyperspectral imaging and remote sensing applications, where speed and signal quality play an important role. For the SC laser presented here, the power scaling is limited by the available 940 nm pump power. The maximum average power handling capability of the fiber may be limited to when the temperature of the fiber core rises close to its melting point. By increasing the pump powers and with better thermal management and heat dissipation techniques, it should be possible to further scale up the average power output of these all-fiber SWIR SC lasers. For example, Xia et al., estimate the damage threshold in a standard fused silica single mode fiber based SC system, where the fiber dimensions are comparable to our current system, to be > 60 W [11]. In our current setup the spectroradiometer is placed ~2 m from the target to ensure sufficient signal. A higher average power SC will allow the detector to be placed farther away from the target, where the end goal might be to have a transceiver design consisting of both the source and detector in one unit. An added advantage of SC laser architecture presented here is the ability to scale up the average output power, while maintaining the same spectral extent, by increasing the repetition rate and the corresponding pump powers. For example, in the next chapter, I present an SC laser using similar architecture as the laser presented here, where the average SC output power is scaled up from 5 W to 25.7 W in a spectrum extending from ~2-2.5 microns, by increasing the repetition rate from ~0.2 to ~1.1 MHz. In addition, we will also show that the SC laser is truly power scalable, in that the SC maintains a near constant spectrum, good beam quality and low output variability as the average output power is scaled up, making the SC laser source a potentially ideal illumination source for long distance remote sensing applications.

## 6. Summary

In this chapter, I present the results of a field trial performed using a developed SC laser source. An all-fiber 5W SWIR SC laser covering the ~1.55-2.35 microns wavelength band is developed and placed on a 76 m tall tower at the Wright Patterson Air Force Base (WPAFB) and propagated through the atmosphere to a target on the runway ~1.6 km away. Field trials are performed to characterize the SC beam quality and output stability after ~1.6km of atmospheric propagation. The developed SC laser has a near diffraction limited beam with an $M^2$ value of <1.25, when measured using a SWIR camera. The SC laser is also used as an active illumination source to perform spectral reflectance measurements of various samples at ~1.6 km, and the SC measurements are seen to be in good agreement with in-lab measurements performed using a conventional quartz-halogen lamp. The SC output variability is measured to be ~4-8% and is seen to depend on the atmospheric turbulence effects. The high average power, broad spectrum and the convenience of an all-fiber integrated laser source with near diffraction limited beam quality makes the SC lasers presented here, an attractive light source for active illumination in the SWIR wavelengths for long distance hyperspectral imaging and remote sensing applications.

## References


1. V. V. Alexander, O. P. Kulkarni, M. Kumar, C. Xia, M. N. Islam, F. L. T. Jr., M. J. Welsh, K. Ke, M. J. Freeman, M. Neelakandan, and A. Chan, "Modulation instability initiated high power all-fiber supercontinuum lasers and their applications," Opt Fiber Technol **18**, 349-374 (2012).
2. S. D. Jackson, "High-power fiber lasers for the shortwave infrared," Proc. SPIE 7686, Laser Technology for Defense and Security VI, 768608 (2010).
3. M. P. Hansen and D. S. Malchow, "Overview of SWIR detectors, cameras, and applications," Proc. SPIE 6939, Thermosense XXX, 69390I (2008).
4. J. H. Taylor and H. W. Yates, "Atmospheric Transmission in the Infrared," J. Opt. Soc. Am **47**, 223-225 (1957).
5. K. Kraus and N. Pfeifer, "Determination of terrain models in wooded areas with airborne laser scanner data,," ISPRS J. Photogramm. Remote Sens. **53**, 193-203 (1998).
6. J. Hyyppä, O. Kelle, M. Lehikoinen, and M. Inkinen, "A segmentationbased method to retrieve stem volume estimates from 3-D tree height models produced by laser scanners," IEEE Trans. Geosci. Remote Sens. **39**, 969-975 (2001).
7. N. Haala and C. Brenner, "Extraction of buildings and trees in urban environments," ISPRS J. Photogramm. Remote Sens. **54**, 130-137 (1999).
8. S. Kaasalainen, T. Lindroos, and J. Hyyppä, "Toward Hyperspectral Lidar: Measurement of Spectral Backscatter Intensity With a Supercontinuum Laser Source," IEEE GEOSCI REMOTE S **4**, 211-215 (2007).
9. G. Bishop, I. V. Veiga, M. Watson, and L. Farr, "Active Spectral Imaging for Target Detection," in *4th EMRS DTC Technical Conference*, 2007),
10. M. L. Nischan, R. M. Joseph, J. C. Libby, and J. P. Kerekes, "Active spectral imaging," Lincoln Laboratory Journal **14**, 131-144 (2003).
11. C. Xia, Z. Xu, M. N. Islam, J. Fred L. Terry, M. J. Freeman, A. Zakel, and J. Mauricio, "10.5 W Time-Averaged Power Mid-IR Supercontinuum Generation Extending Beyond 4 μm With Direct Pulse Pattern Modulation," IEEE J SEL TOP QUANT **15**, 422-434 (2009).
12. D. A. Orchard, A. J. Turner, L. Michaille, and K. R. Ridley, "White light lasers for remote sensing," in *Proc. SPIE 7115, Technologies for Optical Countermeasures V*, 2008),
13. T. Hakala, J. Suomalainen, S. Kaasalainen, and Y. Chen, "Full waveform hyperspectral LiDAR for terrestrial laser scanning," Opt. Express **20**, 7119-7127 (2012).
14. Y. Chen, E. Räikkönen, S. Kaasalainen, J. Suomalainen, T. Hakala, J. Hyyppä, and R. Chen, "Two-channel Hyperspectral LiDAR with a Supercontinuum Laser Source," Sensors **10**, 7057-7066 (2010).
15. R. Ceolato, N. Riviere, and L. Hespel, "Reflectances from a supercontinuum laser-based instrument: hyperspectral, polarimetric and angular measurements," Opt. Express **20**, 29413-29425 (2012).
16. C. R. Howle, D. J. M. Stothard, C. F. Rae, M. Ross, B. S. Truscott, C. D. Dyer, and M. H. Dunn, "Active hyperspectral imaging system for the detection of liquids," in *Proc. SPIE 6954,* (2008), p. 69540L

17. G. A. Shaw and H.-h. K. Burke, "Spectral Imaging for Remote Sensing," Lincoln Laboratory Journal **14**, 3-28 (2003).
18. A. Tunick, N. Tikhonov, M. Vorontsov, and G. Carhart, "Characterization of optical turbulence (Cn2) data measured at the ARL A_LOT facility," ARL-MR-625 (2005).
19. T. Izawa, N. Shibata, and A. Takeda, "Optical attenuation in pure and doped fused silica in their wavelength region," Appl. Phys. Lett. **31**, 33-35 (1977).
20. J. Meola, A. Absia, J. D. Leonarda, A. I. Ifarraguerri, M. N. Islam, V. Alexander, J. Zadnike, A. S. Szalkowskie, and G. J. Boere, "Modeling, development, and testing of a shortwave infrared supercontinuum laser source for use in active hyperspectral imaging," Submitted to Proc. SPIE (2013).
21. X. Hu, W. Zhang, Z. Yang, Y. Wang, W. Zhao, X. Li, H. Wang, C. Li, and D. Shen, "High average power, strictly all-fiber supercontinuum source with good beam quality," Opt. Lett **36**, 2659-2662 (2011).
22. J. Davis, "Consideration of Atmospheric Turbulence in Laser Systems Design," Appl. Opt **5**, 139-148 (1966).
23. M. C. Roggemann and D. J. Lee, "Two-deformable-mirror concept for correcting scintillation effects in laser beam projection through the turbulent atmosphere," Appl. Opt **37**, 4577-4585 (1998).
24. T. xue-chun, W. zhi-chao, and L. zhu, "Effect of adaptive optical system on the capability of lidar detection in atmosphere," Proc. SPIE **7284**(2009).
25. D. N. Loizos, L. Liu, P. P. Sotiriadis, G. Cauwenberghs, and M. A. Vorontsov, "Integrated Multi-Dithering Controller for Adaptive Optics," Proc. SPIE **6708**(2007).

# Chapter V

# Power Scalable > 25 W Supercontinuum Laser from 2 -2.5 μm with Near Diffraction Limited Beam and Low Output Variability

## 1. Introduction

In the previous chapter, we saw that the SC laser has a near transform limited beam quality, good output stability and can be used to perform long distance spectroscopy. Next, my goal is to present the development of a high power SC laser source bringing us closer to realizing a version that can eventually be used for airborne measurements. Hyperspectral imaging devices generally require the illumination of large areas and hence, high optical powers[1]. Several steps could be taken to reduce the required power of illumination, but at the cost of lower operating SNR, reduced field of view of the sensor, moving the sensor closer to the target, or a combination of both[2]. In this chapter, I present the development of a >25 W SC laser focusing on the atmospheric transmission window from ~2-2.5 microns. One unique aspect of our SWIR-SC lasers is that it is truly a power scalable laser, which we prove by showing 1) a near constant spectral output, 2) good beam quality and 3) low output variability as the power is scaled up from 5 W to 25.7 W.

SWIR light sources covering the ~1-2.5 μm wavelengths are attractive for a variety of remote sensing and medical applications due to low water absorption, low scattering and the presence of spectral signatures for various samples of interest in this wavelength region. High average power SC laser sources covering parts of the SWIR region have been widely studied. Most of these SC lasers are Ytterbium doped fiber

(YDFA) based systems and use photonic crystal fibers for SC generation [3-5]. Recently, a 70 W SC spanning from ~1.06 to beyond 1.7 μm was reported in a nonlinear YDFA using an all-fiber master oscillator power amplifier configuration [6]. A review of high power SC lasers using YDFA based sources are reported in [7]. In most of these cases, the SC architecture does not allow for convenient scaling of the repetition rate and hence, the average power. A gain switched system has also been used to generate SC spanning from 0.5-2.25 μm with ~12 W output corresponding to a spectral density of < ~6dBm/nm in the 2-2.25μm region[8].

Thulium doped fiber amplifiers (TDFA) have lately become of interest for mid-IR SC generation > ~2 μm [9-13]. For example, a 2.37 W SC laser spanning from ~1.75-2.7 μm was recently reported as the highest average power SC generated from a single mode Thulium doped fiber [10]. In this chapter, I present the development of a high power >25 W all-fiber supercontinuum (SC) laser covering the short wave infrared (SWIR) wavelength bands from 2-2.5 μm with a spectral density of >12dBm/nm. We characterize the SC laser performance with power scaling and show that the SC laser is truly scalable as verified by a near constant spectrum, beam quality and output stability, as the average power is scaled from 5 to 25.7 W. Average power scaling is achieved by increasing the repetition rate, and a corresponding increase in the pump power helps to maintain a near constant peak power, resulting in a near constant spectral output. The SC beam quality with power scaling is studied next and seen to be near-diffraction limited with an $M^2$<1.2 for all power levels. Output stability measurements with power scaling are also presented in this section and show a radiometric variability <0.8% across the entire SC spectrum. Finally, I will discuss the results presented and power scaling challenges before ending with the summary and conclusions.

## 2. Experimental Setup

Figure 5.1 shows the optical layout of the 25.7 W SC laser. A two stage approach is used for the SC generation The first stage consists to two ~1.5 μm amplification stages (pre-amp and mid-amp), followed by the second stage ~2 μm amplification stage (power-amp) and the SC generation fiber. The amplified 1.5 μm laser source consists of a 1553

nm seed laser with ~1 ns pulse at 1.1 MHz repetition rate amplified using two Er:Yb fiber amplifier stages, similar to the setup in [9]. Pulse breakup through modulation instability (MI) and long wavelength shifting through Raman processes in an ~12 m standard SMF gives rise to ~2 μm pulsed light components for input to the second stage TDFA. Thus, the MI-initiated SC in the SMF eliminates the need for a mode locked laser for high peak power pulse generation at 2 μm and allows the use of standard telecommunication components in all-fiber architecture.

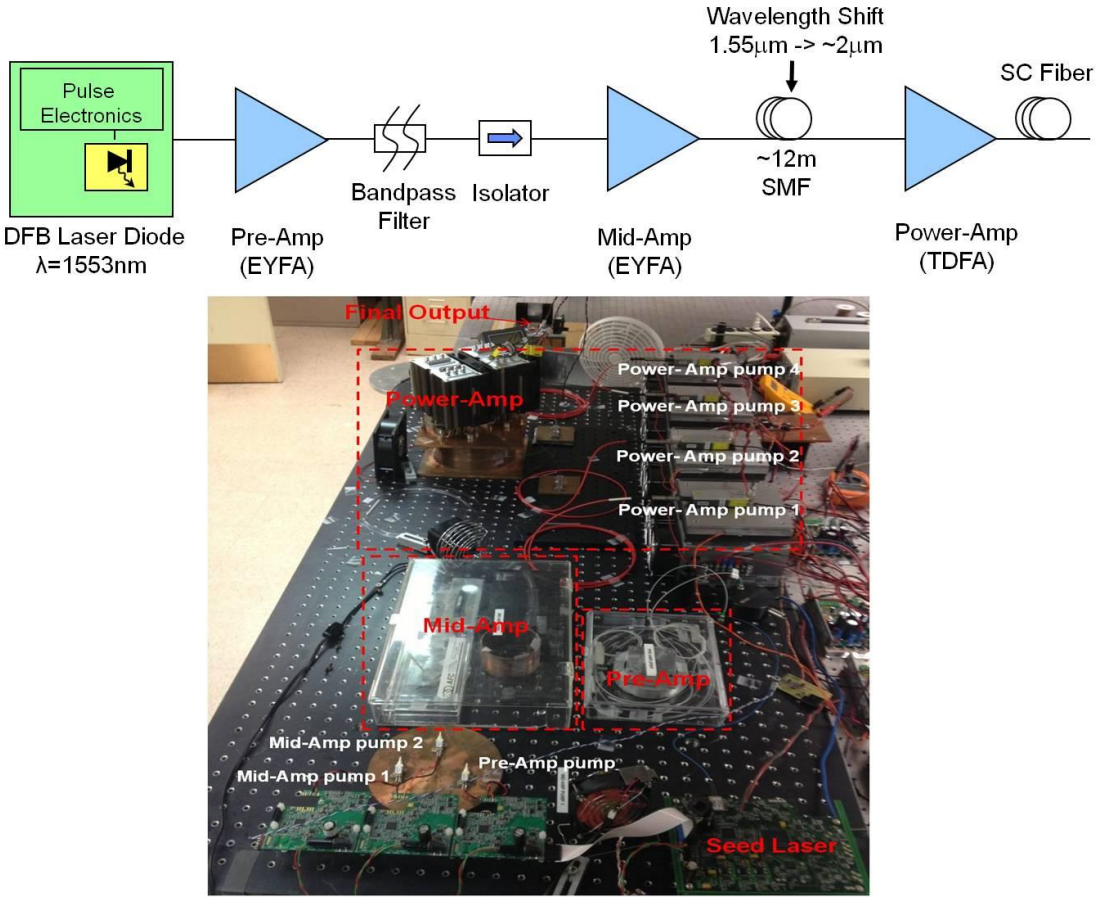


*Fig.5. 1.Block diagram and table top layout of the 25.7W SC laser system*

The output of the first stage SC is then spliced onto the second stage comprising of a TDFA power amplifier stage using a mode field adapter. Mode adaption is usually achieved by heating the fiber to diffuse the cores and/or tapering the fiber to change the core size, thus changing the size of the mode field. The goal is to preserve the energy in the fundamental mode and make the transition in the mode field adapter as adiabatic as possible [14]. The power amplifier consists of ~8 m long 25/400 μm (core/cladding

diameter) TDFA pumped by four 35 W 793 nm pump diodes coupled through a 6x1 pump combiner. By pumping the system with ~112 W in the counter-propagation configuration, we are able to generate ~25.7 W SC at the output. In this case, the 2 m 25/400 μm (core/cladding diameter) silica fiber of the combiner serves as the SC generation fiber. The gain fiber is heat sunk by coiling around a copper mandrel with grooves matched to fit the gain fiber.

The optimum length of gain fiber is experimentally determined based on the SC efficiency measurements obtained using a 25/250 μm TDFA (9.5 dB/m absorption at 793 nm). If the length of the gain fiber is not sufficient, then enough pump light is not absorbed and leads to low SC generation efficiency (combiner output / 790 pump power). On the other hand, if the gain fiber is too long, then the inherent fiber loss will lower the SC efficiency as well. Ideally, we would like to use the shortest length required in order to minimize the non-linear effects in the gain fiber. Figure 5.2 shows the SC efficiency for different lengths for 25/250 μm gain fiber (1 ns pulse, 500KHz repetition rate). It is seen that ~1.5 m of the 25/250 μm TDFA provides the highest SC efficiency. Since the 25/400 mm gain fiber has ~1/4 x the pump absorption as the 25/250 μm, we use ~8 m of the 25/400 μm gain fiber for the high power SC system

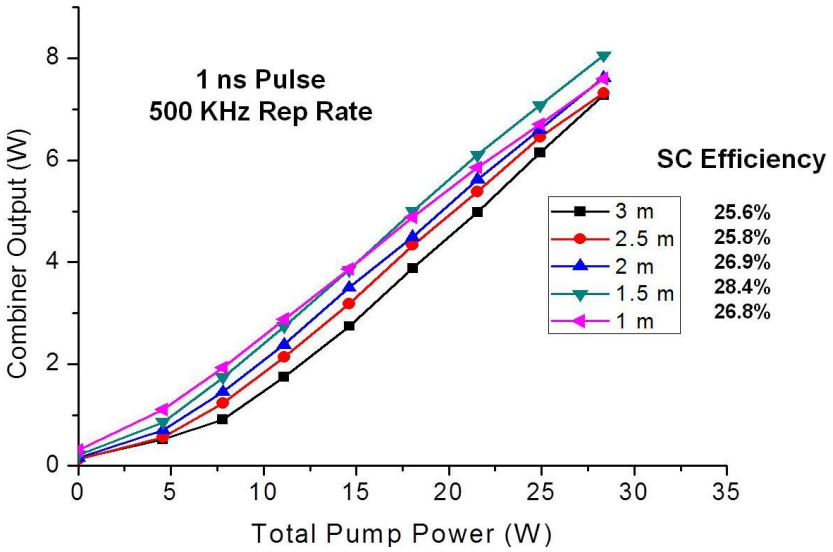


*Fig. 5.2. Measured output power from ~1.5m of combiner fiber versus 793nm pump power for various lengths of the 25/250 μm TDFA.*

The SC output from ~ 2 m of the 25/400 μm core /cladding diameter fiber, corrected for the detector and grating response is shown in Fig.5.3a. The SC extends from ~1.95-2.55 μm with ~25.7 W of time average power in the spectrum. Figure 5.3b shows the power scaling of the SC output to 25.7 W with increasing 790 nm pump power. The TDFA is pumped with ~112 W of 790 nm pump power. The overall SC efficiency in this case is ~ 23 %, which is slightly lower than the ~27 % efficiency reported in [9]. The high output peak power of > 20 kW combined with the ~ 8 m long gain fiber and the ~2m combiner fiber, already gives rise to a continuum at the TDFA output and is most likely responsible for the slightly lower SC efficiency reported here

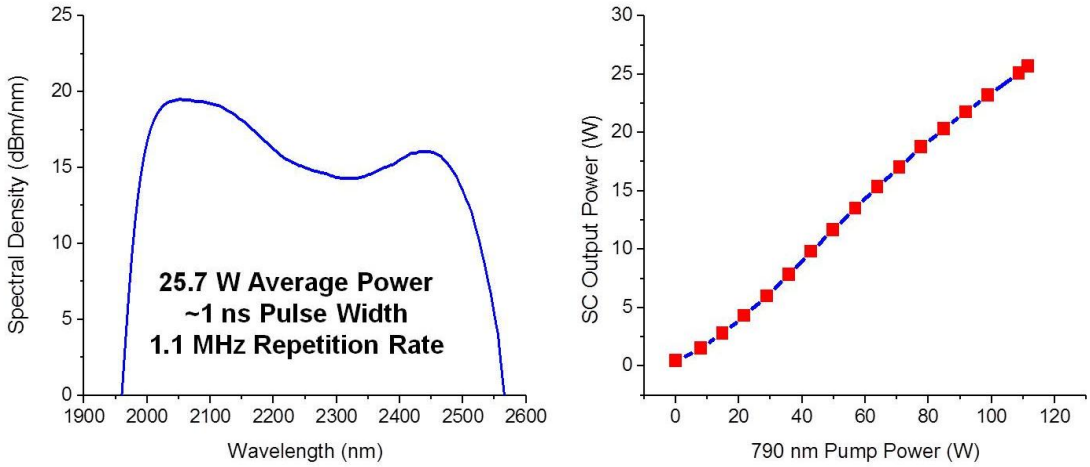


(a) (b)

*Fig. 5.3. (a) 25.7W SC output spectrum (b) SC output power scaling with 793 nm pump power.*

## 3. Experimental Results

In this section, I present the experimental results showing that the developed SC laser is a truly scalable SC laser system. I look at three major factors to verify scalability; the output spectrum, the beam quality and the output stability. I begin by showing that the SC spectrum is nearly constant as the output power is scaled from 5 to 25.7W. Then, I present the beam quality measurements performed using a SWIR camera and show that the $M^2$ value remains nearly constant and is < 1.2 across all power levels. Next, the SC output stability measurements are presented. which show a radiometric variability of < 0.8% across the entire SC spectrum for all power levels. Finally, I also present an

application of the developed SC laser for spectroscopy measurements by performing spectral reflectance measurements of various samples in lab.

### 3.1 SC Output Spectrum with Power Scaling

The average power of the SC system is seen to be linearly scalable with repetition rate, while maintaining nearly the same spectral shape. In our SC systems, the repetition rate couples with the pulse width to determine the duty cycle of the laser system. The spectral width is set by the peak output power, which increases with the reduction of the pulse repetition rate, i.e. pulse duty cycle, and vice versa. Thus, by increasing the repetition rate and the pump power accordingly, we can maintain a nearly constant spectrum, while scaling up the total SC average power. This is seen in Fig. 5.4, which shows the linear scaling of the SC average power from 5 to 25.7W with repetition rate, and the corresponding output spectrum at each of the power levels. It is worth mentioning there is currently no feedback mechanism to maintain a constant final output peak power and therefore it is possible for the peak powers to be slightly higher as the average power is scaled up. This is most likely the cause of the slight increase in the long wavelength edge with power scaling, seen in Fig. 5.4b.

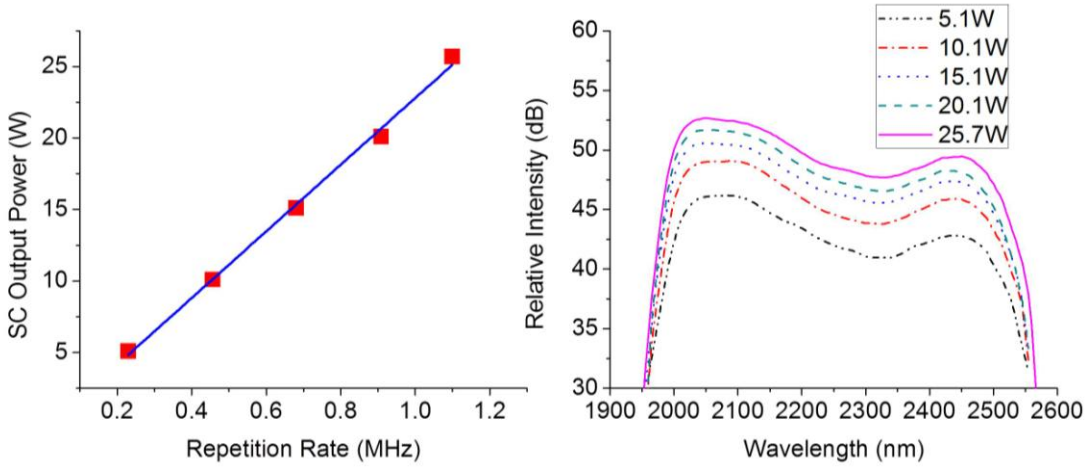


(a) (b)

*Fig. 5.4. (a) Linear scaling of the SC average power with repetition rate. (b) Nearly constant SC output Spectra with average power scaling from ~5 -25.7 W.*

### 3.2 SC Output Beam Quality with Power Scaling

The beam profile of the SC laser with power scaling is studied by projecting the laser beam on a Spectralon target placed ~1.05 m from the SC fiber output, and then observing the beam profile using a SWIR camera. The camera has an Indium Antimonide detector and covers the spectral range from ~1-5 μm. The detector resolution is specified as 640 x 512, 15 μm pixels. For each power level, the beam profile obtained using the camera is fit to a Gaussian profile, from which the beam diameter is then extracted. For example, Fig. 5.5 shows the camera image of the 25.7 W SC beam and the corresponding Gaussian fit.

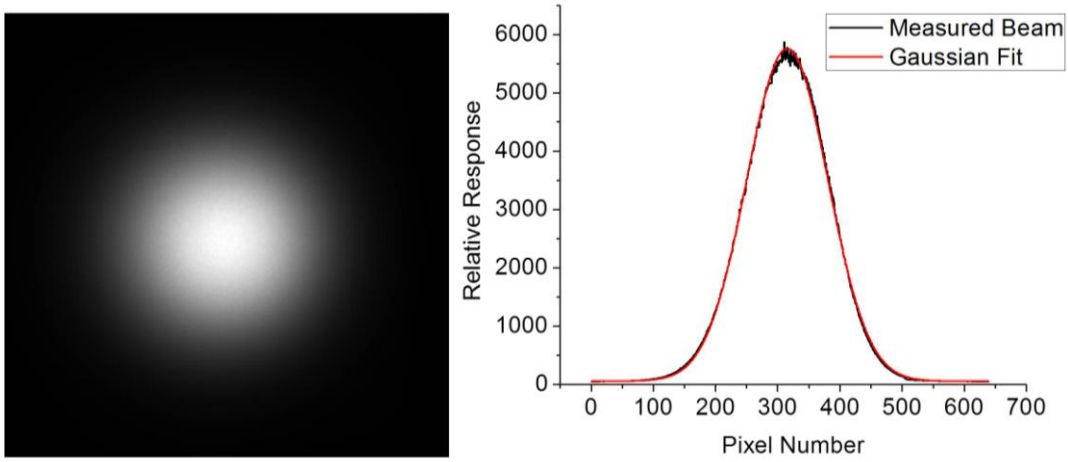


*Fig. 5.5. SWIR camera image of the beam at 25.7 W SC (Left). Corresponding Gaussian fit of the beam cross section at 25.7W (Right).*

Figure 5.6a shows the measured full width at half maximum (FWHM) beam diameter as the power is scaled from 5 to 25.7 W. As can be seen from Fig.5.6a, the average beam diameter is measured to be ~91 mm (+/- 3.5%) across the different power levels. The small increase in the beam diameters may be attributed to the slight increase in the spectral extent towards the long wavelength edge, as the average power is scaled up and the peak output power not being maintained exactly the same with power scaling. Figure 5.6a also shows a +/-2% difference between the x and y diameters at each power level, which may be attributed to the fiber output being angle cleaved. An ideal Gaussian beam at the SC average wavelength of 2.3 μm, and a ~23 μm mode field diameter has a calculated full angle divergence of ~0.13 rad. The SC $M^2$ value is then calculated as the ratio of the SC Beam divergence to ideal Gaussian beam divergence, and is seen to be <1.2 for all power levels (Fig. 5.6b), indicating that the SC laser maintains a nearly

diffraction limited beam with power scaling. Additional $M^2$ measurements are also performed at ~0.47 m from the fiber output by scanning a detector across the beam cross section and range from ~1.16-1.18 across the various power levels.

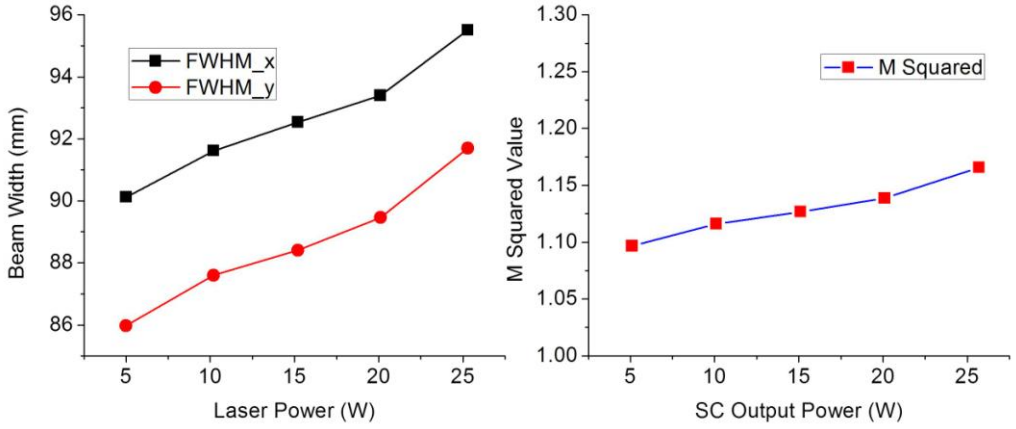


(a) (b)

*Fig.5. 6. SC beam quality measurements using a SWIR camrera. (a) Measured FWHM beam width with power scaling . (b) Calculated $M^2$ measurements with power scaling.*

### 3.3 SC Output Stability with Power Scaling

Another attribute for the SC source to be useful as a broadband illuminator for various applications, is the ability to provide stable irradiance. The output variability of the SC laser spectra with power scaling is studied using a spectroradiometer, where we measure the spectral radiance of the laser spot as projected on the spectralon target, at 5-second intervals (the timing is limited by the software). The actual scan time for each measurement is 1 second. Figure 5.7a shows a sample measurement sequence of ~60 scans at 25.7 W. To quantify the relative variability, we calculate the RMS deviation of the sample-to-sample difference in radiance at each wavelength and divided by the mean radiance spectrum. The measured relative variability of the SC laser spectra is plotted in Fig. 5.7b and is seen to remain below 0.8% across the 1.95-2.5 μm spectral region. Thus, the SC laser maintains a low output variability across the entire SC spectrum as the power is scaled.

Unlike the spectroradiometer, the SWIR camera is able to capture the spatial characteristics of the beam as well as sample at faster rates. We use the camera to record 1000-frame sequences over a 120x120 pixel window in the center of the 25.7 W laser spot, at 10 Hz sampling with an integration time of 20 ms. After subtraction of the

average background (obtained by performing the measurements with the laser off), the relative variability at 10 Hz is measured to be 0.48%, which is consistent with the spectroradiometer results.

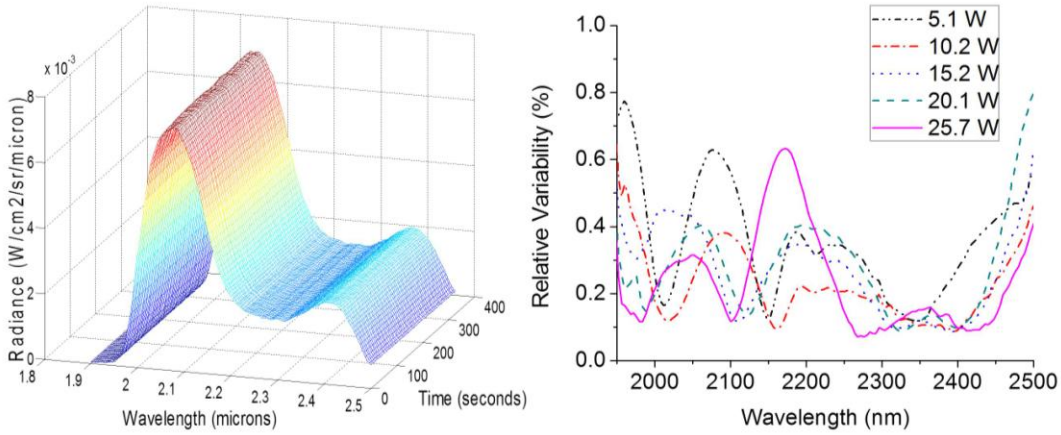


(a) (b)

*Fig. 5.7. SC Output stability measurements. (a) Sixty scan sequence of the 25.7W SC spectra. (b) SC output relative variability with power scaling.*

### 3.4. Spectroscopy Measurements using the SC Laser

As an example application of the developed SC laser for spectroscopy, we also perform diffuse spectral reflectance measurements of various samples using the SC laser as the illumination source. In this case, the power is scaled down to 5W to avoid detector saturation. Three samples: acetate sheet, polystyrene cloth and cotton cloth are chosen for the reflectance measurements. The laser is projected at a normal incident angle on to the samples kept at a distance of ~1.05 m. The spectrometer capturing the reflected light is kept at a distance of ~1m at an angle of ~22.5 deg with respect to the sample normal. The diffuse reflectance spectra for the samples measured using the SC laser and the corresponding reference measurement performed using a conventional halogen lamp source is shown in Fig. 5.8.

As can be seen in Fig. 5.8, the spectral reflectance curves for the various samples agree closely with the reference measurements, especially with respect to the spectral shape of the curves. For some of the materials, a reflectance offset exists between the reference and the SC laser measurements. This is most likely the result of non-lambertian sample surfaces and differences that exist between the illumination/viewing geometry for the SC and lamp measurements.

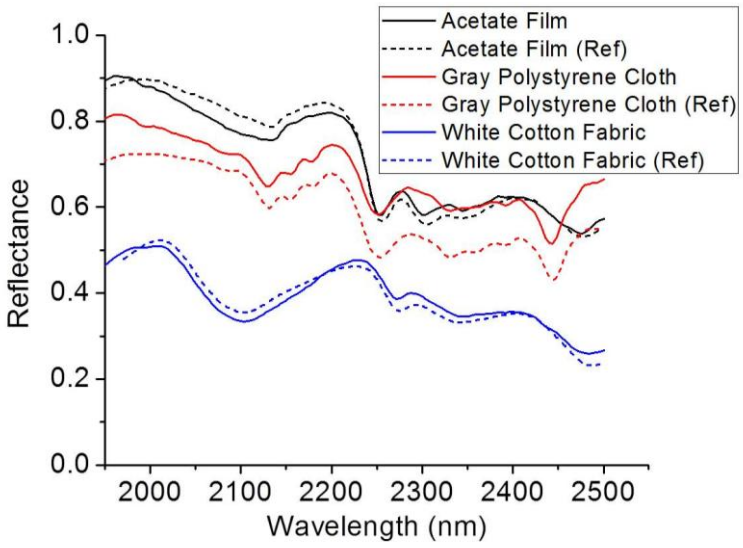


*Fig.5 8. Diffuse spectral reflectance measurements of various samples using the SC laser (solid) and reference measurements performed using a lamp.*

## 4. Discussion

Power scalability of infrared laser sources is becoming a topic of wide interest due to its potential use in a number of applications. The results presented in this chapter indicate that MI initiated SC architectures provide a truly scalable system. As we see from section 3, the spectral extent, beam quality and output variability are all seen to remain fairly constant with power scaling from 5 to 25.7.W. The beam quality is observed to be nearly diffraction limited with an $M^2 < 1.2$ with power scaling as seen in Fig. 5.6. The output stability measurements show a radiometric variability of < 0.8% across the entire spectrum and it remains so with power scaling all the way up to 25.7W.

Although we have demonstrated power scalability up to 25.7W, which is limited by our available pump power, the average SC output power should be further scalable by increasing the repetition rate and by adding more pump lasers. However, very good thermal management and careful low loss splices will be required as the power is scaled up. Once critical splice point in our system prone to thermal damage and requires good thermal management, is the splice between the combiner and the gain fiber, where ~112W of 793 nm pump is coupled into the gain fiber from the combiner. For example, in our initial power scaling attempt, the heat sinking at this splice point proved inadequate at ~85W of 793 nm pump power and lead to significant thermal damage.

Figure 5.9a shows a close up image of the fiber after damage and shows that the fiber jacket is severely damaged. A study of the thermal damage threshold for the fiber jacket was performed by heating the fiber on a hot plate at various temperatures from 100 to 200 deg C. Figure 5.9b shows a comparison of the fiber jacket heated to 150 and 200 deg C, respectively for an hour. No evidence of damage was observed at ~100 deg C. The browning of the jacket from the thermal damage is evident starting at about 150 deg. Thus, for the 25/400/550 mm core/cladding/jacket diameter fibers used in our system, we maintain the temperature <~150 deg C. The temperature is monitored using an infrared thermal viewer and the fiber temperature is always kept < ~120 deg C. Another critical point in the fiber prone to thermal damage is the final fiber endpoint, due to the high intensity at the small core and possible back reflections from the end face into the jacket that could damage the fiber jacket itself. One possible solution for the end face is to use an end-cap, where a small length of a large diameter core fiber is spliced on to the output to lower the intensity at the fiber end face. The maximum average power handling capability of the fiber may be limited to when the temperature of the fiber core rises close to its melting point. Using the formula in [15], we estimate the average power handling limit of the 25/400/550 μm (core/cladding/buffer diameter) fiber used in our system to be >100W. The data presented in this paper suggests that the spectrum, near diffraction limited beam quality and low output variability should still be maintained with power scaling.

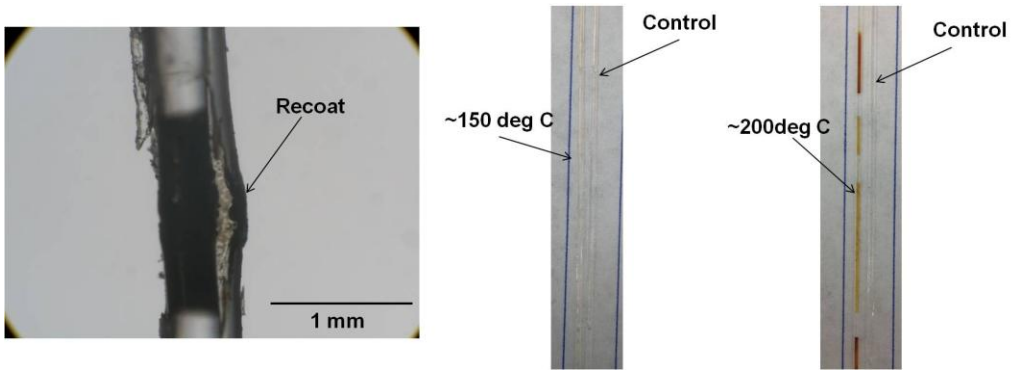


*Fig. 5.9. Fiber thermal damage (a) Fiber jacket/recoat is clearly burnt due to lack of good thermal management. (b) Thermal study of the fiber used in our system show a slight browning at ~150 deg C and clear damage at ~200 deg C.*

Since the SC spectral extent is determined by the peak power, it should be possible to obtain a flatter spectrum by increasing the peak power, which should lead to further pump depletion and push the spectrum out further, until the additional generated spectrum is consumed by the loss edge, which in fused silica is ~ 2.5 μm. However, the spectral flatness in this case comes at the cost of lower SC efficiency, since any additional spectrum generated beyond the loss edge is absorbed by the fiber and does not contribute to the final output power. We observe that the spectrum gets flatter as the peak power is increased, which is done by reducing the repetition rate and keeping the pulse width and average power approximately the same at ~25 W. Figure 5.10 shows that the spectral flatness is improved by ~2 dB as the peak power (calculated as the average power x duty cycle) is increased from 20 kW to 27.5W. Further increase in peak power is limited by the available pump power and possible damage concerns to the system components (combiner, mode field adapter, etc).

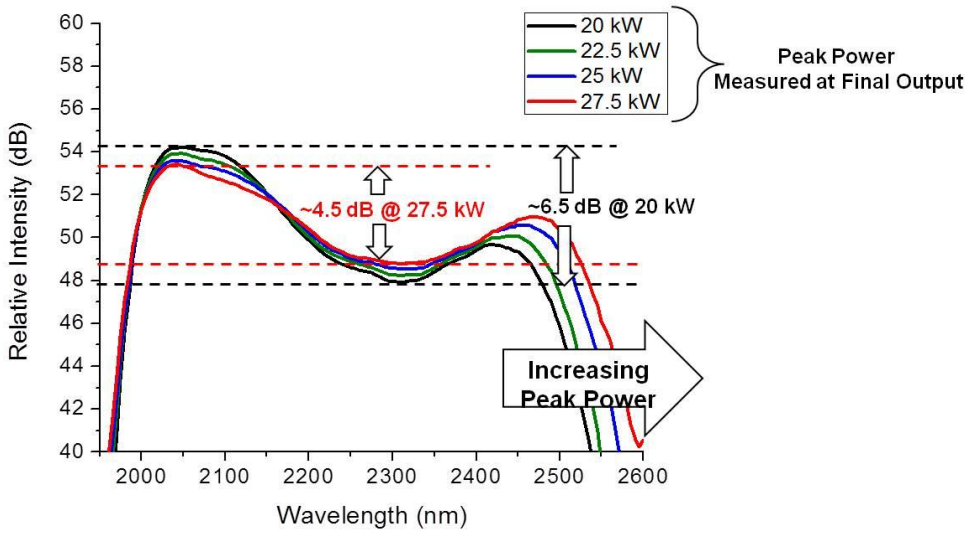


*Fig.5.10. Spectral data showing that the spectral flatness can be improved by increasing the output peak power.*

As a potential application of the developed SC laser, the SC laser has also been used to perform reflectance spectroscopy of various samples. As the results in Fig.5.8 show, the spectral features for the various samples obtained using the SC laser are in good agreement with those obtained using a conventional halogen lamp. In order for applications such as remote explosive detection and spectroscopy to be useful and

practical, measurements need to be performed at large distances and quicker speeds. In such cases, a high average power is required to provide the necessary SNR and system sensitivity. In addition to the high power, the near diffraction limited beam quality and the low output variability are particularly useful features for long distance applications such as remote sensing and hyperspectral imaging.

## 5. Summary

In summary, we demonstrate a truly scalable 25.7W SC laser with the highest spectral density (>12dBm/nm) reported to date in the SWIR band from ~2-2.5 μm wavelength region using an all-fiber platform. The spectrum, beam quality and output stability are studied and show that the SC laser maintains a near constant spectral output, has a near-diffraction limited beam with an $M^2$<1.2 and a radiometric variability of <0.8% across the entire spectrum, as the power is scaled from 5 to 25.7 W. Thus, a truly power scalable SC laser system is presented, where the spectrum, beam quality and output stability are seen to be approximately the same with power scaling. The high average power, near diffraction limited beam quality, low output variability and the spectral reflectance measurements presented here, show that the SC laser can potentially be used as an active illumination source in the SWIR wavelengths for various long distance applications , such as active remote sensing.

## References


1. C. R. Howle, D. J. M. Stothard, C. F. Rae, M. Ross, B. S. Truscott, C. D. Dyer, and M. H. Dunn, "Active hyperspectral imaging system for the detection of liquids," in *Proc. SPIE 6954*, (2008), p. 69540L
2. G. A. Shaw and H.-h. K. Burke, "Spectral Imaging for Remote Sensing," Lincoln Laboratory Journal **14**, 3-28 (2003).
3. B. A. Cumberland, J. C. Travers, S. V. Popov, and J. R. Taylor, "29 W High power CW supercontinuum source," Opt. Express **16**, 5954-5962 (2008).
4. K. K. Chen, S.-u. Alam, J. H. V. Price, J. R. Hayes, D. Lin, A. Malinowski, C. Codemard, D. Ghosh, M. Pal, S. K. Bhadra, and D. J. Richardson, "Picosecond fiber MOPA pumped supercontinuum source with 39 W output power," Opt. Express **18**, 5426-5432 (2010).
5. X. Hu, W. Zhang, Z. Yang, Y. Wang, W. Zhao, X. Li, H. Wang, C. Li, and D. Shen, "High average power, strictly all-fiber supercontinuum source with good beam quality," Opt. Lett **36**, 2659-2662 (2011).
6. R. Song, J. Hou, S. Chen, W. Yang, and Q. Lu, "High power supercontinuum generation in a nonlinear ytterbium-doped fiber amplifier," Opt. Lett **37**, 1529-1531 (2012).
7. J. C. Travers, "High average power supercontinuum sources," Pramana-Journal of physics **75**, 769-785 (2010).
8. C. Larsen, D. Noordegraaf, P. M. W. Skovgaard, K. P. Hansen, K. E. Mattsson, and O. Bang, "Gain-switched CW fiber laser for improved supercontinuum generation in a PCF," Opt. Express **19**, 14883-14891 (2011).
9. O. P. Kulkarni, V. V. Alexander, M. Kumar, Michael J. Freeman, † Mohammed N. Islam,1,2,§, and J. Fred L. Terry, 1 Manickam Neelakandan,3 and Allan Chan3, "Supercontinuum generation from ~1.9 to 4:5 μm in ZBLAN fiber with high average power generation beyond 3:8 μm using a thulium-doped fiber amplifier," J. Opt. Soc. Am. B **28**, 2486-2498 (2011).
10. J. Swiderski and M. Michalska, "Mid-infrared supercontinuum generation in a single-mode thulium-doped fiber amplifier," Laser Phys. Lett **10**, 035105 (2013).
11. D. Buccoliero, H. Steffensen, O. Bang, H. Ebendorff-Heidepriem, and T. M. Monro, "Thulium pumped high power supercontinuum in loss-determined optimum lengths of tellurite photonic crystal fiber," Appl. Phys. Lett **97**, 061106 (2010).
12. W. Q. Yang, B. Zhang, J. Hou, R. Xiao, Z. F. Jiang, and Z. J. Liu, "Mid-IR supercontinuum generation in Tm/Ho codoped fiber amplifier," Laser Phys. Lett **10**, 055107 (2013).
13. J. Geng, Q. Wang, and S. Jiang, "High-spectral-flatness mid-infrared supercontinuum generated from a Tm-doped fiber amplifier," Appl. Opt **51**, 834-840 (2012).
14. M. Faucher and Y. K. Lize, "Mode Field Adaptation for High Power Fiber Lasers," in *in Conference on Lasers and Electro-Optics/Quantum Electronics and Laser Science Conference and Photonic Applications Systems Technologies, paper CFI7.*, (2007).

15. C. Xia, Z. Xu, M. N. Islam, J. Fred L. Terry, M. J. Freeman, A. Zakel, and J. Mauricio, "10.5 W Time-Averaged Power Mid-IR Supercontinuum Generation Extending Beyond 4 μm With Direct Pulse Pattern Modulation," IEEE J. Sel. Top. Quant. Electron **15**, 422-434 (2009).

# Chapter VI

# Surface Roughness Measurement of Flat and Curved Machined Metal Parts Using a Near Infrared Super-Continuum Laser

## 1. Introduction

The measurement of surface roughness and other statistical properties of surfaces are important for a wide range of applications in various industries. For example, in the semiconductor industry, the reliability and stability of thin film components depend in large part on the smoothness of substrates on which they are deposited [1]. The data storage capacity on a surface is also a function of the surface roughness [2]. In other industries like automotive and machining, surface roughness plays an important role in determining friction, lubrication parameters, energy transfer etc. Parts which are finished using lapping or polishing, commonly have surface roughness values in the 0.05 – 0.4 μm range [3]. Two important examples of such polished parts are crankshaft and camshaft journals for internal combustion engines. The surface roughness of crankshaft and camshaft journals and bearings is one of the factors that controls friction and influences the performance and fuel economy of engines [4, 5]. Friction from valve trains, crankshafts, transmission and gears accounts for about 16% of the energy consumption in an engine. Improvements in the tribological performance of engines can provide a variety of benefits such as reduced fuel and oil consumption, increased power output, reduction in harmful emissions and improved durability and reliability of engines [5].

Currently, there is a need in the industry for in-line monitoring of surface roughness in the production environment. Continuous in-line monitoring of surface roughness can detect changes of roughness and other defects on the production line and thus could help to prevent catastrophic failures before they happen. Besides, as the demand for higher quality has increased, surface roughness has become increasingly important in ensuring the quality of parts and products and to achieve better manufacturing control [6].

Current technologies used to measure surface roughness can be grouped into contact based or non-contact based techniques. The mechanical stylus based profilometer is the most common contact based technique used to measure roughness of machined metal parts. This method, however is limited by several factors, including the stylus tip radius [7], the lay of the surface, sample curvature etc. Common non-contact techniques include laser or white-light interferometery, angle resolved light scattering at a fixed wavelength, and specular reflectance vs. wavelength at a fixed angle of incidence [2, 8-14]. Most of these techniques are not very practical for inline measurements, especially for curved surfaces or at large stand-off distances. For instance; interferometery is primarily limited by the working distance and the curvature of samples, where most of the light is reflected away from the detector. Angle resolved scattering techniques have to deal with issues of changing area of illumination with incident angle, which varies according to the cosine of the incident angle to the lowest order, and possible shadowing and multiple scattering effects at large angles of incidence. On the other hand, the specular reflectance vs. wavelength at a fixed angle of incidence approach has advantages that include a constant area of illumination/data collection and the potential for high measurement speed since the sample and detector are all in a fixed position.

The wavelength dependence of specularly reflected light has been extensively explored for roughness measurements. The visible wavelengths have been most commonly used for these measurements due, at least in part, to the availability and relatively low cost of high brightness sources and high sensitivity detectors. However, there are two main factors to consider for roughness measurements of polished metals using the visible region; a) the large angle of incidence required for the reflectance measurements and b) the wavelength signature of the reference that has to be accounted for, in order to make accurate roughness measurements. Hensler and Tavassoly have

shown roughness measurements of flat surfaces from the wavelength dependence of specularly reflected light, using a Xenon or halogen lamp from ~450-800 nm [13, 14]. These measurements had to be done at oblique angles of incidence (~70° [13] and ~88° [14] measured from normal), since the surface irregularities are comparable to the visible wavelengths making the amount of light which is specularly reflected, quite small at lower angles of incidence. Roughness measurements from light scattering at large angles of incidence and scattering are more susceptible to possible shadowing and multiple scattering effects that could affect the reliability of the measurements [9, 15-17]. On the other hand, at lower angles of incidence, reflectance measurements of these surfaces in the visible region would depend not only on the surface roughness, but also on other aspects of the surface such as the root mean square slope etc. If longer wavelengths are used for the measurement of such surfaces, the characteristics of the surface besides roughness become unimportant (at lower angles of incidence) and specular reflectance measurements at these low angles of incidence can provide a simple and effective method for surface roughness measurements [18]. For the common roughness range of polished or lapped parts, low incident angle measurements would then require the use of infrared (IR) wavelengths.

The wavelength dependence of the reference used is another factor to consider when performing specular reflectance vs. wavelength measurements. Ideally, a smooth surface of the same metal composition as the sample should be used as the reference. This ensures that features, besides the surface roughness of the sample of interest are removed by the normalization process. A more subtle, but equally important advantage of the use of near IR and longer wavelengths for metal surface roughness measurements is the fact, that most metals have nearly flat, essentially featureless reflectance vs. wavelength behavior for these longer wavelengths. For example, gold has a reflectance of ~97-99% for wavelengths >1μm. In the visible-near UV range (VIS-NUV), the reflectance vs. wavelength of metals shows much stronger variation and structure. The shape (structure) in the VIS-NUV is influenced by changes in the metal crystal structure (including grain size and/or surface damage) and by metal alloy compositions. There are also other issues such as poor reference preparation [19] and higher sensitivity of the reflectance in the visible wavelengths to layers created by the surface oxidation of the

sample or thin film contaminates, etc. Thus, there are multiple possible sources of error in extracting surface roughness values from metals using VIS-NUV measurements. Since the reflectance signature for smooth metal surfaces in the near IR and beyond is fairly flat, the reference reflectance used does not affect the slope measurements from which the roughness values are extracted. Thus, we can use a single reference (gold mirror for example) and eliminate the need for preparing a highly polished reference sample of the material under test. This also substantially reduces the possibilities for systematic errors and is more practical in an industry setting where the exact composition of the sample, alloys for example, may not be known. Thus, the use of near IR wavelengths and beyond allows the surface roughness measurements of machined metal parts to be performed at low angles of incidence and at the same time, eliminates the requirement to know the exact reflectance vs. wavelength for an ideally smooth reference of the metal under test. The recent development of IR broadband super-continuum (SC) lasers is a key enabler for surface roughness measurements of metals at low angles of incidence, using the same reference material (such as a gold mirror) for all measured samples. In addition, the high average power and the ability to easily collimate and focus the SC laser enables roughness measurements, especially of curved surfaces, at large stand-off distances.

In this chapter, I present a non-contact, potentially high-speed system to accurately measure the root mean square (RMS) surface roughness ($\sigma$) of flat and curved machined parts in the range of ~0.05 to 0.35 μm. This range of roughness values covered by our system is important for a wide range of mechanical applications in the automotive industry including the tribological properties of automotive engine components and is within the roughness range of polished crankshaft journals. First, I present the system setup used to perform the surface roughness measurements followed by the Beckmann-Kirchhoff (BK) theory and method used for extracting the roughness values from the specularly reflected light. The system uses a relatively simple, compact, all fiber based near IR super-continuum (SC) laser source [20] and extracts the roughness from the slope of the reflectance vs. wavelength curve, across the wavelength range from, 1.2 to 2 μm. Next, in section 4, I show experimental results validating the use of a gold mirror as a reference for surface roughness measurements of metals, and provide the criteria used to choose the appropriate wavelength bandwidth and incident angle for performing accurate

measurements. Roughness measurements for flat samples using the SC laser are then presented. In the following section, I present the surface roughness results of cylindrical crankshaft journals measured at 45 deg incidence, again, using a gold mirror as the reference. All roughness measurements using the SC laser are performed at a working distance from sample to detector of greater than ~0.8 m. The roughness values for all samples measured using our system are also compared to measurements performed using conventional instruments, such as the stylus based profilometer and the white light interferometer and shown to be in good agreement. An example for a potential application, where the system is used to sort good crankshafts from those not up to the required roughness specifications is also shown in this section. Finally, I discuss the data presented, with theory, limitations of the system and the scope for improvements in the discussion section before summarizing the results.

## 2. Experimental Setup and Method

The optical layout of the surface roughness measurement system, using the wavelength dependence of the reflected light is illustrated in Fig. 6.1. The light source used in the setup is an SC laser with an average power of ~ 20 mW, from 1.2 to 2.0 μm. The light from the SC is focused into a grating monochromator and the output is collimated using a lens. The collimated light is sent through a polarizer so that the incident light is polarized to be in accordance with the BK model, that we use to extract the roughness and is discussed in more detail in section 3. We use a dual beam approach to minimize any effects of source fluctuations, whereby the light is split into two arms: the sample arm and the reference arm. The reference arm consists of a gold mirror and the reflected light is captured by an InGaAs detector, Det1. The light in the sample arm is collimated for the flat samples and focused for the crankshaft journals to minimize the angular divergence of the reflected light. The beam diameter incident on the flat samples and the journals are about 2 mm and 350 μm, respectively. In the case of crank journals, the reflected light from the journal is again collimated using a lens. A combination of circular and slit apertures is used to spatially filter out the non specular components from the reflected light. This is done by adjusting the apertures to capture the $1/e^2$ intensity or about 86.5% of the power reflected from a gold mirror, when placed in the sample arm. The specular

component versus wavelength is then captured by an InGaAs detector, Det2. The data is then acquired using a standard lock-in amplifier.

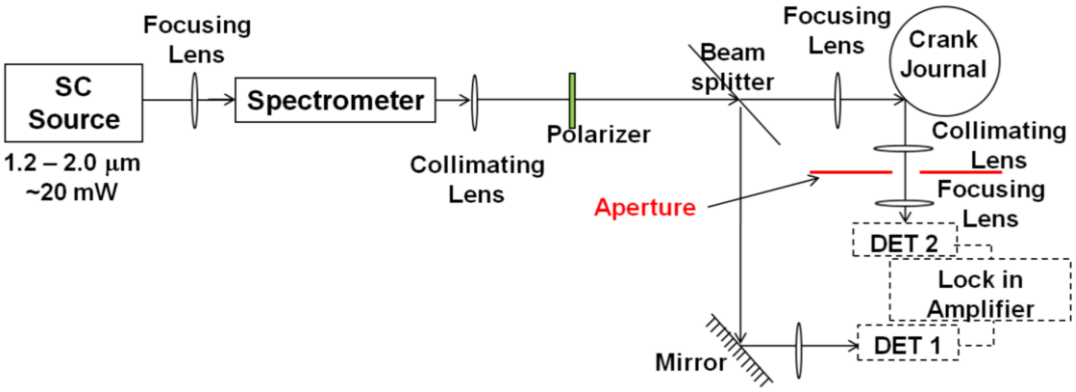


*Fig. 6.1. Optical layout of the surface roughness measurement setup for crankshaft journal measurements.*

For the experimental results presented in this paper, the monochromator slit settings are 100 μm and yield a nominal spectral resolution of ~0.5 nm. The lock-in time constant is 300 ms. We collected ~80 wavelength samples evenly spaced between 1.2 – 2.0 μm and a typical measurement time/spot is ~120 seconds. The measurements were performed only till 2.0 μm due to the detector cutoff at about 2.2 μm. For in-line industrial applications that require high speed measurements, an appropriate spectrometer/array detector could replace the scanning monochromator arrangement.

In our experiments, the measured sample reflectance is normalized to the reference as shown below:

$$\frac{R_{sample}(\lambda)}{R_0(\lambda)} = \left(\frac{S_{meas,sample}(\lambda)}{S_{meas,ref}(\lambda)}\right) \div \left(\frac{S_{meas,ref\ in\ sample\ position}(\lambda)}{S_{meas,ref}(\lambda)}\right) \qquad (1)$$

Where $R_{sample}$ and $R_0$ are the reflectance of the sample and the reference respectively, in the specular direction. Similarly $S_{meas,sample}$ and $S_{meas,ref}$ are the measured signal in the specular direction at the lock-in from the sample under test and the reference respectively. This method of normalization is followed in order to correct for intensity variations vs. time and wavelength for the entire optical system.

## 3. Theory and Data Analysis

To extract surface roughness values from our measurements, we have followed the scattering model outlined by Beckman-Kirchhoff (BK) [21]. It is assumed that all the surfaces considered have an isotropic random roughness and that the elements of the surface height z(x,y) occur with a Gaussian probability distribution $W(z)=\frac{1}{\sigma\sqrt{2\pi}}\exp\left[-\frac{z^2}{2\sigma^2}\right]$, centered about the plane <z>=0. σ is the RMS deviation of the vertical roughness of the surface and is commonly known in the industry as $R_q$. The surface is further described by the autocorrelation coefficient, C (τ) = exp ($-\tau^2/T^2$), where T is the correlation length related to roughness density on the horizontal scale. The assumption in the BK model that the radii of the curvature of the surface features be greater than the incident wavelength is equivalent to requiring that T>>λ [13].

With the above assumptions, Beckmann obtained the following expression for $I_s$, the ratio of the light intensity specularly reflected from a rough surface ($I_{sample,specular}$) relative to that reflected from a smooth surface($I_0$) of the same material composition [13, 21]:

$$I_s=\frac{I_{sample,specular}}{I_0}=\frac{R_{sample}}{R_0}=\exp\left[-\left(\frac{4\pi\sigma\cos(\theta_i)}{\lambda}\right)^2\right]=\exp(-g) \qquad (2)$$

Where $\theta_i$ is the angle of incidence measured from the normal and $\lambda$ is the wavelength of the incident light.

The corresponding diffuse component of the scattered light obtained from theory is given by the following expression [21, 22].

$$\frac{I_{sample,diffuse}}{I_0}=\frac{\pi T^2F^2}{A\exp(g)}\sum_{m=1}^{\infty}\frac{g^m}{m!m}\exp\left(-\frac{V^2{}_{xy}T^2}{4m}\right) \qquad (3)$$

$$F=\frac{1+\cos\theta_i\cos\theta_s-\sin\theta_i\sin\theta_s\cos\phi_s}{\cos\theta_i(\cos\theta_i+\cos\theta_s)} \qquad (4)$$

Where $V_x = k(\sin\theta_i - \sin\theta_s \cos\phi_s)$, $V_y = -k(\sin\theta_s \sin\phi_s)$, $V_{xy}^2 = V_x^2 + V_y^2$ , $\theta_s$ and $\phi_s$ are the angle of reflection and azimuth angle with respect to the surface normal in the scattering direction.

If the receiving optics is set so that the receiving angle equals the angle of incidence (Snell's law), then the measured intensity will be composed of the specular component (equation 2) plus the fraction of the diffuse component (equation 3) that is scattered into the angle of acceptance of the receiver around the Snell's law direction. It has been shown that for slightly rough surfaces, where g << 1, this collected diffuse component is negligible [12, 15]. Also, if the measurement area is large compared to the square of correlation length (A >> $T^2$), which is the case for most measurements; the contribution of the diffuse component in the specular direction is further reduced. Under these conditions, energy information from the specular direction that is lost into diffuse scattering is easily extracted by looking at the spectral dependence of the reduction of the specular signal. Thus, if the reflectance measurements are made at sufficiently long wavelengths or large incidence angles such that g << 1, σ can be calculated directly from the measured reflectance in the specular direction using the following equation obtained from equation (2).

$$\ln\left(I_s\right) = \ln\left(\frac{R_{sample}}{R_0}\right) = -g = -\left(4\pi\sigma\cos\left(\theta_i\right)\right)^2\left(\frac{1}{\lambda^2}\right) \qquad (5)$$

This is now a linear equation for $\ln\left(I_s\right)$ in terms of $1/\lambda^2$ where the slope depends directly on the surface roughness parameter σ.

It is worth noting that from equation 5, the reference ($R_0$) used for the measurements can introduce three main kinds of errors that could affect the accuracy of the slope and hence the extracted σ values. First, it is possible that $R_0$ has a constant offset in terms of λ due to minor misalignments in the system. However, this can be easily corrected by adding a constant scaling factor to equation 5 and so, does not affect the fitting of the slope of the normalized reflectance curve and the extracted σ value. This is effectively equivalent to fitting only the slope of the $\ln\left(I_s\right)$ vs. $\lambda^{-2}$ curve and the value of the scaling factor is not used in the surface roughness extraction. Next, if the reference used had some roughness to begin with, then the roughness value obtained from

the normalized spectrum will be less than the actual roughness of the sample. The error in this case can be minimized by using a reference as smooth as possible, or of a known roughness value. Finally, if the reference used is not of the same material composition as the sample, the reflectance spectrum of the reference and the sample could be different due to the material properties. The normalized reflectance in this case will not correspond to the actual roughness value of the sample under consideration and will be a major source of error in the measurements. However, this becomes less of an issue in the NIR and beyond and we will show that it is possible to obtain accurate roughness measurements of metal surfaces using a gold mirror as a reference, and that the error in measurements caused by the three factors mentioned above is significantly reduced. This is further discussed in the results section.

All simulation fits in this paper were performed over the wavelength region from 1.2 to 2.0 μm using the Levenberg-Marquardt non-linear least squares algorithm. Since our data was taken at equal intervals of λ, the non-linear fitting algorithm was used, where the raw data ($I_s$ vs. λ) was fitted first to equation 2, which is a non-linear equation for $I_s$ in terms of λ, to extract the roughness value. The Levenberg-Marquardt algorithm is a popular method used for non-linear curve fitting. The results are then plotted on the log scale (ln ($I_s$) vs. $(1/\lambda)^2$) according to equation 5, as it is easier to relate and compare roughness values using a linear slope. We have also calculated and plotted the 95% confidence intervals on all the predicted simulation fits and the corresponding intervals for the extracted roughness values, and seen this to be ≤ ±10 nm of the fitted roughness values across all the samples measured.

## 4. Results

### 4.1 Flat Samples

Two flat cold rolled steel samples with different surface roughness values are used for the flat sample measurements. They are commonly known in the industry as the steel #2b and steel #4 finishes and are designated as Flat A and Flat B, respectively. In both measurements, the incident light is collimated with a beam diameter of ~2mm and the reflectance data is measured in the wavelength range, from 1.2 to 2.0 μm, in steps of 10

nm. To justify the use of a gold mirror as a reference, this section compares the roughness measurements for both Flats A and B, made using a gold reference with measurements made using a smooth steel reference. The relation between the wavelength bandwidth and incident angle for making accurate measurements is also discussed. Then, the results obtained using the SC laser are compared with other conventional instruments such as the stylus profilometer and the white light interferometer and seen to be in good agreement.

### 4.1.a Justification for Using a Gold Mirror Reference

One of the assumptions used in deriving equation 5, is that the reference spectrum used in the normalization process is of the same material composition as the sample itself. We have used a gold mirror as the reference to normalize the reflectance of all our samples (flat steel samples and crankshaft journals) and to perform the corresponding simulation fits. In order to justify the use of a gold mirror as a reference, we performed two sets of roughness measurements with the flat steel samples. In the first case, the roughness value is measured for both Flat A and Flat B using a gold mirror as the reference and in the second case, a flat steel polished to a mirror finish using a 0.05 μm grit size polishing cloth is used as the reference. Fig. 6.2 shows the reflectance measurements for both Flat A and B normalized to gold and steel mirrors respectively. The dotted lines show the 95 % confidence interval for the fitted y values. For both Flat A and B, the slopes of the two reflectance curves corresponding to gold and steel mirror references are seen to be comparable and the roughness values extracted from the simulation fits are almost identical. The extracted roughness values and the 95% confidence interval for the $\sigma$ value from the reflectance spectrum for Flat A is 0.152 ± 0.010 μm (w/gold reference) and 0.151±0.010 μm (w/steel reference). Similarly the extracted roughness values for Flat B is 0.313 ± 0.005 μm (w/gold reference) and 0.312 ± 0.009 μm (w/steel reference). Fig. 6.2 also clearly shows the relation between the slope of reflectance signatures and their corresponding roughness values i.e. higher slope corresponds to higher roughness values. Thus, we have experimentally shown that the roughness value of metal samples can be measured from the wavelength signature of the reflectance in the IR region using a

gold mirror as a reference, and that a reference of the same metal composition is not required for accurate measurements.

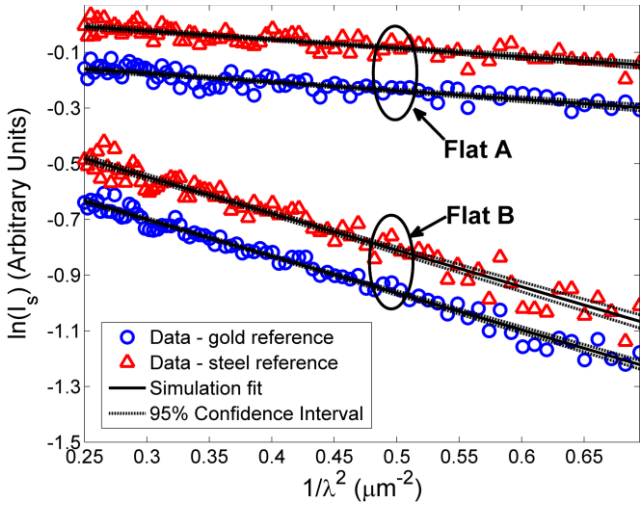


*Fig. 6.2. Comparison of normalized reflectance curves using smooth steel and gold references for both Flat A and B. Extracted roughness values for Flat A are 0.152±0.010 µm (w/gold reference) and 0.151±0.010 µm (w/steel reference). Extracted roughness values for Flat B are 0.313±0.005 µm (w/gold reference) and 0.312±0.009 µm (w/steel reference). Larger slope values correspond to higher surface roughness values.*

The lack of requirement for the same material reference can be explained by the fairly flat reflectance signature of metals, like gold, aluminum etc, in the near infrared wavelengths and beyond. The wavelength shape of the normalized reflectance in the Infrared is then mostly due to the surface features and is more or less independent of the metal property of the reference itself. In principle, the roughness range of interest for crank journals and metal parts can be measured using scattering in the visible region; however, different metals have widely varying reflectance signatures in the visible region. This makes it mandatory to have a reference of the same material or to correct for the wavelength signature of the reference for measurements done in the visible region. The results shown in Fig. 6.2 indicate that operating in the infrared region has the added benefit of having a universal reference, such as a gold mirror, for surface roughness measurements of metals using this technique.

### 4.1.b Choice of Wavelength and Incident Angle

The wavelength range and incident angle are critical factors that determine the range of roughness values that can be measured using the specular reflectance method. In the case of a fixed incident angle, as the wavelength increases, the value of g decreases according

to equation 2, to satisfy the condition g << 1, where the specular component is the dominant part of the total reflectance in the specular direction and equation 5 becomes valid. Similarly, if the wavelength is held constant and the angle of incidence is allowed to increase, g again decreases to << 1, since g is proportional to $\cos(\theta_i)$ and equation 5 will again hold. Thus, in order to extract the surface roughness from the wavelength dependence of the reflected light using equation 5, it is important to choose the appropriate wavelength range and incident angle. Bennett et al showed that it is possible to perform roughness measurements of flat samples from the wavelength signature at a fixed incident angle (normal incidence) by increasing the wavelength range, using a globar source [18]. We show that it is also possible to increase the roughness measurement range by increasing the angle of incidence while keeping the wavelength range constant.

In order to determine the upper range of roughness value that our system was capable of measuring using the wavelengths from 1.2 to 2.0 μm, we performed the reflectance in the specular direction for the roughest sample, Flat B, which is a flat steel sample with an σ value of 0.325 μm, as measured using a stylus profilometer. First, the measurements are done at an incident angle of 45°. In this case, the value of g is calculated to lie between 2 and 5.6 across the wavelength region, from 1.2 to 2.0 μm. Thus, the assumption that g << 1 used to derive equation 5 is no longer valid. This is made clear in Fig. 6.3, where we can see that the reflectance vs. wavelength curve is not a straight line according to equation 5 and a clear inflection point is evident in the curve as we move closer to lower wavelengths. The deviation of the normalized specular reflectance signature from a straight line at lower wavelengths can be explained by the diffuse scatter, which now takes over as the dominant contributor to the reflection in the specular direction. In order to move towards g << 1, the incident angle is increased to 73°. Fig. 6.4 shows the reflectance vs. wavelength curve for this case where the curve is now a straight line as expected from equation 5 and the roughness value of 0.313 μm extracted from the slope is comparable to the profilometer value of 0.325 μm. In this case, the value of g is calculated to lie between 0.35 and 0.96. Thus, the roughness measurements presented here show that the wavelength bandwidth and incident angle parameters are related and that it is important to choose the appropriate wavelength band

and incident angle for accurate roughness measurements. We have experimentally seen that the roughness value obtained from the wavelength signature of the specularly reflected intensity using this technique is valid up to g < 1. All of our wavelength measurements have been made to conform to this requirement of g < 1. This was achieved by performing all measurements using a wavelength range from 1.2 to 2.0 μm at an incident angle of 45°, except for the flat samples which were done at 73°.

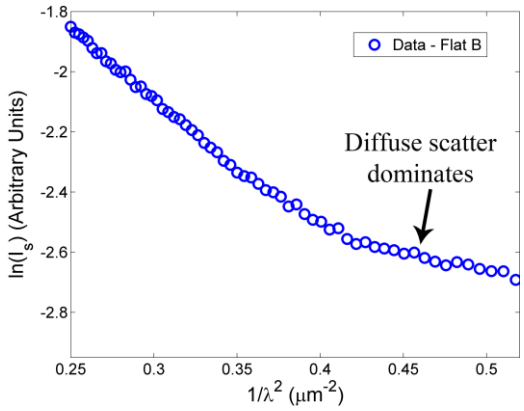


*Fig. 6.3. Normalized reflectance spectrum of Flat B at 45° where* $2 \le g \le 5.6$. *The slope of the normalized reflectance is not a straight line and begins to curve at lower wavelengths where the diffuse scattering component begins to dominate in the specular direction. This will result in an erroneous roughness value.*

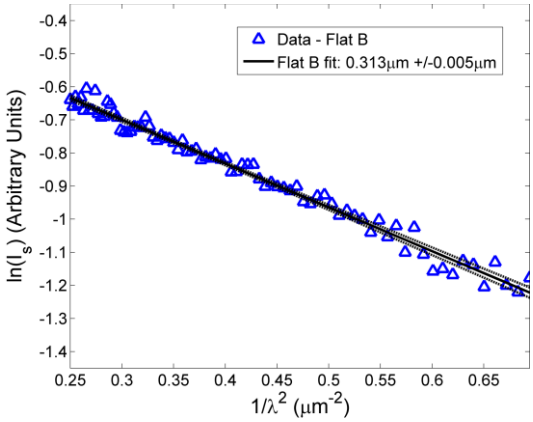


*Fig. 6.4. Normalized reflectance spectrum of Flat B at 73° where* $0.35 \le g \le 0.96$. *The reflectance curve is once again a straight line as expected from the BK model and the correct roughness value can be extracted from the slope of this line. The extracted roughness value is seen to be in good agreement with the value measured using a stylus profilometer.*

### 4.1.c Comparison of SC Values with Other Techniques

The roughness values obtained using the SC laser are also compared to the measurements made using a mechanical stylus based profilometer (Talysurf) and a white

light interferometer (WYKO). For each technique, the roughness values are measured at three random points on the samples and their average value along with the standard deviation (in parenthesis) is shown in table 1. We can see from table 1 that the σ values obtained using the SC laser are in close agreement to the values obtained using the stylus profilometer as well as the white light interferometer.

*Table 6.1. Comparison of flat sample RMS roughness values*

| Sample | Super-continuum (μm) | White Light Interferometer (μm) | Stylus (μm) |
|---|---|---|---|
| Flat A | 0.148 (0.005) | 0.146 (0.004) | 0.136 (0.005) |
| Flat B | 0.324 (0.018) | 0.330 (0.026) | 0.326 (0.020) |

## 4.2 Crankshaft journal measurements

After verifying the roughness measurements for the flat samples, we then used the system to perform roughness measurements on cylindrical crankshaft journals. A typical crankshaft journal used in our measurements is shown in Fig. 6.5. All crankshafts are obtained from various automobile vendors and the journals are designated as Cranks A, B, C, D and E respectively. Crank A is polished with a rough polishing tape and made smoother by using a finish polishing tape. Crank B is polished using a rough polishing tape only. Both Cranks A and B looked the same with visual inspection. Crank C is polished to an unknown specification and Crank D is not polished at all. Finally, Crank E is polished starting with Crank C and then polishing it close to a mirror finish with a 1 μm grit polishing cloth. Both Cranks D and E are visually distinct from all the other crank samples. Cranks A and C were both provided as examples of crankshaft journals with acceptable roughness values by the vendors.


*Fig. 6.5. Example of a crankshaft journal*

### 4.2.a SC Laser Measurements

The roughness measurements on the cylindrical journals are performed using the SC laser spanning the wavelength region, from 1.2 to 2.0 μm, in steps of 10 nm. In this case, the incident light is focused on to the journal in order to limit the angular spread of the reflected light. Also, focusing the light to a small spot on to the curved surface allows for a quasi-flat surface approximation, similar to the case for flat samples. The laser spot diameter (using knife-edge measurements) on the journals is measured to be about 350 μm. A 10 cm focal length lens is used, both to focus the ~ 2 mm collimated light on to the journal and to re-collimate the reflected light from the journal. The incident angle used is 45°.

Figure 6.6 shows an example for the measured reflectance signal, from 1.2 to 2.0 μm of the reference material (gold mirror) and the crankshaft journal Crank B. Figure 6.7 shows the normalized reflectance spectrum both for Crank B and Crank C. The simulation fits, using the BK model and the corresponding extracted roughness values are also shown in Fig. 6.7. The RMS roughness values and the corresponding 95% confidence interval for Crank B and Crank C is measured to be 0.111 ± 0.003μm and 0.086±0.004 μm respectively. The slope difference between the two roughness values is also evident in Fig. 6.7, where larger slope corresponds to a higher roughness value.

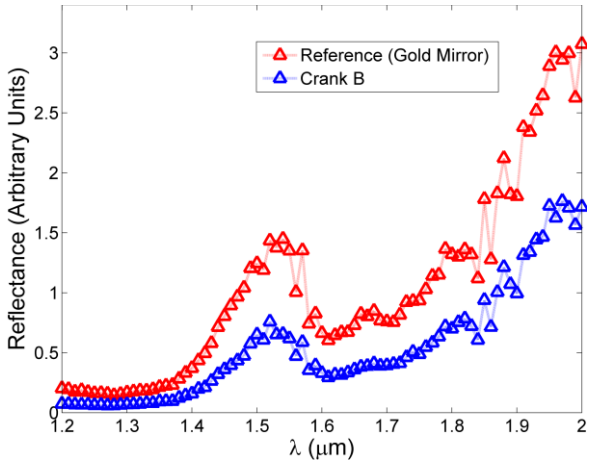


*Fig. 6.6. Measured signal for the reference (gold mirror) and sample (crank B) as measured by the two detectors DET 1and DET 2 respectively*

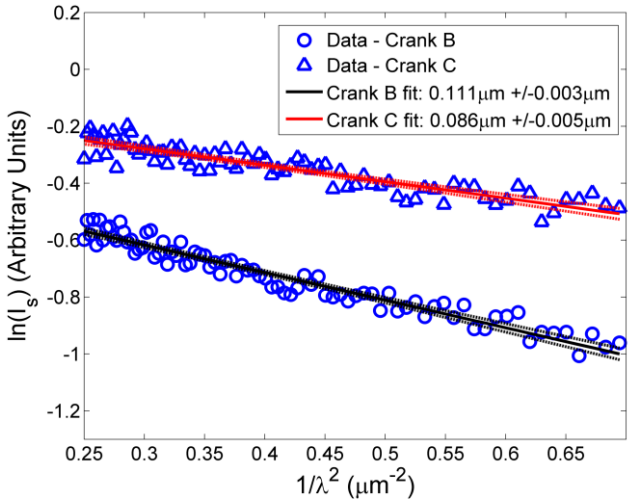


*Fig. 6.7. Normalized reflectance spectrum and the extracted roughness values for cylindrical crank journals Crank B and Crank C respectively. Dotted lines represent the 95% confidence interval for the fitted y-axis values.*

The angle of incidence parameter used for the simulation fit is the half angle between the beam centers of the collimated beam sections before the focusing and after the collimation lens respectively. Since the light is focused on to the journals, there is a range of incidence angles involved in a given measurement. Therefore, it is important to characterize the sensitivity of the extracted roughness value to the incident angle parameter used in the simulation fitting algorithm. Large focal lengths (10 cm) used in our measurement setup will help to narrow down the range of incidence angles involved in a measurement. This would then allow us to apply the paraxial approximation for the incident angle parameter used in the simulations. In order to quantify any possible error

in the measured incident angle, we calculated the sensitivity of the extracted roughness value for Cranks C and E to the angle of incidence parameter ($\pm 1^{\circ}$ change) used in the specular reflectance simulation fits to be about $\leq \pm 2.0\%$ of the roughness value extracted, when fitted with the actual incident angle that was measured.

We also performed static and dynamic repeatability measurements with the journals using the system. Crank C is used for the dynamic repeatability tests, where the crank journal is cycled in and out of the system after each measurement. Measurements are performed by loading and unloading the crank journal to about the same position for ten times. The average measured $\sigma$ value is ~0.091 μm and the standard deviation is ~ 0.002 μm. Crank B is chosen for the static repeatability tests, where ten consecutive measurements are made at one site without moving the sample. The average measured $\sigma$ value in this case is ~0.102 μm and the standard deviation of the measured $\sigma$ values is ~0.001 μm.

### 4.2.b Comparison of SC Values with Other Techniques

The roughness values of the crank journals obtained using the SC laser are compared against other standard techniques such as the mechanical stylus based profilometer (Talysurf) and the white light interferometer (WYKO). Table 2 shows a comparison of the roughness values for all the crankshaft journals obtained using the three different methods. For each sample, the roughness measurements are performed at three random points on the sample and the average value and standard deviation is noted in the table. We were not able to measure Crank E using the white light interferometer, since the roughness value is below the measurement range using the available settings. The roughness value of Crank D is above the measurement range of our system.

*Table 6 2. Comparison of crank journal RMS roughness values*

| Sample | Super-continuum (μm) | White Light Interferometer (μm) | Stylus (μm) |
|---|---|---|---|
| Crank A | 0.081(0.004) | 0.091(0.002) | 0.088(0.006) |
| Crank B | 0.109(0.011) | 0.111(0.015) | 0.115(0.014) |
| Crank C | 0.087(0.004) | 0.093(0.008) | 0.087(0.010) |
| Crank D | NA | 0.774(0.045) | 0.757(0.039) |
| Crank E | 0.049(0.003) | NA | 0.047(0.005) |

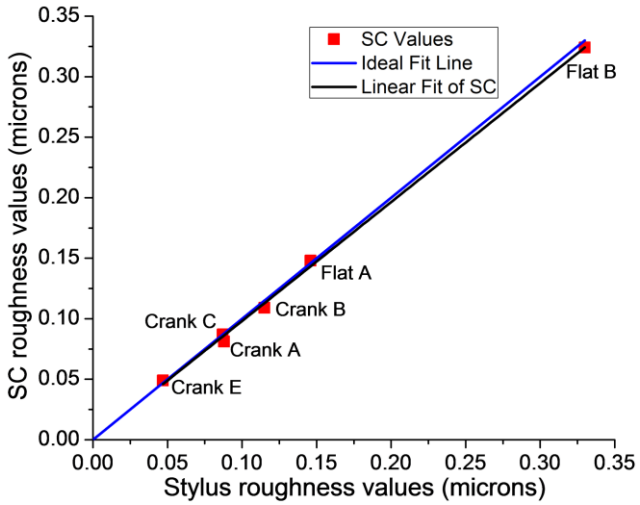


*Fig.6.8. Super-continuum vs. stylus measured roughness values. The SC roughness values are seen to be in good agreement with the values measured using a stylus profilometer.*

Figure 6.8 plots the comparison of roughness values measured with the SC laser to the stylus profilometer values. A linear fit of the SC measured data is performed to compare the roughness values measured using the SC laser to those measured using the stylus profilometer. The best linear fit has a slope of 0.99 and a y intercept of 0.002 µm. An ideal fit would correspond to a slope of 1 and a y intercept of 0, had the values obtained using the two techniques been identical. Table 2 and Fig. 6.8 both show that the RMS roughness values measured using the SC laser are comparable to the values measured using the stylus profilometer and the interferometer. This close agreement shows that there are no significant systematic errors in the SC measurements.

### 4.2.c Detecting Crankshaft Roughness Defects

As a possible application for inline detection of crank journal roughness defects, we used the SC laser system to sort good crank journals from those not polished to specification. Cranks A and B are used for the sorting measurements and were provided by the manufacturer as examples of good and bad crank journals respectively. Crank A was polished first with a rough polishing tape and then smoothened using a finish polishing tape. Crank B skipped the rough polishing stage entirely and was polished only with the finish polishing tape. Polishing should be done in a progressive sequence from a rougher to smoother finish. If a step is missed due to a broken polishing tape or some other issue,

this can lead to surfaces with a higher peak to valley difference translating to a higher RMS roughness value. Figure 6.9 shows the roughness value distribution for ten random points on each of the samples. The average σ value for Crank A and B are measured to be 0.080 μm (std dev = 0.007μm) and 0.100 μm (std dev =0.011 μm) respectively. As we can see from Fig. 6.9, the Crank A roughness distribution is decreasing towards higher roughness values while Crank B roughness distribution is increasing towards higher roughness values reaching a peak between 0.1 and 0.11 μm. The average σ values of cranks in our samples designated as good crank journals by the supplier are about $\leq$0.09 μm. The data in Fig. 6.9 shows that 90 % of the σ values for Crank A lie below 0.09 μm while about 80% of the σ values for Crank B lie above 0.09 μm. Thus, we can conclude that Crank B is rougher than Crank A and is therefore not polished to specification. This could be because of reasons such as a missed polishing step, a broken or worn out polishing tape etc.

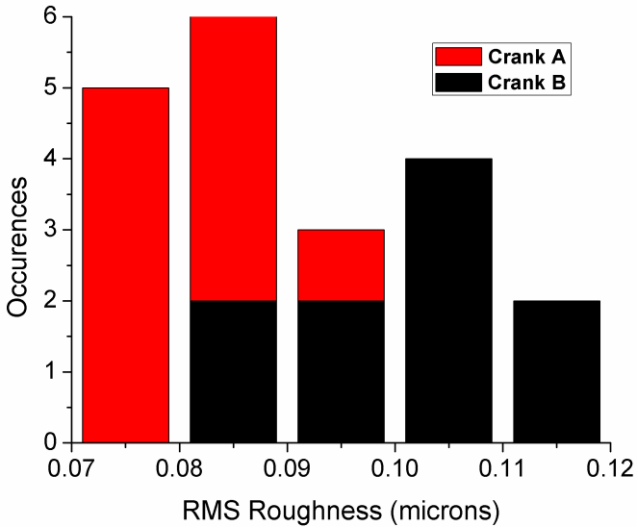


*Fig. 6.9. RMS roughness distributions for Crank A and Crank B. Crank A has a higher roughness distribution towards lower roughness values while Crank B has a higher distribution towards larger surface roughness values. Crank A is specified as a journal with acceptable roughness by the vendor. This data indicates that Crank B has a higher surface roughness value than Crank A and is therefore not polished to specification.*

## 5. Discussion

The theory of scattering of electromagnetic waves from rough surfaces applying the Beckmann-Kirchhoff approximation is outlined. Experimental evidence has also been presented showing the validity of the model to both flat and curved samples. The linear

plots of reflectance vs. wavelength in the specular direction, shown in Figs. 6.2 and 6.7, and the data comparing the roughness values extracted from the wavelength dependence to other standard techniques, as presented in Tables 1 and 2 respectively, show the applicability of eq 5 to make surface roughness measurements in the wavelength and incident angle ranges investigated. Furthermore, the crankshaft journal roughness measurement data shows the validity of equation 5 on curved surfaces, as enabled by the ability to collimate and focus the SC laser easily. We also measured the correlation length, T, using the stylus profilometer for all the samples to be between 7 μm and 14 μm. Thus, we have the condition that $T>\lambda$ rather than $T>>\lambda$ , as assumed in deriving equation 5. However, the data presented in Tables 1 and 2 demonstrate that equation 5 is still applicable for the case $T>\lambda$. Hensler and Ohlidal have also reported the same conclusion in their work on light scatter [13, 23]. The exponential correlation function is also seen to give a better fit to the stylus measured data than the Gaussian correlation function. According to the BK model, the nature of the correlation function plays a negligible role for scattering in the specular direction for slightly rough surfaces [12, 21], and is not seen to affect the roughness measurements for the samples used in our study.

We have also estimated the spatial wavelength bandwidth for the different techniques used to measure the surface roughness. The spatial frequency is calculated as 1/(spatial wavelength). For the stylus profilometer, the lowest spatial wavelength (lateral resolution) is chosen to be 2.5 μm and the largest spatial wavelength (sampling length) is chosen to be 800 μm. Thus, the spatial wavelength bandwidth of the stylus profilometer is 2.5 – 800 μm, which corresponds to a spatial frequency bandwidth of $1.25\times10^{-3}$ – 0.4 $\mu m^{-1}$. The white light interferometer has a lateral resolution of ~1 μm and a sampling length of ~ 100 μm. Thus, the spatial wavelength bandwidth in this case is ~1 – 100 μm, which corresponds to a spatial frequency bandwidth of ~0.01 – 1 $\mu m^{-1}$. For the scattering technique, the lower spatial wavelength limit is approximately the optical wavelength [15, 24], which, in our case is ~1.2 μm. The grating equation can be used to estimate the upper limit of the spatial wavelength, where, a surface can be thought of as being composed of components of sinusoidal height variations, each with different amplitude, spatial frequency and phase. A beam of light incident on the surface is diffracted into

different orders on either side of the specular beam [24, 25]. Since all spatial wavelengths in the area of illumination will contribute to the specular direction, the highest spatial wavelength that contributes in the specular direction is limited only by the illumination beam diameter. For our curved sample experiments, the beam diameter used is ~350 μm. The spatial wavelength bandwidth is then ~1.2 – 350 μm, which corresponds to a spatial frequency bandwidth of ~ $2.86\times10^{-3}$ – 0.83 $\mu m^{-1}$. The fairly good agreement between the different techniques used, would indicate that the samples most likely have spatial features that are in the overlapping region of the spatial frequency bandwidths of the techniques used.

The importance of parameter g and its role in determining the range of wavelengths and incident angles has been shown with an experimental example in Figs. 6.3 and 6.4, where we see that it is possible to extend the roughness measurement range by increasing the incident angle used. Experimental data also indicates that equation 5 is valid under the condition that the parameter g is < 1 rather than g<<1 over most of the wavelength range used. Following this technique, we are able to measure roughness values up to ~0.35 μm at an incident angle of 73°, where the highest value of $\sigma/\lambda$ is calculated to be ~0.29. Vorburger et al have also suggested a $\sigma/\lambda$ regime up to ~ 0.3, where the specular reflected measurements can be used for the roughness measurements [15]. However, very large angles of incidence and scattering may render invalid, some of the assumptions (such as the paraxial or small-angle assumption) used in the BK model, and result in possible shadowing and other scattering effects that can affect the surface measurements of rough surfaces, obtained using the BK model [9, 15-17, 26, 27]. In addition, at grazing incident angles, the beam also becomes difficult to align on the surface [15]. One possible solution to extend the roughness measurement range of surfaces while maintaining a low angle of incidence would be to extend the wavelength region used for the measurements to get g <1. Ideally, in most cases, the measurements would best be done at normal incidence. For the range of roughness values from ~0.05 to 0.35 μm, representative of finished metal surfaces in the automotive industry, this would require a wavelength range of about ~ 0.7 to 4.5 μm. Xia et al have reported SC lasers spanning from 800 nm to 4 μm with a time averaged power of ~10 W [28]. The high

power can also increase the working distance used for the measurements, which could be useful in an inline industry setting.

The data presented in Fig. 6.2 also confirm the validity of using a gold mirror as the reference for roughness measurements of metals and the benefits of performing measurements in the infrared region. It is known that most common metals exhibit strong wavelength dependence in their reflectance signature around the plasma frequency ($\omega_p$) of that metal. The plasma frequency for most common metals is in the visible and UV regions and hence it is important to have a reference of the same metal or to correct for the wavelength dependence of the reference reflectance for measurements performed in the visible wavelengths. Also, the reflectance signature can be affected by anomalous skin effects due to lattice distortion from poor sample preparation [19]. These effects are more pronounced in the visible wavelengths near $\omega_p$ and are small in the near IR and beyond. As $\omega << \omega_p$ which corresponds to the near IR and beyond, the reflectance signature of the common metals are approximately flat. It is this property of metals that enables us to perform roughness measurements in the near IR using a gold mirror as a reference. In addition, it is not always trivial to prepare a smooth reference for every material composition that is used in the industry setting. Smooth gold mirrors, on the other hand are fairly cheap and commercially available. As a possible application suggested in section 4.2.c, where we detect polishing defects in crank journals, this system can be potentially used for inline roughness measurements and process control on the plant floor. One of the added advantages of using an all fiber based SC laser is the ability to design a fiber based sensing head, where the fiber extension would allow the system components to be placed remotely with only the sensing heads on the plant floor, making it easier to integrate this technique into current process monitoring technologies used in the industry with minimum space requirements.

## 6. Summary

In conclusion, we have demonstrated an RMS surface roughness measurement system capable of measuring roughness values in the range of ~0.05 to 0.35 μm, from the slope of the wavelength dependence of reflected light, using a super-continuum laser, from 1.2

to 2 μm. We have used the system to perform surface roughness measurements on flat metal samples with σ values ranging from ~0.14 to 0.33 μm and automobile crankshaft journals at different stages of polishing with σ values ranging from ~0.05 to 0.12 μm. The σ values obtained using the SC laser are compared with those from a stylus based profilometer and a white light interferometer and shown to be in good agreement. Repeatability measurements are also performed on the system and shown to have a standard deviation of $\leq 0.002\mu m$. Performing roughness measurements in the near IR and beyond has added benefits compared to using the visible wavelengths. We have shown that, by performing roughness measurements of metallic surfaces in the near IR, a reference measurement from the same material composition is not required and that a gold mirror can effectively be used as a reference. The longer wavelengths also allow for measurements to be performed at a lower angle of incidence (45° in the case of crank journals), thus reducing possible shadowing and other scattering effects that could affect the accuracy of roughness values measured. We have also discussed the importance of the parameter g in the BK model to be < 1, while choosing the appropriate parameters such as wavelength and incident angle to perform accurate measurements using this technique. As an example for a potential application for inline inspection, we have used the system to detect and sort good crankshaft journals from defective ones not polished to specifications. The SC laser provides the ability to collimate and focus the light, which is critical for roughness measurements of curved surfaces using this technique. We have successfully demonstrated the broadband super-continuum laser as a key enabler for wavelength dependent roughness measurements of flat and curved surfaces with large working distances of greater than 0.8m from the sample to the detector. Finally, we have also discussed how the roughness measurement range and working distance can both be increased by SC laser systems being developed with longer wavelength bandwidths and higher power. The combination of sub-micron roughness measurements at a large working distance along with the capability to measure both flat and curved surfaces, like crankshaft journals, makes the system an attractive tool for inline inspection in the industry.

## References


1. R. M. Anderson and G. W. Neudeck, "Flatness and surface roughness of some common thin film substrate materials," J Vac Sci Technol **8**, 454-457 (1971).
2. J. M. Bennett, "Measurement of the RMS roughness, autocovariance function and other statistical properties of the optical surfaces using a FECO scanning interferometer," App Opt **15**, 2705-2721 (1976).
3. E. P. DeGarmo, J. T. Black, and R. A. Kohser, *Materials and Processes in Manufacturing*, 8 ed. (Prentice-Hall, 1997).
4. S. Adachi, K. Horio, Y. Nakamura, K. Nakano, and A. Tanke, "Development of Toyota 1ZZ-FE Engine," SAE Technical papers 981087 (1998).
5. S. Tung and M. L. McMillan, "Automotive tribology overview of current advances and challenges for the future," Tribology Int **37**, 517-536 (2004).
6. D. Whitehouse, "Surface Metrology," Meas. Sci. Technol. **8**, 955-972 (1997).
7. K. A. O'Donnell, "Effects of finite stylus width in contact Profilometry," App Opt **32**, 4922-4928 (1993).
8. E. L. Church, "The measurement of surface texture and topography by differential light scattering," Wear **57**, 93-105 (1979).
9. J. C. LeBosse, G. Hansali, J. Lopez, and T. Mathia, "Characterization of surface roughness by laser light scattering: specularly scattered intensity measurement," Wear **209**, 328-337 (1997).
10. J. M. Bennett and P. Z. Takacs, "Surface roughness and scattering: papers from the first topical meeting," App Opt **32**, 3333-3334 (1993).
11. J. G. Valliant, M. P. Foley, and J. M. Bennett, "Instrument for on-line monitoring of surface roughness of machined surfaces," Opt Eng **39**, 3247-3254 (2000).
12. D. Kim, K. J. Oh, and C. S. Lim, "Simultaneous measurement of root-mean-square roughness and autocorrelation length by optical method," Part of the SPIE conference on three dimensional imaging, optical metrology, and inspection IV **3520**, 277-283 (1998).
13. D. H. Hensler, "Light scattering from fused polycrystalline aluminum oxide surface," App Opt **11**, 2522-2528 (1972).
14. M. Tavassoly and M. Dashtdar, "Height distribution on a rough plane and specularly diffracted light amplitude are Fourier transform pair," Opt. Commun **281**, 2397-2405 (2008).
15. T. V. Vorburger, E. Marx, and T. R. Lettieri, "Regimes of surface roughness measurable with light scattering," Appl. Opt **32**, 3401-3408 (1993).
16. K. E. Torrance and E. M. Sparrow, "Theory for off-specular reflection from roughned surfaces," J Opt Soc Am **57**, 1105-1114 (1967).
17. J. Caron, J. Lafait, and C. Andraud, "Scalar Kirchhoff's model for light scattering from dielectric random rough surfaces," Opt Commun **207**, 17-28 (2002).
18. H. E. Bennett and J. O. Porteus, "Relation between surface roughness and specular reflectance at normal incidence," J. Opt. Soc. Am **51**, 123-129 (1961).
19. H. E. Bennett, "Reflectance, scattering and anomalous skin effect," in *Encyclopedia of optical engineering*, R. G. Driggers, ed. (Marcel Dekker, New York, 2003), pp. 2349-2357

20. C. Xia, M. Kumar, M.-Y. Cheng, O. P. Kulkarni, M. N. Islam, A. Galvanauskas, F. L. T. Jr, M. J. Freeman, D. A. Nolan, and W. A. Wood, "Supercontinuum generation in silica fibers by amplified nanosecond laser diode pulses," IEEE JOURNAL OF SELECTED TOPICS IN QUANTUM ELECTRONICS **13**, 789-797 (2007).
21. P. Beckmann and A. Spizzichino, *The scattering of electromagnetic waves from rough surfaces* (Pergamon, New York 1963).
22. H. Ragheb and E. Hancock, "Testing new variants of the Beckmann–Kirchhoff model against radiance data," Comput Vis Image Und **102**, 145-168 (2006).
23. I. Ohlidal, K. Navratil, and F. Lukes, "Reflection of light by a system of nonabsorbing isotropic film-nonabsorbing isotropic substrate with randomly rough boundaries," J Opt Soc Am **61**, 1630-1639 (1971).
24. R. D. Jacobson, S. R. Wilson, G. A. Al-Jumaily, J. R. McNeil, J. M. Bennett, and L. Mattsson, "Microstructure characterization by angle-resolved scatter and comparison to measurements made by other techniques," App Opt **31**, 1426-1435 (1992).
25. E. Marx and T. V. Vorburger, "Direct and inverse problems for light scattered by rough surfaces," App Opt **29**, 3613-3626 (1990).
26. J. E. Harvey, A. Krywonos, and C. L. Vernold, "Modified Beckmann-Kirchhoff scattering model for rough surfaces with large incident and scattering angles," Optical Engineering **46**, 078002 (2007).
27. J. A. Ogilvy, "Wave scattering from rough surfaces," Rep. Prog. Phys **50**, 1553-1608 (1987).
28. C. Xia, Z. Xu, M. N. Islam, F. L. T. Jr., M. J. Freeman, A. Zakel, and J. Mauricio, "10.5 W time-averaged power mid-IR supercontinuum generation extending beyond 4 μm with direct pulse pattern modulation," IEEE JOURNAL OF SELECTED TOPICS IN QUANTUM ELECTRONICS **15**, 422-434 (2009).

# Chapter VII

# Summary and Future Work

In my thesis, I present the development of fiber based infrared lasers and demonstrate their applications in various fields such as medicine, defense and metrology. One of the significant works in my thesis is our first field trial performed at the Wright Patterson Air Force Base with an SC laser developed as part of my thesis work and used as an active illumination source for spectral reflectance measurements of samples kept 1.6 km from the laser. Another significant work presented in this thesis is our first live animal trial investigating the use of a focused infrared laser for renal denervation as a potential treatment option for resistant hypertension. Besides these major contributions, my thesis also describes numerous other significant studies using infrared fiber lasers, such as laser acne treatments and non-invasive surface roughness measurements. In this chapter, I will briefly summarize the important findings for each topic in this thesis and present some of my thoughts on the future work in these fields.

## 1 Laser Treatments for Acne

In chapter II, we develop an all- fiber based Raman laser source at 1708 nm, a wavelength near the lipid absorption peak at ~1720 nm and demonstrate the capability of this laser to thermally damage sebaceous glands located deep into the dermis. The 1708 nm laser is shown to be effective in selectively targeting and thermally damaging fat/lipid rich tissues as indicated by the *ex vivo* porcine heart, porcine visceral fat tissue and porcine skin tissue results. The 1708 nm laser, together with a contact cooling method is then used to thermally damage sebaceous glands at depths up to ~1.65 mm (at an average

fluence of 80J/cm$^2$) in human skin without apparent injury to the epidermis. The results presented in chapter II indicate that the 1708 nm laser may offer a more efficient way to target lipid-containing structures in the skin and, thus, imply the potential use of this device as a better approach to the treatment of acne vulgaris. One of the issues discussed in chapter II is the lack of evidence for selective damage of the sebaceous glands. While selectivity is clearly apparent between fat and tissue as seen in the porcine tissue experiments, we did not observe any clear histochemistry indication that the 1708 nm Raman laser is able to selectively damage the sebaceous glands without injuring the surrounding dermal tissue.

Selective damage to tissue structures has been explored in literature [1-3] . One of the more obvious requirements for selective damage is that the target structure must have a greater optical absorption at some wavelength than the surrounding tissue. The absorption spectra for fat and water clearly show an absorption peak for fat at wavelengths around ~1720nm, which suggests that the wavelengths around ~1720 nm are attractive candidates for selectively targeting lipid rich structures like sebaceous glands. The second important factor to consider is the exposure duration of the laser treatments. With long exposures, the heat transfer occurs and uniformly heats the entire tissue. On the other hand, the delivery of an instantaneous pulse can cause extreme temperature differences between target structure and its surroundings[1]. This transition from specific to non specific thermal damage is dependent on the thermal relaxation time ($\tau r$) defined as the time required for the central temperature of a Gaussian temperature distribution with a width equal to the target's diameter to decrease by 50 % [1]. Recently, Sakamoto et al, reported selective photothermolysis of sebaceous glands in human skin in vitro using a free electron laser (FEL)[3]. In this case, the in vitro skin samples are cooled to protect the epidermis and exposed to laser wavelengths of ~1700-1720 nm with a spot diameter of ~7-9.5mm. For the facial sebaceous glands the $\tau r$ ranges from ~20 to 130 ms. Therefore, the pulse durations in their experiments range from ~100-125 ms (64-82 J/cm$^2$) and show selective thermal damage to the sebaceous glands. However, it is also seen that there is a narrow range of exposure parameters capable of selective damage. For example, treatments at pulse durations of ~135 ms (87.6-93.5 J/cm$^2$) by the same group showed non-selective damage in the dermis[3].

Fiber based lasers are attractive for such medical applications from a practical point of view. Unlike the FEL, fiber lasers can be made compact and robust. The 1708 nm Raman laser described in chapter II uses all-fiber off the shelf telecom components as well. A fluence level of 64 J/cm$^2$ (100 ms pulse duration, 7 mm spot diameter) used by Sakomoto et al. to achieve selective damage corresponds to an incident power level of ~ 250 W. Therefore a significant power scaling of the Raman laser will be required to potentially achieve selective photothermolysis with similar treatment parameters. In our case, the fiber laser at the time is limited by the available pump powers. Continuous wave fiber lasers in the kW regime has been reported in literature [4]. However, very good thermal management is required as the power is scaled up. It is also possible to bundle or combine several fibers to scale the total power output. In addition, diode lasers at ~1700 nm, with average powers of ~7 W (QPC Lasers, CA) have also recently become commercially available. It is possible that with time, these diode lasers could scale up to much higher powers similar to the 980nm laser diodes, where fiber modules with > 100 W (IPG Photonics, MA) are now commercially available.

## 2 Laser Treatments for Hypertension

In chapter III, we demonstrate a novel technique for renal denervation using focused infrared fiber lasers, which are used to damage the renal nerves with little to no injury to the endothelium. Hypertension is a major global health hazard and renal denervation may be a potential treatment for resistant hypertension. We perform both in vitro and in vivo laser treatments in renal arteries. A specially designed laser catheter is developed and used for live animal trials in sheep. Three laser wavelengths a ~980nm, ~1210 nm and ~1700 nm are investigated based on the absorption spectra and penetration depth calculations. The focusing advantage and Beer's law are seen to be countering effects, i.e. lower optical absorption suggests a higher intensity difference between the tissue top and the focus. Both 980 nm and 1210 nm, which have a lower absorption in tissue than 1700 nm are seen to be more advantageous for renal denervation. While all three wavelengths are capable of damaging renal nerves, only 980 nm and 1210 nm lasers show histology evidence of penetrating deep enough to cause nerve damage at depths of > ~1.3mm, while also saving the endothelium. Histochemistry results of *in vivo* renal denervation in

sheep using a designed laser catheter prototype show clear evidence of renal denervation with depths of damage extending > ~ 1.5 mm from the artery wall. In some sections, we also observe laser induced damage to the media/ adventitia at depths of > ~1 mm without injury to the endothelium. However, in these cases there are no visible nerves at the treatment site or the depth of damage does not extent deep enough to cause renal denervation. The catheter capabilities are currently the major limiting factor in our animal trials. Some of the possible treatment parameters and catheter designs to minimize damage to the endothelium and non-target tissues are also discussed. The results presented in this chapter show that focused infrared lasers are a viable technique for causing renal denervation with minimum damage to the endothelium/media and warrants further research to refine the treatment parameters and evaluate its efficacy as a potential treatment for resistant hypertension.

The significant advantage of using lasers over other techniques such as RF and ultrasound is that the laser can be easily focused to damage the renal nerves with little to no injury to the endothelium. Besides saving the endothelium, the higher tissue absorption at the laser wavelengths can also potentially reduce the treatment times and patient discomfort. We are able to achieve in vitro renal nerve damage without injuring the endothelium using focused infrared laser at 980 nm. In order to potentially achieve similar or better results in vivo there are three main issues that will have to be considered in future work.

One of the main issues that need to be addressed in the future work is the catheter placement inside the renal artery. As discussed in Chapter III, the position of the distal end is critical in determining the optimum treatment parameters for renal denervation. Since the beam is focused, the position of the focus in the renal artery is important to achieve the required treatment effects. Ideally, the distal end will be in contact with the artery wall and the focus will be at the nerves ( ~1.5-2 mm from the artery wall). Maintaining artery wall contact for denervation treatments is not entirely a new issue and has been addressed in the alternate techniques such as RF and ultrasound therapy. For example, in RF denervation, the catheter (SYMPLICITY RDN, Medtronic) is designed to assist in positioning the platinum electrode tip within the artery and the flexible tip is designed to facilitate consistent artery wall contact (Fig 7.1a). In treatments using

ultrasound therapy (PARADISE, ReCor Medical), a specially designed inflated water cooled balloon surrounding the transducer is used (Fig 7.1b). Unlike the RF technique, which relies on impedance measurements to ensure wall contact, using a water cooled balloon enables the cooling fluid to circulate during the treatment and keep the artery wall cool and minimize endothelial and non-target tissue damage. In addition, the balloon positions the ultrasound transducer in the center of the renal artery and enables uniform energy delivery circumferentially. For the laser catheter, we could adopt a design similar to the RF technique to maintain contact with the artery wall during treatments. Another option is to use the cooled balloon technique similar to the ultrasound therapy[5], with the distal end either centered or at fixed off-axis distance from the center.

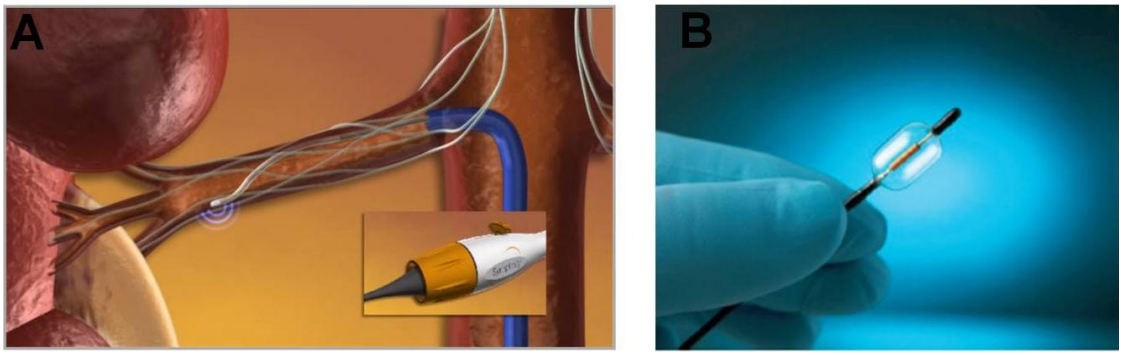


*Fig 7.1. Catheters used in current renal denervation procedures. (a) SYMPLICITY catheter design used for RF renal denervation (http://www.medtronicrdn.com/intl/news-events/media-resources/index.htm )(b) PARADISE catheter design used for ultrasound renal denervation[5].*

Once the position of the distal end in the artery is fixed, the next issue to consider is the focusing property of the optics used. It might be beneficial to use a focusing optic with the highest available numerical aperture (NA) for a given focal length (~2mm in this case), since this configuration would then give the highest optical intensity between the lumen wall and the nerves. For the available GRIN lens used in chapter III, the ZEMAX simulations Fig 7.2 show the calculated NA for the different focal lengths, suggesting that the NA increases with decreasing focal length, achieved by increasing the air gap length. Therefore, using a focal length of ~2mm in addition to maintaining wall contact should in theory, give us the highest optical intensity difference between the endothelium and the nerve for this optical configuration. However, increasing the air gap would also ultimately increase the overall length of the distal end, which might make it harder to maneuver inside the renal artery.

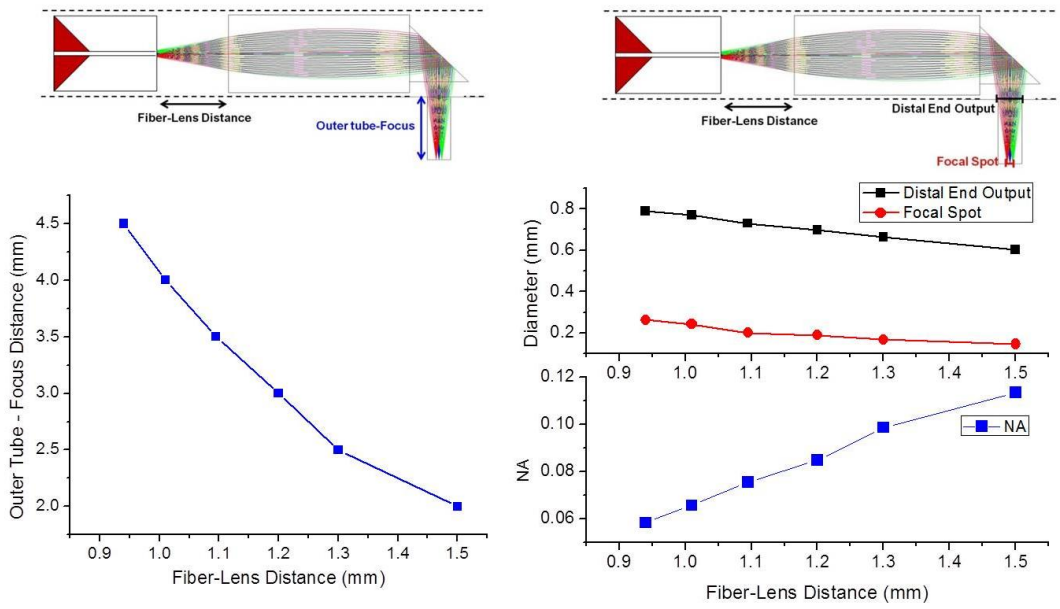


(a) (b)

*Fig. 7.2 ZEMAX simulations for GRIN lens (a) Outer-tube to focus distance versus air gap distance. (b) Beam diameter at outer tube and focal spot and the corresponding NA calculations*

The third issue to consider in future work is the ability to potentially cause selective damage to the nerves with minimal injury to the surrounding adventitial tissue. As mentioned in section1, the wavelength is one aspect of the requirements for selective damage, the second aspect being the laser exposure duration. Since the nerves are surrounded by lipid rich myelin sheaths, it might be possible to selectively damage the nerves by targeting the myelin sheaths using wavelengths with lipid absorption peaks, such as ~1700 nm and ~1210 nm. As we saw in chapter III, the focusing advantage appears to be countered with higher absorption. From this point of view, it might be more beneficial to use 1210 nm for selective damage of the renal nerves with focused light. If an external cooling mechanism (like a water cooled balloon) is applied such that focusing is no longer required or is made redundant to save the endothelium and media, then both ~1700 nm and 1210 nm may be used. For the laser exposure duration, the optimal pulse duration is calculated in chapter III to be in the range of 3 ~ 300 ms. Assuming that majority of the renal nerves are ~ 260 microns in diameter[6], we then calculate a required pulse duration of ~ 30 ms for potential selective nerve damage using [1]. The in vitro experiments in chapter III are performed with the focused laser beam scanned over the artery tissue. With a beam diameter of ~0.4 mm at the adventitia around the nerves

and a scan speed of ~0.4mm/s, this corresponds to an effective exposure time of ~1s at the nerve site. To maintain similar fluence levels at ~30 ms for similar depths and beam diameters, the total power would have to be increased ~30 X from 1.8 W to ~ 60W to potentially observe selective damage in vitro. On the other hand, in the in vivo experiments, the spot diameter for the proposed catheter design (with a 2 mm focal length) is ~0.08 mm. It is important to take into account the laser spot size differences between the in vitro and in vivo cases. For the same incident fluence, smaller spot sizes have been reported to deliver less effective fluence at targets located at depths in the tissue due to higher effects of scattering [7, 8]. Therefore, it is may not be possible to maintain the same effective fluence at the target by simply decreasing the spot diameters. Thus, further modeling will have to be performed to identify the optimum treatment parameters for renal nerve damage using short duration pulses.

## 3 Supercontinuum Laser for Remote Sensing

In chapter IV, I present the development of an all-fiber Short Wave Infrared (SWIR) supercontinuum (SC) laser covering the ~1.55-2.35μm spectral region with an average power of ~5W across the spectrum. Using this laser prototype, we performed our first field trial, where the SC laser is kept on a 12 story tower at the Wright Patterson Air Force Base (WPAFB) and propagated through ~1.6 km of atmosphere to a target kept on the runway. The SC laser is used as an active illumination source to perform spectral reflectance measurements of various samples at ~1.6 km, and the SC measurements are seen to be in good agreement with in-lab measurements performed using a conventional quartz-halogen lamp. The field trials also involve SC beam characterizations and spectral stability measurements. The developed SC laser has a near diffraction limited beam with an $M^2$ value of <1.25, when measured using a SWIR camera. The SC output variability is measured to be ~4-8% and is seen to depend on the atmospheric turbulence effects.

The spectral reflectance measurements in the field trials are performed with the target kept ~1.6 km from the SC laser, but the spectrometers and detectors are kept at small distances (< 5m) from the target to receive sufficient signal levels. While this is a great preliminary proof of concept, in an actual remote sensing scenario, the detector will also be kept at long distances from the target. Thus, a higher power SC laser will have to

be used to ensure that sufficient signal is received at the detector. Ultimately the goal is to perform air borne measurements using the SC lasers as the active illumination source. Solar illumination is a commonly used source for passive measurements. Solar radiation reaching the earth's surface depends on a variety of factors such as the location, atmospheric conditions, cloud cover, aerosol content, ozone layer conditions, time of day, earth/sun distance, solar radiation and activity[9]. Figure 7.3 shows the terrestrial solar spectrum from ~300 nm to 2500 nm published by the American Society for Testing and Materials (ASTM). The curves in the figure are from the data in ASTM standard, E 891 and E 892 for AM 1.5, a turbidity of 0.27 and a tilt of 37 deg facing the sun and a ground albedo of 0.2[9]. Direct radiation consists of the radiation straight from the sun, while the global radiation is the total ground radiation that includes the direct radiation, diffuse radiation scattered from the sky, buildings and other surroundings. The direction of the target surface has to be defined for global radiation, whereas for direct radiation, the target faces the incoming beam[9]. From Fig 7.3, we can see that the total irradiance in the ~1.5-1.8 μm and the 2-2.5 μm wavelength regions are ~75 $W/m^2$ and ~50 $W/m^2$, respectively. In chapter IV, the full angle divergence of the SC laser at 1.6 km is measured to be ~0.49 mrad, corresponding to beam diameters of ~0.4 m and ~1.5 m at ~1.6 km and ~3 km (10,000ft), respectively. We can then calculate the approximate SC power required to mimic the solar irradiation at 1.6 km and 3.05 km (10,000 ft), assuming negligible attenuation during propagation. The calculated SC power levels are shown in Table 7.1. The estimations in Table 7.1 show that in order to match the 75 $W/cm^2$ at 1.6 km and 3.05 km, we would need ~ 36 W and ~130 W of SC power in the 1.5-1.8 μm wavelength region. Similarly, the required power levels in the 2-2.5 mm wavelength region are estimated to be ~12 W and ~43 W at 1.6 km and 3.05 km respectively. It might

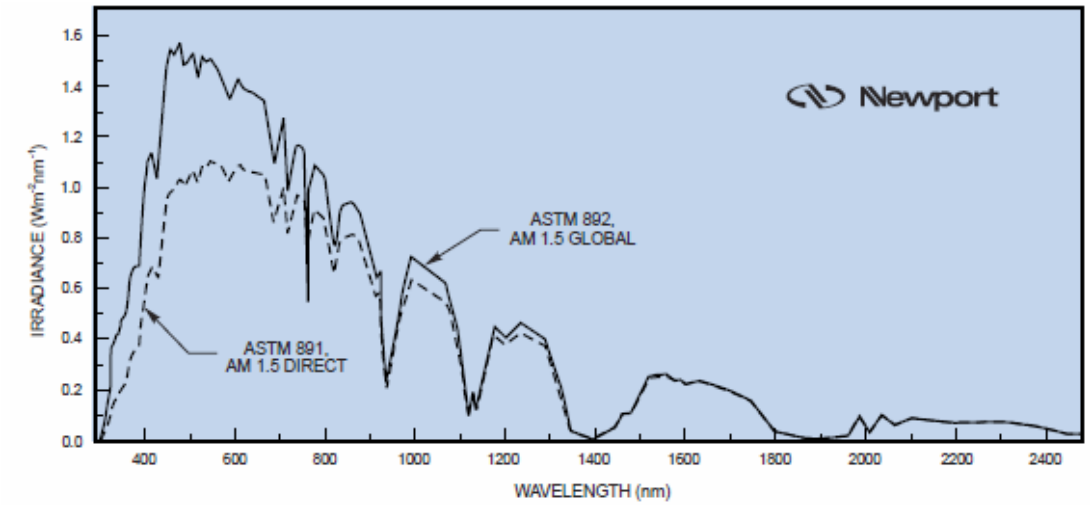


*Fig. 7.3 ASTM standard terrestrial solar spectrum for AM1.5, Direct spectrum from standard ASTM E891 and global spectrum from ASTM E892.*

*Table 7.1. Approximate values for the SC power required to match the solar irradiance at ~1.6 km and ~3 km.*

| Wavelength (mm) | Solar Irradiance | SC power Required @ ~1.6 km | SC Power Required at ~3km |
|---|---|---|---|
| 1.5-1.8 μm | 75 W/m$^2$ | 36 W | 130 W |
| 2-2.5 μm | 25W/m$^2$ | 12 W | 43 W |

SC power scalability is an active area of research in our group as well as others [10-12]. In chapter V, We demonstrate a >25 W all-fiber supercontinuum (SC) laser covering the short wave infrared (SWIR) wavelength bands from 2-2.5 μm with a spectral density of >12dBm/nm, which is the highest SC spectral density reported in this spectral range, to our knowledge. One unique aspect of this SWIR -SC source is that it is a truly power scalable laser, which we prove by showing that the SC maintains a near constant spectrum, beam quality and output stability, as the average power is scaled from 5 to 25.7W. Average power scaling is achieved by increasing the repetition rate, and a corresponding increase in the pump power helps to maintain a near constant peak power, resulting in a near constant spectral output. The SC beam quality with power scaling is seen to be near-diffraction limited with an $M^2 < 1.2$ for all power levels. Output stability measurements with power scaling show a radiometric variability <0.8% across the entire SC spectrum. High power SC lasers have also been reported with average powers as high

as ~70 W in an SC spanning from ~1.06 μm to beyond 1.7 μm [12]. Power scaling in our SC systems is currently limited by the available pump powers and we estimate that power handling limit of the 25/400/550 μm fiber used in our system to be > 100 W. However, as shown in chapter V, very good thermal management will be required as the SC power is scaled up higher. The data presents in chapter V also suggest that the spectrum, near diffraction limited beam quality and output stability should still be maintained with power scaling. Thus, the SC laser systems presents in chapters IV and V demonstrate a truly scalable SC laser system, which is an attractive feature as the power is scaled up higher for long distance applications

Another issue to consider for long distance measurements is atmospheric turbulence. As seen in chapter IV, atmospheric turbulence is clearly evident in the beam images and the output stability measurements. One solution, as demonstrated in chapter IV is to average multiple frames to obtain a smoother beam profile. However, when collecting from an airborne platform, we may not have the time to take multiple frames of the same area. At small time scales, the turbulence can also affect the spatial distribution of illumination, which may not be as predicted by a Gaussian distribution. So, the spatial optical mixing will be subject to a varying weighing function. This may not make much difference for surfaces of uniform composition, but could distort the results for mixed-material surfaces[13, 14]. In addition, for a broadband system, the fluctuations are wavelength dependent and must be taken into account when measuring the reflectance spectrum of a remote target[15]. Some of the techniques used to mitigate the effects of atmospheric turbulence on laser propagation measurements include the use of adaptive optics, deformable mirrors, beam dithering, etc [16]. Further research and modeling will have to be performed to identify the applicability of these or other techniques to mitigate the effects of atmospheric turbulence for SC laser measurements.

## 4 Supercontinuum Laser for Metrology

Finally, in chapter VI, I present an application of infrared fiber lasers in metrology, where we demonstrate an RMS surface roughness measurement system capable of measuring roughness values in the range of ~0.05 to 0.35 μm, from the slope of the wavelength dependence of reflected light, using a super-continuum laser, from 1.2 to 2 μm. Surface

roughness measurements on flat metal samples with σ values ranging from ~0.14 to 0.33 μm and automobile crankshaft journals at different stages of polishing with σ values ranging from ~0.05 to 0.12 μm are performed. The σ values obtained using the SC laser are also compared with those from a stylus based profilometer and a white light interferometer and shown to be in good agreement. Repeatability measurements are also performed on the system and shown to have a standard deviation of $\leq 0.002\mu m$.

Performing roughness measurements in the near IR and beyond has added advantages compared to using the visible wavelengths. We have shown that, by performing roughness measurements of metallic surfaces in the near IR, a reference measurement from the same material composition is not required and that a gold mirror can effectively be used as a reference. The longer wavelengths allow for measurements to be performed at a lower angle of incidence (45° in the case of crank journals), thus reducing possible shadowing and other scattering effects that could affect the accuracy of roughness values measured. We have also discussed the importance of the parameter g in the BK model to be < 1, while choosing the appropriate parameters such as wavelength and incident angle to perform accurate measurements using this technique. A potential application for inline inspection is also presented, where we use the system to detect and sort good crankshaft journals from defective ones not polished to specifications.

The ability of the SC laser to be collimated and focused easily is critical for roughness measurements of curved surfaces using this technique. We have successfully demonstrated the broadband super-continuum laser as a key enabler for wavelength dependent roughness measurements of flat and curved surfaces with large working distances of greater than 0.8 m from the sample to the detector. The combination of sub-micron roughness measurements at a large working distance along with the capability to measure both flat and curved surfaces, like crankshaft journals, makes the system an attractive tool for inline inspection in the industry.

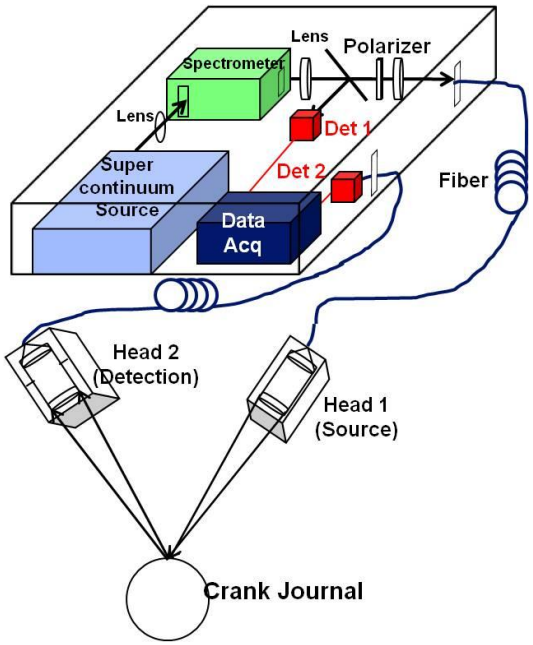


*Fig. 7.4. A potential design for in-line surface roughness measurement using the SC laser*

In a finished product on the plant floor, it might be more advantageous to be able to perform the roughness measurements at a normal incident angle, so that both the laser and the detector can be kept close to each other. As described in chapter VI, it is possible to either decrease the incident angle by using SC sources with a wider spectral bandwidth. For example, we estimate that an SC laser source spanning from ~0.7-4.5 μm can be used to measure the range of roughness values from ~0.05-0.35 μm, representative of metal surfaces finished using lapping or polishing. We have also discussed how the roughness measurement range and working distance can both be increased by SC laser systems being developed with longer wavelength bandwidths and higher power. High average power SC laser spanning from the visible to the mid-IR (0.4-4.5 μm) have been reported in the literature[10]. For example, Xia et al., reported an SC laser spanning from ~0.8-4mm with a time averaged power of >10W [17]. In addition to the broad spectrum, the high average power of such an SC laser can also enable measurements at larger working distances as well. As an example for a proposed in-line design shown in Fig. 7.4, it might also be possible to capture and fiber couple the light reflected from the sample of interest. This would then allow both the SC laser and the detector to be kept in a remote location, which might be beneficial for inline measurements in an industry environment, where space could be limited.

To conclude, in this thesis, I demonstrate the development of infrared fiber lasers and their applications in medicine, spectroscopy and metrology. In medicine, fiber based infrared lasers are attractive due to the lower tissue absorption, which allow high tissue penetration depths. In addition, the presence of absorption peaks for tissue components, such as lipids allow the potential for causing selective tissue damage. The high average powers and the attractive laser properties such as the ability to deliver a collimated or focused beam are key enablers for potential catheter based medical treatments, such as renal denervation demonstrated in this thesis. In spectroscopy, high power broadband SC lasers with near diffraction limited beam quality and good spectral stability are key enablers for long distance applications like remote sensing and hyperspectral imaging. High power SC lasers are an active area of research and the works presented so far looks promising for their potential use in airborne measurements. Finally, in metrology, the broad bandwidth and high power of infrared lasers are attractive for surface profile measurements such as surface roughness and defect detection and can help improve the quality standards of manufacturing by enabling non-contact in-line measurements on the plant floor.

## References


1. R. R. Anderson and J. A. Parrish, "Selective Photothermolysis: Precise Microsurgery by Selective Absorption of Pulsed Radiation," Science **220**, 524-527 (1983).
2. J. A. PARRISH, R. R. ANDERSON, T. HARRIST, B. PAUL, and G. F. MURPHY, "Selective Thermal Effects with Pulsed Irradiation from Lasers: From Organ to Organelle," Journal of Investigative Dermatology **80**, 75s-80s (1983).
3. F. H. Sakamoto, A. G. Doukas, W. A. Farinelli, Z. Tannous, M. Shinn, S. Benson, G. P. Williams, J. F. Gubeli, H. F. Dylla, and M. R. Rox Anderson, "Selective Photothermolysis to Target Sebaceous Glands:Theoretical Estimation of Parameters and Preliminary Results Using a Free Electron Laser," Las Surg Med **44**, 175-183 (2012).
4. A. Tünnermann, "High-power cw Fiber Lasers-Present and future," LTJ **2**, 54-56 (2005).
5. T. Mabin, M. Sapoval, V. Cabane, J. Stemmett, and M. Iyer, "First experience with endovascular ultrasound renal denervation for the treatment of resistant hypertension," Eurointervention **8**, 57-61 (2012).
6. Y. Sinelnikov, S. McClain, Y. Zou, D. Smith, and R. Warnking, "Renal denervation by intravascular ultrasound: Preliminary in vivo study," AIP. Conf. Proc **1481**, 337-344 (2012).
7. M. Lukac, M. Gorjan, J. Zabkar, L. Grad, and Z. Vizintin, "Beyond Customary Paradigm: FRAC3® Nd:YAG Laser Hair Removal " Journal of the Laser and Health Academy **1**, 35-46 (2010).
8. B. Cencic, M. Lukac, M. Marincek, and Z. Vizintin, "High Fluence, High Beam Quality Q-Switched Nd:YAG Laser with Optoflex Delivery System for Treating Benign Pigmented Lesions and Tattoos," Journal of the Laser and Health Academy **1**, 9-18 (2010).
9. "Introduction to Solar Radiation", retrieved http://www.newport.com/Introduction-to-Solar-Radiation/411919/1033/content.aspx.
10. V. V. Alexander, O. P. Kulkarni, M. Kumar, C. Xia, M. N. Islam, F. L. T. Jr, M. J. Welsh, K. Ke, M. J. Freeman, M. Neelakandan, and A. Chan, "Modulation instability initiated high power all-fiber supercontinuum lasers and their applications," Opt. Fiber Tech **18**, 349-374 (2012).
11. C. Larsen, D. Noordegraaf, P. M. W. Skovgaard, K. P. Hansen, K. E. Mattsson, and O. Bang, "Gain-switched CW fiber laser for improved supercontinuum generation in a PCF," Opt. Express **19**, 14883-14891 (2011).
12. R. Song, J. Hou, S. Chen, W. Yang, and Q. Lu, "High power supercontinuum generation in a nonlinear ytterbium-doped fiber amplifier," Opt. Lett **37**, 1529-1531 (2012).
13. A. Ifarraguerri, "Personal correspondence on atmospheric turbulence effects," (SAIC, 2013).
14. J. Meola, "Personal correspondence on atmospheric turbulence effects," (Air Force Research Labs, 2013).

15. D. A. Orchard, A. J. Turner, L. Michaille, and K. R. Ridley, "White light lasers for remote sensing," in *Proc. SPIE 7115, Technologies for Optical Countermeasures V*, 2008),
16. M. C. Roggemann and D. J. Lee, "Two-deformable-mirror concept for correcting scintillation effects in laser beam projection through the turbulent atmosphere," Appl. Opt **37**, 4577-4585 (1998).
17. C. Xia, Z. Xu, M. N. Islam, F. L. T. Jr., M. J. Freeman, A. Zakel, and J. Mauricio, "10.5 W time-averaged power mid-IR supercontinuum generation extending beyond 4 μm with direct pulse pattern modulation," IEEE JOURNAL OF SELECTED TOPICS IN QUANTUM ELECTRONICS **15**, 422-434 (2009).